Delft University of Technology

Micromechanical Modelling of Porous Asphalt Mixtures

Zhang, H.

DOI
10.4233/uuid:35a16fd8-6cde-49c6-9455-042aa4ac4d0a

Publication date
2022

Document Version
Final published version

Citation (APA)
Zhang, H. (2022). *Micromechanical Modelling of Porous Asphalt Mixtures*. [Dissertation (TU Delft), Delft University of Technology]. https://doi.org/10.4233/uuid:35a16fd8-6cde-49c6-9455-042aa4ac4d0a

Important note
To cite this publication, please use the final published version (if applicable).
Please check the document version above.

Micromechanical Modelling of Porous Asphalt Mixtures

Hong ZHANG

Micromechanical Modelling of Porous Asphalt Mixtures

Dissertation

for the purpose of obtaining the degree of doctor

at Delft University of Technology

by the authority of the Rector Magnificus, prof.dr.ir. T.H.J.J. van der Hagen,

chair of the Board for Doctorates

to be defended publicly on

Tuesday 7 June 2022 at 10:00 o'clock

by

Hong ZHANG

Master of Engineering in Highway & Railway Engineering

Harbin Institute of Technology, China

born in Laiwu, China

This dissertation has been approved by the promotors.

Composition of doctoral committee:

Rector Magnificus	chairperson
Prof.dr. A. Scarpas	Delft University of Technology, promotor
Prof.dr.ir. S.M.J.G. Erkens	Delft University of Technology, promotor
Dr. K. Anupam	Delft University of Technology, copromotor

Independent members:

Prof.dr.ir. E. Schlangen	Delft University of Technology
Prof.dr. L. Wang	Virginia Tech College of Engineering, United States
Prof.dr. M.E. Kutay	Michigan State University, United States
Prof.dr. A. Bhasin	The University of Texas at Austin, United States
Prof.dr.ir. M.A.N. Hendriks	Delft University of Technology, reserve member

Dedicated to my family

Acknowledgements

First of all, I would like to express my gratitude to my promoters Prof. Tom Scarpas and Prof. Sandra Erkens. During my Ph.D. study, Tom has provided support in many aspects. He is such a great promoter that he has made so many efforts on helping me find final solutions to my research questions. Without his help, it would had been impossible for me to finish this thesis. Beyond that, his enthusiasm and critical attitude towards research have strongly influenced me and this influence will last in my future career. Sandra was involved in my research halfway, but she is always very helpful. I am thankful for her critical and detailed comments on my thesis, and her recommendations for my new work.

I owe gratitude to Dr. Kumar Anupam, who is my co-promoter and daily supervisor. Whenever I have research questions, he is always there to give help. Sometimes I can be an "angry cat" during our discussion, but he is always so patient with me. In life, he is also a good friend who I can share a lot of things with and who can give me many wise pieces of advice. I am also grateful to my committee members, Prof. Erik Schlangen, Prof. Linbing Wang, Prof. Emin Kutay, Prof. Amit Bhasin, and Prof. Max Hendriks, for their time and efforts.

My sincere thanks also go back to China to my master's promoter Prof. Yiqiu Tan, my master's daily supervisors Prof. Liyan Shan and Prof. Huining Xu, and Prof. Zejiao Dong. They are the first persons who have guided me on how to do research, and their support continues during my Ph.D. study.

I also would like to thank all my colleagues in the Pavement Section for their encouragement and support. I thank Cor Kasbergen for his strong support to my research. I also would like to thank Marco Poot and Michèle van Aggelen, who have provided great help with my laboratory work. I thank Dr. Xueyan Liu for helping me get this chance to start my Ph.D. study. I also want to thank Dr. Katerina Varveri for her valuable advice on my research. Besides, I would like to thank Jacqueline Barnhoorn and Claudia Baltussen for dealing with the administration issues.

My thanks also go to Ruxin Jing, Haopeng Wang, Panos Apostolidis, Tianchi Tang, Zhaojie Sun, Peng Lin, Lili Ma, Chen Wang, Shisong Ren, Greet Leegwater, Nikiforos Pavlatos, and Daniel Akinmade. They are colleagues as well as friends who have given me great help in both research and life.

Many things have happened in these seven years, but friends have always been together with me. I would like to thank my good friends in China: Chen Chen, Hong Chen, Haiqing Zhang, Guoqing Jiang, Linhua Fang, Wei He, Jianna Jia, Ya'an Wang, and Jia Li. They have always supported me even though we are far away from each other. My genuine thanks also go to my good friends in the Netherlands, Wei Xie, Shan Qu, Xinmin

You, and Wenjuan Lv. In this foreign country, we have shared so many joys and worries and helped each other with our studies, our research, and our life.

"*Family is not an important thing. It's everything.*" I would like to thank my family: my father Wenlong Zhang, my mother Chunjv Di, and my sister Fenghua Zhang, for giving me all they had throughout my life. No words can express my love for all of you, especially, my father, who passed away during my Ph.D. study. Dad, life is not as beautiful as it was before you left, but moving forward is the best way to miss you.

Last but not least, I want to express my gratitude and love to my partner, Dongbin Cai. Meeting you is one of the luckiest things that have happened in my life. I am so touched that in these five years you have always supported me no matter what the situation is. Thank you for all the things that you have done to make me happy.

<div align="right">

Hong Zhang,

Delft, 3 May 2022

</div>

Contents

1

Introduction

1.1 Background

Porous asphalt (PA) mixture, which typically has a design air voids content of at least 20%, is often used as a wearing course. In the Netherlands, more than 90% of the highways are surfaced by PA mixes (Zhang et al., 2016), primarily due to their effectiveness in reducing traffic noise. PA mixes also offer other benefits such as the improvement of wet skid resistance, the reduction of hydroplaning risks, and the reduction in splashing and spraying during wet weather driving (Anupam et al., 2016).

Due to the open structure, PA mix pavements easily suffer from a certain type of damage named ravelling (Zhang et al., 2016). Ravelling is defined as the loss of individual aggregates due to abrasion caused by traffic load and/or weather conditions (Mo et al., 2010). After the initial ravelling, the damage can rapidly progress. Ultimately, ravelling can lead to the formation of potholes which can significantly reduce the driving safety of the road (Kringos and Scarpas, 2008).

In order to characterize the susceptibility of a given PA mix to ravelling, various experimental methods have been developed. The commonly used tests include among others Rotating Surface Abrasion Test (RSAT) (Kelie, 2009), Aachener Ravelling Tester (ARTe) (Qiu et al., 2016), and Skid Resistance & Smart Ravelling-Interface Testing Device (SR-ITD) (Khedoe et al., 2016). In these tests, the movement of wheels generates shear forces which introduce the loss of the stones from the surface of the specimen. The ravelling resistance is indicated by the loss of the specimen's mass. Although these tests provide a quick and simple way to compare the ravelling resistance of PA mixes, they do not give any fundamental insight into the physical mechanisms related to ravelling.

a. Cohesive damage   **b. Adhesive damage**
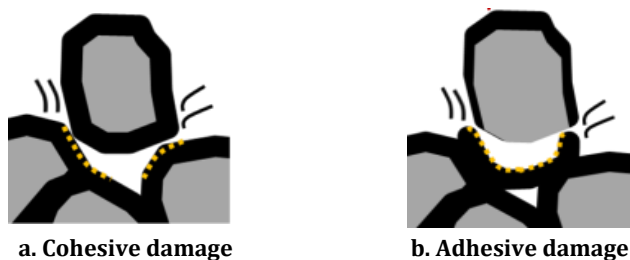
Figure 1.1 Two damage modes of ravelling distress

In recent studies, researchers pointed out that ravelling can be considered as a type of fatigue failure that occurs within the stone-on-stone contact regions (Huurman, 2007, Mo et al., 2009). On the microscale, two types of damage modes can occur, the cohesive damage and the adhesive damage (Mo et al., 2010). Cohesive damage is the failure of the mortar bridges that bond two particles, while adhesive damage is the failure of the mortar-aggregate interface, see Figure 1.1. Based on this ravelling

mechanism, the problem of analysing the ravelling distress of a PA mix pavement can be converted to the problem of analysing the fatigue characteristics of the mortar and those of the mortar-aggregate interface. The susceptibility of the given mix to ravelling can be assessed on the basis of the information about the predominant damage mode and the number of tire passages required to cause this damage (fatigue life).

In order to determine the number of tire passages required to cause fatigue damage to the mortar and the mortar-aggregate interface, the stresses/strains of these two components when tire loads are subjected to PA pavements are needed. This indicates that when the propensity of a given mix to ravelling is analysed, it is required to get into the component level of the mix to capture the local stress/strain field of each phase.

Currently, the most commonly used method to obtain the local stress and strain fields at the component level is the computational technique based on finite element methods (FEM) and/or discrete element methods (DEM) (Kringos and Scarpas, 2005, Mo et al., 2008, Anupam et al., 2014, Anupam et al., 2016, Manrique-Sanchez et al., 2018). In FEM/DEM-based micromechanical models, a PA mix is modelled as a heterogeneous material with different phases (mortar/mastic, aggregates, and air voids), and each phase is composed of a huge number of FEM/DEM elements. Although FEM/DEM-based models can handle complex compositions and almost realistic mix components, the modelling of different phases requires large FEM meshes (usually on the basis of CT scans) and very large-scale computational facilities (Anupam et al., 2016). Such extensive computational tools and facilities are not typically available in engineering practice, so this approach is only feasible in research.

Table 1.1 Different types of micromechanical models

Micromechanical models	Examples
Semi-empirical micromechanical models (SEMM)	Christensen's model (Christensen et al., 2003)
Continuum-based micromechanical models (CBMM)	the Dilute model (Eshelby, 1957), the Mori-Tanaka (MT) model (Mori and Tanaka, 1973), the Self-consistent (SC) model (Hill, 1965), the generalized self-consistent (GSC) model (Christensen and Lo, 1979), the Differential model (Norris, 1985)
Discrete particles-based micromechanical models (DBMM)	Dvorkin's model (Dvorkin et al., 1994), Walton's model (Walton, 1987)

As an alternative to complex tools, the homogenization technique can be used to obtain the stress and strain field of each phase without the need for much computation

power. Essentially, the homogenization technique provides an analytical way to derive a relationship between the effective properties of a heterogeneous material on the macroscale and the properties of its individual phases on the microscale (Charalambakis, 2010). Based upon the homogenization technique, different types of micromechanical models have been developed. Examples include Semi-empirical micromechanical models (SEMM), Continuum-based micromechanical models (CBMM), and Discrete particles-based micromechanical models (DBMM), see Table 1.1.

Since the homogenization technique connects the macroscale properties to those at the microscale, micromechanical models developed based on this technique (called as micromechanical models for short) can be used in both forward and inverse ways:

In a forward way, the properties of each phase in the microscale can be transferred into the macroscale to obtain the effective modulus of a composite. In fact, research endeavours using micromechanical models in a forward way are not new in the pavement community. Christensen's model, the MT model, the GSC model, etc. have been widely used to predict the mechanical properties of asphalt composites (Aigner et al., 2009, Shu and Huang, 2009, Kim and Buttlar, 2011, Underwood and Kim, 2013). The advantage of using micromechanical models is that it eliminates (or at least reduces) the need of conducting time-consuming laboratory tests whenever 1) it is required to alter the mix design 2) a mix design is prepared using new materials 3) it is impossible to obtain mix samples for testing 4) mixes testing facilities are not available in the laboratory. Besides, micromechanical modelling helps understand the fundamental mechanisms behind the mechanical behaviour of asphalt mixtures.

In an inverse way, the stress and strain of the composite in the macroscale can be transferred back to the microscale to obtain the local stress and strain of each phase. Although many researchers have realized the advantage of using micromechanical models in a forward way, little attention has been paid to the benefits of using this technique in an inverse way. As highlighted above, analysing the local stress/strain directly at the component level requires very powerful computational facilities. On the contrary, using micromechanical models in an inverse way, the local stress/strain of each phase can be obtained from the stress/strain of the mix. Since the stress/strain of the mix can be analysed on the macroscale by considering the mix as a homogenized material, much less computational power is required.

Taking advantage of the two different ways of using micromechanical models, one possible solution to analyse the ravelling distress of a PA mix can be given, see Figure 1.2. At first, the properties of individual components are measured in the laboratory and the stiffness of a PA mix is predicted using micromechanical models. Then, the strains in the PA mix layer are calculated by means of any available pavement analysis tool (i.e. 3D-MOVE) on the basis of the predicted mix's stiffness. Lastly, the local stresses/strains in the individual phases are calculated. Based on the fatigue

characteristics of each phase under these stresses/strains conditions, the propensity of a given PA mix for ravelling can be evaluated.

Ravelling

$$\boldsymbol{\varepsilon}_i = \mathbf{A}_i : \boldsymbol{\varepsilon}_{mix}$$

$\mathbf{C}_{mor}$

$\mathbf{C}_{agg}$

$\mathbf{C}_{mix}$

$\boldsymbol{\varepsilon}_{mix}$
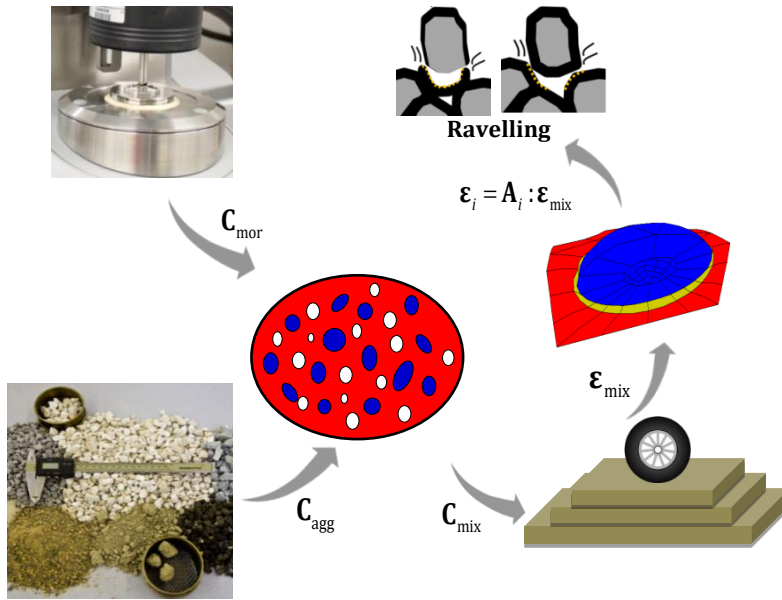
$\mathbf{C}_{mor}$ is the stiffness tensor of mortar;
$\mathbf{C}_{agg}$ is the stiffness tensor of the aggregates;
$\mathbf{C}_{mix}$ is the effective stiffness tensor of the mix;
$\boldsymbol{\varepsilon}_{mix}$ is the strain tensor of the mix;
$\boldsymbol{\varepsilon}_i$ and $\mathbf{A}_i$ are the strain tensor and the strain localization tensor of phase i respectively.

Figure 1.2 A possible solution to ravelling analysis using micromechanical models

1.2 Problem statement and research objectives

Based upon the above introductions, it can be concluded that although FEM/DEM-based micromechanical models have been developed to analyse the propensity of a given PA mix for ravelling, not many of them have been used in daily engineering applications since these models typically require very expensive computational facilities. Therefore, for pavement practitioners today, there are still no readily available and accessible tools to assist them in mitigating ravelling distress or making accurate ravelling distress predictions.

On the other hand, the utilization of homogenization-based micromechanical models is a promising method to effectively analyse the ravelling distress of PA mixes. It is, therefore, crucial for pavement researchers to carry out relevant studies. Following the proposed possible solution to ravelling analysis (see Figure 1.2), this thesis aims to

achieve the first step of accurately predicting the stiffness of a PA mix using micromechanical models. An accurate stiffness is required for the accurate calculation of the response of the pavement system. Moreover, the ability of the model to accurately predict the stiffness of the mix supports the reliability and the validity of the predicted stresses and strains of each phase.

Up to now, pavement researchers have made many efforts to evaluate the performance of different types of micromechanical models (i.e. SEMM, CBMM, and DBMM) for predicting the stiffness of asphalt materials. However, there are still a few limitations existing in these research studies:

- Calibration factors are always required in SEMM for accurately predicting the stiffness of asphalt mixtures. In literature, these factors were typically determined based upon laboratory tests performed on dense asphalt (DA) mixes. Due to the significant differences between PA mixes and DA mixes, it is not expected that these calibration factors can be directly used for PA mixes.

- The utilization of CBMM is always stuck in their poor performances at high concentrations and high temperatures/low frequencies. Although researchers have generally realized that the poor performance of CBMM is related to their limitation in describing the stiffening effect coming from the direct contacts of aggregate particles, no effective mechanics-based models have been developed to adequately account for this stiffening effect.

- Researchers' attention has been mainly paid to the utilization of SEMM and CBMM while limited experience has been provided regarding the utilization of DBMM.

Based on the above realizations, the key objective of this research is to figure out a methodology for accurately predicting the stiffness of PA mixes. For this purpose, the proposed scope of this study includes the following:

- to evaluate the performances of commonly used SEMM and CBMM in predicting the mechanical properties of PA mixes.

- to achieve the implementation of DBMM in predicting the mechanical properties of PA mixes.

- to modify the existing micromechanical models or to develop a new micromechanical model for accurately predicting the stiffness of PA mixes.

The first two parts of the scope provide a thorough investigation into both the advantages and the limitations of different micromechanical models. The obtained evaluation results can help understand the mechanisms behind the behaviour of PA mixes, and more importantly, they can provide guidance to further either modify the

existing micromechanical models or develop a new micromechanical model in order to accurately predict the mechanical properties of the mix.

1.3 Thesis outline

This dissertation consists of seven chapters that cover the utilization of different types of micromechanical models for predicting the mechanical properties of PA mixes. A brief summary of each chapter is given below.

- *Chapter 1:* introduces the background of this thesis, highlights the benefit of using micromechanical models, and describes the application of micromechanical models for PA mixes. This chapter also provides the objectives of this research work and the outline of this thesis. This chapter does not contain a literature review, instead, a literature review is provided in each chapter, addressing the corresponding topic.

- *Chapter 2:* describes the materials, specimen preparation methods, and laboratory tests that have been used in this study. Moreover, experimental results are presented and discussed.

- *Chapter 3:* develops a SEMM by revising the arrangement of individual phases in the Christensen modified Hirsch model. An aggregate organization factor, which describes the contribution from the aggregate phase to the modulus of PA mixes, is proposed. A function for calculating the values of the aggregate organization factor is determined and verified against test results. Furthermore, the contributions made by each phase to the modulus of PA mixes are analysed.

- *Chapter 4:* focuses on comprehensively evaluating the capability of commonly used CBMM (the Dilute model, the MT model, the SC model, and the GSC model) for predicting the modulus of asphalt materials. In order to assess the performance of CBMM at different inclusion concentrations, the upscaling of the moduli of both mastic and mix is implemented. In the context of predicting a mix's modulus, the effects of (1) the scale of the matrix phase (asphalt binder, mastic, and mortar), (2) the differential scheme (DS) (the constituents are included in steps rather than concurrently), and (3) the Poisson's ratio of the matrix phase on the accuracies of the predictions are investigated. On the basis of the obtained results, the limitation of CBMM is discussed.

- *Chapter 5:* explores the utilization of Dvorkin's model (one of DBMM) to predict the modulus of PA mixes. A framework for the implementation of Dvorkin's model is proposed. This framework includes (1) a proposed PA mix microstructure where an assembly of spherical particles covered by mortar materials is bonded together; (2) developed methods that are used to

determine the geometrical parameters in the microstructure; and (3) proposed procedures that are used to predict the modulus of PA mixes. Predicted results using Dvorkin's model are compared against both the experimental results and the predictions using CBMM. Moreover, sensitivity analyses are carried out to investigate the effect of the geometrical characteristics and the Poisson's ratio of mortar on the accuracy of the predictions. In the end, the advantages, as well as the limitations of Dvorkin's model, are highlighted.

- *Chapter 6:* describes the development of a hybrid micromechanical model for accurately predicting the modulus of PA mixes in a wide frequency range. This model combines the advantage of Dvorkin's model for predicting the modulus of PA mixes at higher frequencies and the advantage of Walton's model for describing the characteristics of packing aggregates at lower frequencies. Elaborations are given about how to determine the confinement for the packing aggregates in the mix. At the end of this chapter, the validation of the developed model and the discussions of the obtained results are presented.

- *Chapter 7:* summarizes the obtained results and conclusions of this thesis. This chapter also gives an outlook on the potential use and further development of the proposed methodology.

1.4 References

AIGNER, E., LACKNER, R. & PICHLER, C. 2009. Multiscale Prediction of Viscoelastic Properties of Asphalt Concrete. *Journal of Materials in Civil Engineering,* 21**,** 771-780.

ANUPAM, K., SRIRANGAM, S. K., SCARPAS, A., KASBERGEN, C. & KANE, M. 2014. Study of Cornering Maneuvers of a Pneumatic Tire on Asphalt Pavement Surfaces Using the Finite Element Method. *Transportation Research Record,* 2457**,** 129-139.

ANUPAM, K., SRIRANGAM, S. K., VARVERI, A., KASBERGEN, C. & SCARPAS, A. 2016. Microstructural Analysis of Porous Asphalt Concrete Mix Subjected to Rolling Truck Tire Loads. *Transportation Research Record: Journal of the Transportation Research Board,* 2575**,** 113-122.

CHARALAMBAKIS, N. 2010. Homogenization Techniques and Micromechanics. A Survey and Perspectives. *Applied Mechanics Reviews,* 63.

CHRISTENSEN, D. W., PELLINEN, T. & BONAQUIST, R. F. 2003. HIRSCH MODEL FOR ESTIMATING THE MODULUS OF ASPHALT CONCRETE. *Journal of the Association of Asphalt Paving Technologists,* 72**,** 97-121.

CHRISTENSEN, R. M. & LO, K. H. 1979. Solutions for effective shear properties in three phase sphere and cylinder models. *Journal of the Mechanics and Physics of Solids,* 27**,** 315-330.

DVORKIN, J., NUR, A. & YIN, H. 1994. Effective properties of cemented granular materials. *Mechanics of Materials,* 18**,** 351-366.

ESHELBY, J. D. 1957. The determination of the elastic field of an ellipsoidal inclusion, and related problems. *Proceedings of the Royal Society of London. Series A. Mathematical and Physical Sciences,* 241**,** 376.

HILL, R. 1965. A self-consistent mechanics of composite materials. *Journal of the Mechanics and Physics of Solids,* 13**,** 213-222.

HUURMAN, M. 2007. Lifetime Optimisation Tool, LOT.

KELIE, C. J. P. 2009. Onderzoek naar de invloed van het wegdektype op de bandenslijtage d.m.v. de Rotating Surface Abrasion Test (Research on the Influence of the Type of Road Surface on Tire Wear through Rotating Surface Abrasion Test). The Netherlands: De Dienst Verkeer en Scheepvaart (Department of Traffic and Navigation), Rijkswaterstaat.

KHEDOE, R., DE BONDT, A., VILLANI, M. & SCARPAS, T. 2016. *The development and use of the Skid Resistance and Smart Ravelling Interface Testing Device*.

KIM, M. & BUTTLAR, W. G. 2011. Differential Scheme Effective Medium Theory for Hot-Mix Asphalt |E*| Prediction. *Journal of Materials in Civil Engineering,* 23**,** 69-78.

KRINGOS, N. & SCARPAS, A. 2005. Raveling of Asphaltic Mixes Due to Water Damage: Computational Identification of Controlling Parameters. *Transportation Research Record: Journal of the Transportation Research Board,* 1929**,** 79-87.

KRINGOS, N. & SCARPAS, A. 2008. Physical and mechanical moisture susceptibility of asphaltic mixtures. *International Journal of Solids and Structures,* 45**,** 2671-2685.

MANRIQUE-SANCHEZ, L., CARO, S. & ARáMBULA-MERCADO, E. 2018. Numerical modelling of ravelling in porous friction courses (PFC). *Road Materials and Pavement Design,* 19**,** 668-689.

MO, L., HUURMAN, M., WU, S. & MOLENAAR, A. A. A. 2009. Ravelling investigation of porous asphalt concrete based on fatigue characteristics of bitumen–stone adhesion and mortar. *Materials & Design,* 30**,** 170-179.

MO, L. T., HUURMAN, M., WOLDEKIDAN, M. F., WU, S. P. & MOLENAAR, A. A. A. 2010. Investigation into material optimization and development for improved ravelling resistant porous asphalt concrete. *Materials & Design,* 31**,** 3194-3206.

MO, L. T., HUURMAN, M., WU, S. P. & MOLENAAR, A. A. A. 2008. 2D and 3D meso-scale finite element models for ravelling analysis of porous asphalt concrete. *Finite Elements in Analysis and Design,* 44**,** 186-196.

MORI, T. & TANAKA, K. 1973. Average stress in matrix and average elastic energy of materials with misfitting inclusions. *Acta Metallurgica,* 21**,** 571-574.

NORRIS, A. N. 1985. A differential scheme for the effective moduli of composites. *Mechanics of Materials,* 4**,** 1-16.

QIU, J., HUURMAN, M., JACOBS, M., WOLDEKIDAN, M. & FRUNT, M. 2016. Towards sustainable horizontal asphalt recycling. *Chinese European Workshop.*

SHU, X. & HUANG, B. 2009. Predicting Dynamic Modulus of Asphalt Mixtures with Differential Method. *Road Materials and Pavement Design,* 10**,** 337-359.

UNDERWOOD, B. S. & KIM, Y. R. 2013. Effect of volumetric factors on the mechanical behavior of asphalt fine aggregate matrix and the relationship to asphalt mixture properties. *Construction and Building Materials,* 49**,** 672-681.

WALTON, K. 1987. The effective elastic moduli of a random packing of spheres. *Journal of the Mechanics and Physics of Solids,* 35**,** 213-226.

ZHANG, Y., VAN DE VEN, M., MOLENAAR, A. & WU, S. 2016. Preventive maintenance of porous asphalt concrete using surface treatment technology. *Materials & Design,* 99**,** 262-272.

2

Experimental program

2.1 Introduction

As introduced in the previous chapter, micromechanical models predict the mechanical properties of a mix on the basis of the properties of individual constituents (i.e. mechanical, geometric, and volumetric properties). In order to utilize these models for PA mixes, laboratory tests need to be conducted to measure (1) the properties of individual constituents as inputs and (2) the mechanical properties of PA mixes for evaluating the accuracy of the predictions.

As a viscoelastic material, the mechanical properties of an asphalt mixture, without the consideration of damage, are generally characterized using the creep compliance or the relaxation modulus in the time domain or the complex modulus in the frequency domain. For the sake of testing time, the complex modulus of PA mixes was used in this study. Therefore, temperature and frequency sweep tests, which are typically used to measure the complex modulus of an asphalt mixture, were conducted in the laboratory. Accordingly, in order to predict the complex modulus of a PA mix, the complex moduli of the mix's viscoelastic constituents, i.e. asphalt binder, mastic and mortar, are required. Hence, temperature and frequency sweep tests were carried out for asphalt binder, mastic and mortar as well.

In this chapter, detailed procedures to prepare PA mastic, PA mortar and PA mixes specimens and to conduct temperature and frequency sweep tests are introduced. Furthermore, the measured results of the properties of each constituent and the mechanical properties of the mix are presented and discussed.

2.2 Materials

The aggregates that were used for making PA mixes specimens consisted of crushed Norwegian BESTONE aggregates (2mm-16mm) and crushed sand (0-2mm). The filler was Wigro 60K filler (25%-35% lime), produced by Ankerpoort NV. The densities of each size of aggregates and filler were measured according to the AASHTO standard methods (AASHTO, 2009b, AASHTO, 2009c). The asphalt binder, provided by Q8/ Kuwait Petroleum B.V., had a penetration grade of 70/100 and an assumed density of 1032 kg/m³.

Table 2.1 Gradation and density of aggregates

Size (mm)	16	11.2	8	5.6	2	0.5	0.18	0.125	0.063	Filler
% Passing	98	77	44	22	15	14	9	6	4	0
Density (kg/m³)	2686	2686	2678	2670	2673	2658	2658	2658	2658	2638

The recipe for making PA mix specimens conformed to the Dutch standards specifications (CROW, 2015). The content of the asphalt binder was 4.3% by the total weight of the mix. The aggregates gradation is shown in Table 2.1.

2.3 Specimens preparation

2.3.1 Specimens preparation for PA mixes

PA mixes specimens were prepared according to the ASSHTO standard method (AASHTO, 2015). PA mix materials were compacted using a gyratory compactor to obtain initial specimens with a size of 170 mm in height and 150 mm in diameter. Some of the specimens (termed as "PA mix-1") were performed reference compaction effort to target the designed air voids content of 20%. In order to investigate the applicability of micromechanical models for mixes with different microstructures, more compaction effort was deliberately applied to the remaining specimens (termed as "PA mix-2") to create a denser aggregates pack. All the specimens obtained from the gyratory compactor were further cored and cut to the test specimens with a height of 150 mm and a diameter of 100 mm.

2.3.2 Specimens preparation for mortar

In this study, mortar specimens contained sand particles smaller than 0.5 mm, filler, and asphalt binder. The proportioning of the fine aggregates in the mortar was kept the same as that in the full mixture, but it was normalized with respect to the largest sieve in the mortar (0.5 mm), see Table 2.2. The content of the asphalt binder was calculated as 23% by the total weight of the mortar specimen.

Table 2.2 Gradation of aggregates in mortar

Size (mm)	0.5	0.18	0.125	0.063	Filler
Gradation (% Passing)	100	62	39	29	0

A brief overview of the preparation of mortar specimens is presented as follows. A specially designed mould was used to make mortar specimens, Figure 2.1a. At first, the preheated asphalt binder, filler, and sand particles were mixed by hand to obtain the mortar material, Figure 2.1b. In order to make mortar flow smoothly, the material and the mould were preheated up in the oven at 160°C for 30 minutes. The mortar was slowly poured into the mould to prevent the formation of air voids. Then, the filled mould was placed back in the oven at 160°C for 10 minutes to remove air bubbles in the mortar. After cooling down the mould for 10 minutes at room temperature and around 24 hours in the freezer, the specimens were removed from the mould. The size of the obtained specimens is 6 mm in diameter and 12 mm in height, see Figure 2.1c. In order to clamp specimens on the Dynamic Shear Rheology (DSR) device, steel rings of

1 mm in thickness and 4 mm in height were attached at the top and bottom (Huurman, 2007).

It is highlighted here that the mortar materials in this study can smoothly flow like a liquid at high temperatures, and thus no compaction effort was performed during the fabrication. This behaviour may be different from the observation in other research studies (Sousa et al., 2013) that mortar had a solid-like behaviour and thus can be compacted. However, the properties of mortar are highly dependent on its composition and the properties of each component. Until now, there is no widely accepted method to determine the composition of the mortar material (i.e., the maximum aggregate size, the aggregate gradation, the asphalt binder content, the air voids content, etc.) in a mixture (Suresha and Ningappa, 2018). According to the mortar's definition used in this study, the binder content was much higher than the values used in other studies (Sousa et al., 2013, Suresha and Ningappa, 2018); therefore, it is reasonable that the mortar in this study was more viscous. Moreover, this viscous behaviour was obtained by other researchers as well (Zhang and Leng, 2017).

| a. Mortar mould | b. Mortar material | c. Size of mortar specimen |
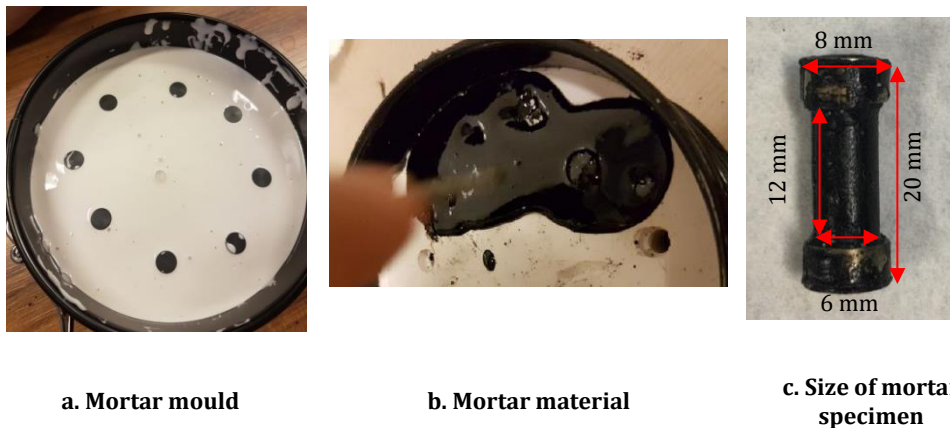
Figure 2.1 Preparation of mortar specimens

2.3.3 Specimens preparation for mastic

As defined earlier, mastic specimens consisted of asphalt binder and filler size particles (<0.063 mm). The proportioning of binder and filler was consistent with that in the whole mix. The content of the asphalt binder was calculated as 52.3% by the total weight of the mastic specimen.

The preparation method of mastic specimens for DSR tests was quite similar to that of the asphalt binder. The preheated binder and filler were mixed by hand for around 2 minutes to obtain well blended and homogeneous mastic material. The mastic material was then poured into silicone moulds of 8 mm in diameter for testing.

2.4 Test methods

In this study, temperature and frequency sweep tests were used to determine the viscoelastic properties of asphalt materials. In this test, a specimen is subjected to a fixed level of sinusoidal or haver-sinusoidal force/displacement at a fixed frequency and temperature for a fixed number of cycles. Testing is performed at different temperatures and frequencies to obtain a set of complex moduli (represented in terms of dynamic moduli and phase angles). Furthermore, according to the time-temperature corresponding principle, the modulus and phase angle curves at different temperatures can be shifted to those at a reference temperature to obtain master curves. The master curves of modulus and phase angle can reflect the behaviour of a material in a broad frequency/temperature range.

Temperature and frequency sweep tests can be conducted in either stress-controlled mode or strain-controlled mode. In the stress-controlled mode, the amplitude of the stress remains constant during the measurement, while in the strain-controlled mode, the amplitude of the strain keeps unchanged. In this study, the strain-controlled mode was used, considering that under the stress-controlled mode, it is difficult to limit the resultant strain within the desired range. As a result, the measured modulus may be significantly affected by other physical mechanisms such as damage, visco-plasticity, etc. Since micromechanical models in this study were evaluated for predicting the un-damaged viscoelastic properties of a mix, the introduction of other physical mechanisms would affect the evaluation of the models.

2.4.1 Temperature and frequency sweep test of PA mixes

PA mix specimens were tested by using the Universal Testing Machine (UTM), see Figure 2.2. Specimens were glued on the steel plate and mounted to the fixtures. Forces were applied from the bottom of the specimens, and the force level was measured via the load cell on the top. Vertical displacement was measured using three linear variable differential transformers (LVDT), which were equally distributed around the specimens. The distance between the two end positions of each displacement sensor was 100mm.

Seven different test temperatures, -10°C, 4°C, 21°C, 37°C, 45°C, 54°C and 60°C, were used to measure the complex moduli of PA mixes in a wide temperature range. At each temperature, six frequencies of 20 Hz, 10 Hz, 5 Hz, 1 Hz, 0.5 Hz, and 0.1 Hz were performed. The number of the loading cycles for each frequency, according to the ASSHTO Standard method (AASHTO, 2015), was 200 for 20 Hz, 200 for 10 Hz, 100 for 5 Hz, 20 for 1 Hz, 15 for 0.5 Hz and 15 for 0.1 Hz.

Figure 2.2 Setup for the temperature and frequency sweep test of PA mixes

In order to investigate the difference of a mix's behaviour in tension and in compression, both a tensile strain and s compressive strain (with the same amplitudes) were subjected to the specimens, see Figure 2.3. The amplitude of the applied strains at all the temperatures and frequencies was chosen as 10 $\mu\varepsilon$. The selection of this strain level was on the basis of the consideration that the strain level has to be small enough to minimize the nonlinearity and damage of the mix. Apart from that, it is impossible with the available equipment to reliably measure the modulus of the mix at further small strain levels.

a. Tension   **b. Compression**
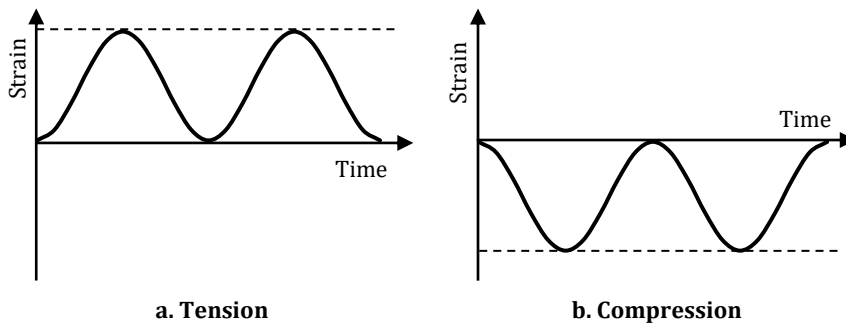
Figure 2.3 Tensile and compressive strains

2.4.2 Temperature and frequency sweep test of asphalt binder, mastic and mortar

Temperature and frequency sweep tests were conducted using a DSR device to measure the shear moduli of asphalt binder, mastic, and mortar. The Parallel-Plate Configuration

was applied to test asphalt binder and mastic specimens, while mortar specimens were tested using the so-called "Column Configuration", as shown in Figure 2.4. The test frequency ranged from 20 Hz to 0.1 Hz, at five different temperatures of -10°C, 4°C, 21°C, 37°C, and 54°C. At each temperature, constant small strains were applied to ensure the linear viscoelastic behaviour of the material, Table 2.3.

a. Fixture   **b. Configuration**
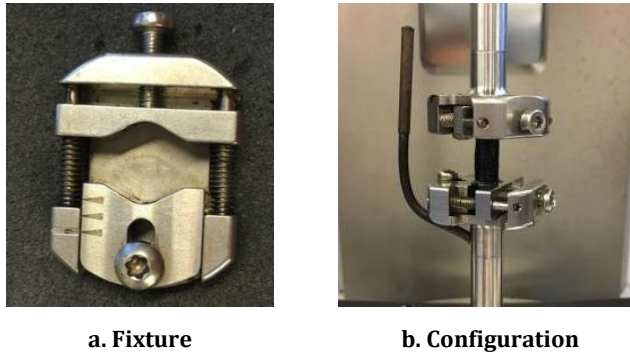
Figure 2.4 DSR setup for mortar tests

Table 2.3 Amplitudes of the applied strains for binder, mastic and mortar

Temperature (°C)	-10	4	21	37	54
Amplitude (µε)	10	50	100	200	200

2.5 Discussion and analysis of test results

2.5.1 Volumetric properties of each phase

The air voids content of PA mixes was measured using a CoreLok device according to the standard test method of ASTM D6752 (ASTM, 2018). The measured results for PA mix-1 and PA mix-2 were 18% and 13%, respectively. It is noted here that the designed air voids contents of the PA mix specimens were higher than the measured values (20% for PA mix-1). One of the possible reasons is that the plastic bags were sucked into the air voids on the surface of the specimens, see Figure 2.5. In this case, the air voids on the surface were not included in the measured total volume of the air voids. However, considering that this measurement error did not significantly affect the predicted modulus, the measured values of air voids contents were still used in all the further analyses.

Figure 2.5 Plastic bags sucked into the air voids

In this study, the upscaling of a PA mix's properties was conducted from different scales (asphalt binder, mastic, and mortar). In all the cases, the volume fraction of each phase was calculated, see Table 2.4. Upscaling from asphalt binder to mastic was also conducted. Therefore, the volume fraction of asphalt binder and filler in mastic was calculated, see Table 2.5. Since mastic could flow smoothly, its air voids content was assumed as 0%.

Table 2.4 Volume fraction of each phase

a. Volume fractions of asphalt binder, aggregates and air voids

PA mixes	Asphalt binder	Aggregate	Air voids
PA mix-1	0.085	0.735	0.18
PA mix-2	0.092	0.778	0.13

b. Volume fractions of mastic, aggregates (excluded filler) and air voids

PA mixes	Mastic	Aggregate (excluded filler)	Air voids
PA mix-1	0.116	0.704	0.18
PA mix-2	0.124	0.746	0.13

c. Volume fractions of mortar, aggregates (excluded filler and sand (<0.5 mm)) and air voids

PA mixes	Mortar	Aggregate (excluded filler and sand)	Air voids
PA mix-1	0.20	0.62	0.18
PA mix-2	0.21	0.66	0.13

Table 2.5 Volume fraction of each phase in mastic

Mastic	Asphalt binder	filler
PA mix-1 & PA mix-2	0.737	0.263

2.5.2 Modulus of PA mixes in tension and compression

The measured force and displacement of PA mixes were analysed to calculate the dynamic Young's modulus ($|E_{mix}^*|$) and the phase angle (δ_{mix}) using the standard procedure provided in the AASHTO norm (AASHTO, 2015). The master curves of $|E_{mix}^*|$ and δ_{mix} at a reference temperature of 21°C in both tension and compression are shown in Figure 2.6.

a. Dynamic Young's modulus of PA mix-1 **b. Phase angle of PA mix-1**

c. Dynamic Young's modulus of PA mix-2 **d. Phase angle of PA mix-2**
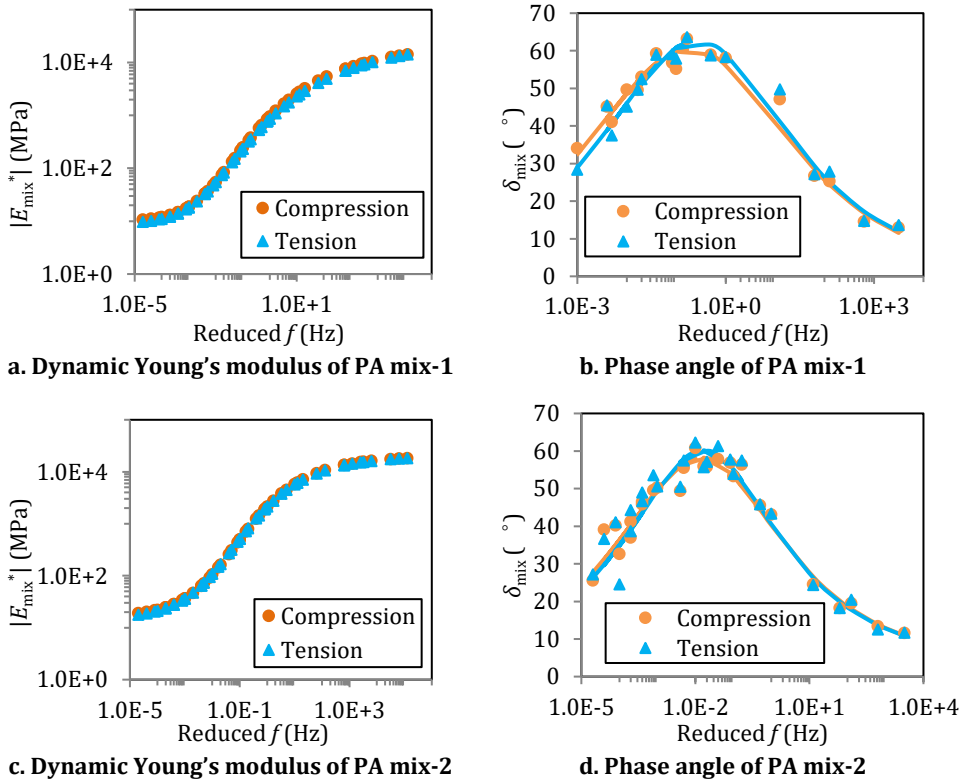
Figure 2.6 Comparison of complex modulus in tension and compression

It can be seen that the measured values of $|E_{mix}^*|$ and δ_{mix} in tension are almost the same as those in compression. This indicates that under a small strain loading condition, the stiffness of a mix is not significantly sensitive to the direction of the load.

2.5.3 Modulus of asphalt materials at different scales

The master curves of the shear moduli of asphalt binder ($|G_b^*|$ and δ_b), mastic ($|G_{mas}^*|$ and δ_{mas}) and mortar ($|G_{mor}^*|$ and δ_{mor}) at a reference temperature of 21°C are plotted in Figure 2.7. In the same figure, the values of $|E_{mix}^*|$ and δ_{mix} are also presented. Comparing the modulus and the phase angle of asphalt materials at different scales, it can be found that:
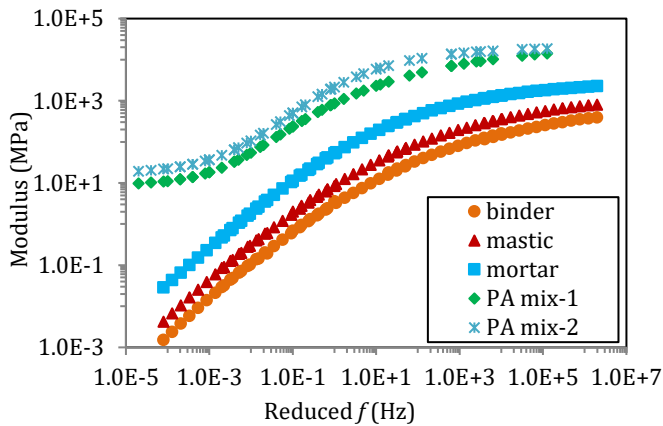
a. Modulus
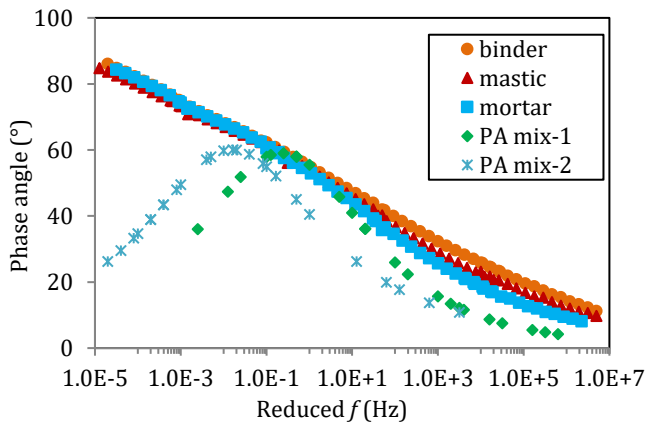
b. Phase angle

Figure 2.7 Test results of asphalt materials at different scales

- the magnitudes of $|G_{mas}^*|$ and $|G_{mor}^*|$ are higher than those of $|G_b^*|$; while the shapes of the $|G_b^*|$-f curve (or δ_b-f curve), the $|G_{mas}^*|$-f curve (or δ_{mas}-f curve), and the $|G_{mor}^*|$-f curve (or δ_{mor}-f curve) are quite similar to each other. This indicates that the addition of filler and sand particles makes asphalt binder stiffer; however, it does not significantly change the sensitivity of the material

to the frequency and temperature. This can be interpreted by the fact that mastic and mortar in this study do not contain a large number of filler and sand particles. Therefore, there is no solid body (filler, sand, etc.) packing in these materials, and thus their behaviours are mainly dominated by the asphalt binder phase.

- the magnitudes of $|E_{mix}^*|$ are higher than the moduli of asphalt binder, mastic, and mortar. In the high-frequency range (around $>10^{-1}$ Hz), the shape of the $|E_{mix}^*|$-f curve (or the δ_{mix}-f curve) shows a similar trend as those of the materials at lower scales. However, with the decrease of frequencies, the shapes of the master curves of the modulus and phase angle of the materials at different scales start to become different. While the moduli of asphalt binder, mastic, and mortar keep decreasing, $|E_{mix}^*|$ reaches a lower bound of the asymptotic value. The phase angles of asphalt binder, mastic, and mortar remain increasing, whereas δ_{mix} starts to decrease after reaching a peak value.

The above observations indicate that further addition of a large number of coarse aggregate not only produces a higher stiffness but also changes the viscoelastic behaviour of the matrix phase (asphalt binder, mastic or mortar), especially at lower frequencies/high temperatures. This can be attributed to the fact that at higher frequencies, the effect of aggregate contacts is less pronounced, and the behaviour of the matrix phase governs the behaviour of the PA mix. On the contrary, at lower frequencies, since there is no solid body packing in asphalt binder, mastic, and mortar, they are easy to be deformed, while due to the formation of the stone-on-stone skeleton framework, the deformation of the mix is limited. It is highlighted that, as will be discussed later in the paper, these different behaviours between a mix and the matrix phase are important in assessing the performance of micromechanical models.

2.6 Other properties of each phase

2.6.1 Poisson's ratio of asphalt binder, mastic, and mortar

In addition to the shear modulus, the Poisson's ratio of asphalt binder, mastic or mortar is generally used as another input to predict the stiffness of a mix. The Poisson's ratio of a viscoelastic material is supposed to be temperature- and frequency-dependent. However, until now, there have been almost no studies concerning experimentally determining the Poisson's ratio of asphalt binder, mastic, or mortar. The only well-known literature is the research work from Di Benedetto et al where the Poisson's ratios of asphalt binder and mastic were measured via laboratory tests (Di Benedetto et al., 2007). However, these tests were only conducted at lower temperatures from -30°C to 0°C, and there was no available data at higher temperatures. In fact, it is quite difficult to measure the Poisson's ratio of a liquid-like viscoelastic material at higher temperatures because of its possible permanent deformation. Therefore, in practice,

researchers generally assumed the Poisson's ratio of asphalt binder, mastic, or mortar as a constant between 0.35 and 0.5 (Underwood and Kim, 2014).

In this study, when asphalt binder, mastic or mortar was used as the matrix phase, their Poisson's ratios were initially assumed as a constant value of 0.4 to evaluate the performance of different micromechanical models. Furthermore, sensitivity analyses were conducted to investigate the effect of different values of the Poisson's ratio of the matrix on the predicted results.

2.6.2 Mechanical properties of aggregates

The shear modulus G_a and Poisson's ratio v_a of aggregates (including filler, sand, and coarse aggregates) were used as inputs for upscaling. The values of G_a and v_a were obtained from the literature (Kim and Buttlar, 2011, Underwood and Kim, 2014) as 20.8 GPa and 0.27, respectively.

2.7 References

AASHTO 2009b. Uncompacted void content of fine aggregate. *AASHTO T 304-08.* Washington, DC.

AASHTO 2009c. Standard method of test for uncompacted void content of coarse aggregate (as influenced by particle shape, surface texture and grading). *AASHTO T 326-09.* Washington, DC.

AASHTO 2015. Standard Method of Test for Determining Dynamic Modulus of Hot Mix Asphalt (HMA). Washington, D.C.

ASTM 2018. Standard Test Method for Bulk Specific Gravity and Density of Compacted Asphalt Mixtures Using Automatic Vacuum Sealing Method.

CROW 2015. Standaard RAW Bepalingen. The Netherlands.

DI BENEDETTO, H., DELAPORTE, B. & SAUZéAT, C. 2007. Three-Dimensional Linear Behavior of Bituminous Materials: Experiments and Modeling. *International Journal of Geomechanics,* 7**,** 149-157.

HUURMAN, M. 2007. Lifetime Optimisation Tool, LOT.

KIM, M. & BUTTLAR, W. G. 2011. Differential Scheme Effective Medium Theory for Hot-Mix Asphalt |E*| Prediction. *Journal of Materials in Civil Engineering,* 23**,** 69-78.

SOUSA, P., KASSEM, E., MASAD, E. & LITTLE, D. 2013. New design method of fine aggregates mixtures and automated method for analysis of dynamic mechanical characterization data. *Construction and Building Materials,* 41**,** 216-223.

SURESHA, S. N. & NINGAPPA, A. 2018. Recent trends and laboratory performance studies on FAM mixtures: A state-of-the-art review. *Construction and Building Materials,* 174**,** 496-506.

UNDERWOOD, B. S. & KIM, Y. R. 2014. A four phase micro-mechanical model for asphalt mastic modulus. *Mechanics of Materials,* 75**,** 13-33.

ZHANG, Y. & LENG, Z. 2017. Quantification of bituminous mortar ageing and its application in ravelling evaluation of porous asphalt wearing courses. *Materials & Design,* 119**,** 1-11.

3

Semi-empirical micromechanical models

3.1 Introduction

The laboratory tests used for evaluating micromechanical models have been introduced in the previous chapter. Based on these experimental results, the application of different types of micromechanical models (i.e. SEMM, CBMM and DBMM) in predicting the mechanical properties of PA mixes will be investigated. The current chapter focuses on the evaluation of SEMM. As compared to CBMM and DBMM, SEMM are much easier to be implemented, and moreover, these models have been shown to be able to accurately predict the mechanical properties of asphalt mixtures (Christensen et al., 2003b, Al-Khateeb et al., 2006). Therefore, the evaluation of SEMM, as a preliminary study, can help understand the basic concept behind micromechanical models as well as the fundamental mechanisms that affect the behaviour of PA mixes.

In SEMM, in order to relate the mechanical properties of a mix to the properties of its individual phases, individual phases are assumed to be arranged in parallel or series or a combination of them, see Figure 3.1. Different SEMM include the Voigt model, the Reuss model, the Hirsch model, etc. Among all these models, Hirsch model (Hirsch, 1962) is one of the most commonly used SEMM for asphalt mixtures. It was originally developed by Hirsch to investigate the modulus of concrete as determined by the moduli of the cement and the aggregate particles. In Hirsch model, different phases are assumed to be in a combination of parallel and series arrangements. The modulus of the composite is controlled by the volume fractions and the moduli of all its phases. Further, Christensen et al. (Christensen et al., 2003a) modified the original Hirsch model, which is referred to as Christensen's model in this study, to make it applicable for asphalt mixes.

a. Series arrangement   **b. Parallel arrangement**   **c. Combination of series and parallel arrangement**
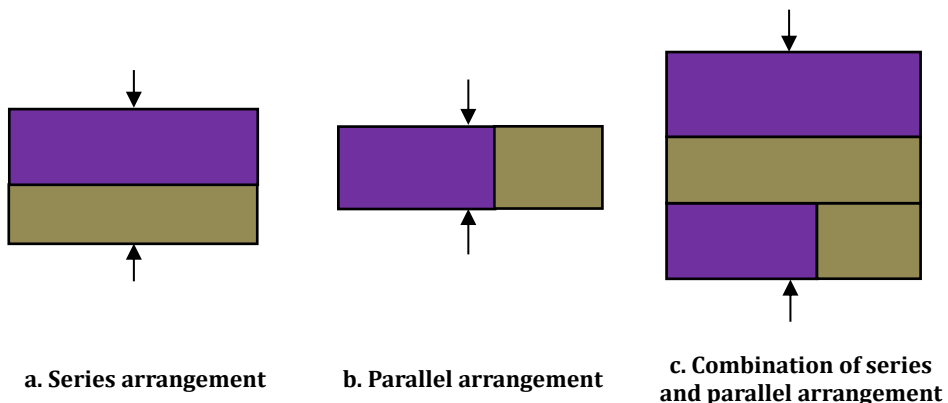
Figure 3.1 Different arrangements in SEMM

SEMM have been widely used to estimate the dynamic modulus of asphalt mixes (Dongre et al., 2005, Pellinen et al., 2007). In general, it was found that the performance of the model varies with many different factors, such as the type of mix, the volumetric

properties, the testing temperatures, etc. For example, Dongre, et al. (Dongre et al., 2005) found that Christensen's model provided reasonable predictions of dynamic modulus for asphalt mixtures from five pavement construction sites across the United States. Whereas, the research work from Bari and Witczak (Bari and Witczak, 2006), Kim, et al. (King et al., 2005) and Ceylan (Ceylan et al., 2008) showed that Christensen's model underpredicted the dynamic modulus of their studied mixes. Singh, et al. (Singh et al., 2011) concluded that Christensen's performed with good accuracy at low temperatures for the commonly used asphalt mixes in Oklahoma, while Yousefdoost, et al. (Yousefdoost et al., 2015) found that this model performed well only at 50°C for typical Australian asphalt mixes.

The reason that SEMM perform differently from different mixes is that several parameters, i.e. P_0, P_1 and P_2 in Christensen's model, are required to be calibrated in the laboratory. Therefore, although these models are developed based upon the law of mixture, they are still semi-empirical methods of predicting asphalt mixture's modulus, and their applications are limited to the type of mix that they were calibrated for. Currently, SEMM have been calibrated mainly on the basis of laboratory tests performed on DA mixes. They cannot be directly used for PA mixes, and thus, recalibrations are required in order to accurately predict the modulus of PA mixes.

Based on the above realizations, the objective of this chapter is to implement Christensen's model for estimating the mechanical properties of PA mixes. At the beginning of this chapter, a thorough investigation into the development of this model was conducted in order to capture the basic approach used by SEMM for relating the mechanical properties of a mix to the properties of its individual phases. Furthermore, recalibration of the parameters in Christensen's model was carried out using the test data in Chapter two. Additionally, in order to figure out the effect of different phases on the mechanical properties of PA mixes, this chapter also compared the contributions of different phases as quantified by Christensen's model.

3.2 Christensen's model

In the early research of Christensen et al. (Christensen et al., 2003b), various phase arrangements were proposed to modify the original Hirsch model to make it applicable for asphalt mixes. After thorough investigations of the several proposed versions of the modified Hirsh model, they came to a conclusion that the version in which the parallel and series sub-units composed of asphalt binder, aggregates, and air voids are arranged in parallel provided better prediction results of the modulus of asphalt concrete, Figure 3.2a.

a. Original arrangement   **b. Simplified arrangement**
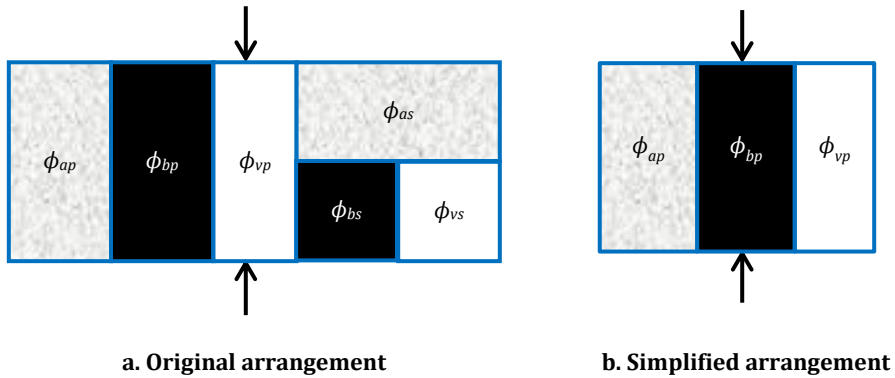
Figure 3.2 Arrangement of Christensen's model for asphalt mixes

In this version, the dynamic Young's modulus of asphalt mix $|E_{mix}^*|$ is obtained from the volume fractions and moduli of asphalt binder, aggregates, and air voids, Equation (3.1).

$$|E_{mix}^*|(f) = \phi_{ap}E_a + 3\phi_{bp}|G_b^*|(f) + (\phi_{as} + \phi_{bs} + \phi_{vs})^2 \left[\frac{\phi_{as}}{E_a} + \frac{(\phi_{bs} + \phi_{vs})^2}{3\phi_{bs}|G_b^*|(f)} \right]^{-1} \qquad (3.1)$$

where the subscripts p and s represent the parallel portion and the series portion, respectively; ϕ_a and E_a are the volume fraction and Young's modulus of the aggregate phase, respectively, ϕ_b and $|G_b^*|$ are the volume fraction and the dynamic shear modulus of the asphalt binder phase, respectively, and ϕ_v is the volume fraction of the air voids phase.

Further studies by the researchers (Christensen and Bonaquist, 2015) showed that the effects of the series sub-unit on the estimated modulus of asphalt mix are much less significant than the effects of the parallel sub-unit, which indicates that the characteristics of asphalt mix are similar to a parallel arrangement of individual phases, Figure 3.2b. Under this realization, the authors (Christensen and Bonaquist, 2015) simplified the original model to a simple parallel arrangement, as shown in Equation (3.2).

$$|E_{mix}^*|(f) = \phi_{ap}E_a + 3\phi_{bp}|G_b^*|(f) \qquad (3.2)$$

Equation (3.2) has two unknown parameters, ϕ_{ap} and ϕ_{bp}, which makes it difficult to be determined by using laboratory/field tests. Researchers (Christensen et al., 2003b) have proposed further simplification to solve this issue by introducing factors such as contact factor P_c. P_c is the share of the parallel component of the total volume of the composite and therefore varies between 0 and 1. As can be seen from Equation (3.2), if the parallel part occupies the same proportion in each phase, Equation (3.2) can be further reduced to Equation (3.3).

$$|E^*_{mix}|(f) = P_c(f)\left(\phi_a E_a + 3\phi_b |G^*_b|(f)\right)$$ (3.3)

3.2.1 Contact factor P_c

In Equation (3.3), it is obvious that P_c is one of the critical parameters in the calculation of $|E_{mix}^*|$. Since the behaviour of asphalt concrete depends on frequency/temperature, the relative proportions of the series part and parallel part are also frequency/temperature-dependent. As proposed by the researchers (Christensen et al., 2003b), the values of P_c can be calibrated from laboratory tests. The researchers concluded that the proposed factor "P_c" is frequency/temperature sensitive, as expected.

a. High frequency/Low temperature   **b. Low frequency/High temperature**
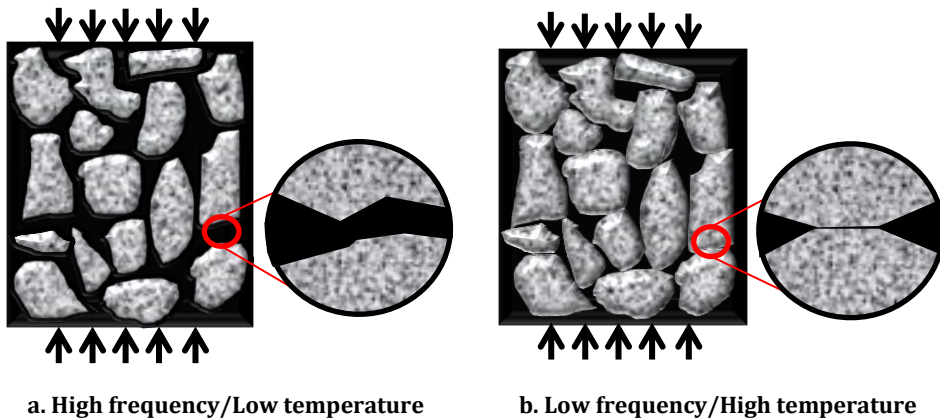
Figure 3.3 Aggregate contacts at different frequencies/temperatures

In line with the above research work, researchers (Dongre et al., 2005, Pellinen et al., 2007, Christensen and Bonaquist, 2015) showed that generally, a good agreement exists between the predicted results of Christensen's model and the laboratory tests. However, it can be stated that the physical representation of P_c is difficult. In their pioneering studies, researchers (Christensen et al., 2003b) hypothesized that P_c represented the aggregate contact factor and interpreted it as the contribution from the portion of aggregate particles in intimate contact with each other. They also noted that high values of P_c at high frequencies/low temperatures indicate more contact among aggregate particles. However, this interpretation does not comply with the physical situation where fewer aggregate particles are expected to be in intimate contact at high frequencies/low temperatures, Figure 3.3a. This behaviour is expected because of the existence of stiff asphalt binder at high frequencies/low temperatures. Similarly, at low frequencies/high temperatures when the modulus of asphalt binder is soft, it is expected that the aggregate would find it easier to move, which will result in more pronounced contact, Figure 3.3b.

Based on the above analysis, it can be concluded that the interpretation of P_c does not consider the aggregate contact interaction aptly. Thus, in the following section, a modified expression for Christensen's model will be proposed.

3.3 Modified expression of Christensen's model

As mentioned above, the effects of the series element in Christensen's model on the estimated modulus of asphalt concrete are negligible as compared to the effects of the parallel element. Therefore, in the revised arrangement, it is proposed that the total volume of asphalt binder, aggregates, and air voids are arranged in parallel, Figure 3.4. This arrangement is the same as the arrangement proposed by the original researcher (Christensen and Bonaquist, 2015) except that in the revised arrangement, the part of the volume is replaced by the total volume. The relationship between $|E_{mix}^*|$ and the properties of individual phases is shown in Equation (3.4).

$$| E_{mix}^* |(f) = \phi_a E_a + 3\phi_b | G_b^* |(f) \qquad (3.4)$$
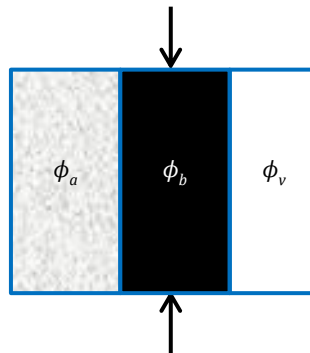
Figure 3.4 Revised arrangement of Christensen's model

This study proposed to modify Equation (3.4) by introducing a factor P_a which describes the contribution to $|E_{mix}^*|$ from the arrangement of aggregate particles at different frequency/temperature conditions, see Equation (3.5). A detailed description of P_a will be presented in the following subsection.

$$| E_{mix}^* |(f) = P_a(f)\phi_a E_a + 3\phi_b | G_b^* |(f) \qquad (3.5)$$

3.3.1 Aggregate organization factor, P_a

An Asphalt mix has a higher volume fraction of the aggregate phase than the binder and the air void phase. Moreover, the modulus of the aggregate phase is also much higher than that of the other two phases. Therefore, the contributions made by the aggregate phase to the modulus of the asphalt mix are expected to be higher than those made by other phases. If a non-frequency/temperature-dependent factor were introduced for

evaluating the contribution from the aggregate phase to the overall response of the mix, $|E_{mix}^*|$ would also be primarily frequency/temperature independent. This can be clearly deduced from Equation (3.5), where the aggregate phase contribution ($P_a\phi_a E_a$) becomes temperature/ frequency-independent due to the temperature/ frequency-independent value of P_a.

In order to physically understand the concept of P_a, if hypothetically two extreme conditions of low temperatures (or high frequencies) and high temperatures (or low frequencies) are considered, then in the case of low temperatures the asphalt binder would be stiff, and it would be able to bond the particles well together, Figure 3.5a. Whereas, at high temperatures, the binder would be too soft to bind the particles, Figure 3.5b. In the prior case, the whole structure will act together in the load-bearing capacity, on the contrary, in the other case, the asphalt binder will not take part in the load-bearing capacity, and the mix would slowly collapse.
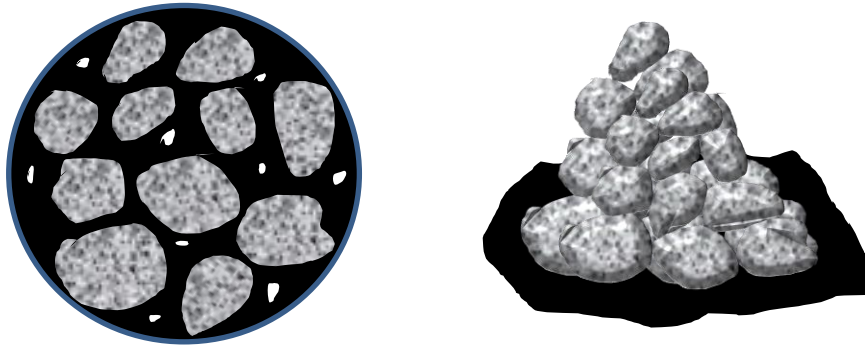
a. High frequency/Low temperature   **b. Low frequency/High temperature**

Figure 3.5 Organization of aggregates at different frequencies/temperatures

From the above discussions, it can be stated that the introduction of the factor, P_a, is logical and meaningful. It is also expected to capture the frequency/temperature-dependent contribution of the aggregate phase in predicting $|E_{mix}^*|$. P_a, which is termed as the "aggregate organization factor", has been determined and validated by the laboratory tests in this research study.

3.4 Results and discussions

3.4.1 Determination of P_a using laboratory tests

Equation (3.5) can be rearranged in the form of the following equation, Equation (3.6):

$$P_a(f) = \frac{|E_{mix}^*|(f) - 3\phi_b |G_b^*|(f)}{\phi_a E_a} \tag{3.6}$$

The values of P_a can be calculated with the mix properties using Equation (3.6). A typical curve, as obtained for PA mix-1 at 21°C, is shown in Figure 3.6. The shape of the plot shows that P_a is indeed a frequency-dependent factor, as discussed before. It can also be observed that P_a increases with the increase in frequency, and more or less follows a sigmoidal curve for the tested specimen. This, in terms of physical meaning, implies that the contribution made by the aggregate phase to the modulus of the mix increases with the frequencies.
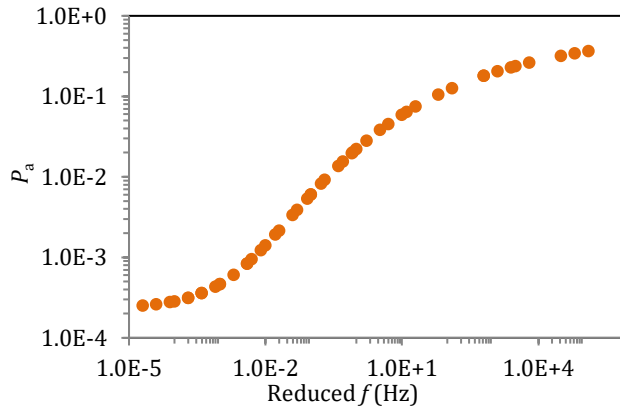
Figure 3.6 Calculation results of P_a

By assuming P_a to follow a sigmoidal curve, Equation (3.7) can be used to fit the value of P_a. It is noted here that Equation (3.7) is similar in nature to the P_c function as described by the researcher (Christensen and Bonaquist, 2015). After fitting the test results using Equation (3.7), constant parameters in the equation can be obtained, as shown in Table 3.1.

It is important that the proposed model is validated. In order to judge the suitability of the aggregate organization factor, a two-step validation approach was adopted. In the first step, the overall response of PA mix-1 was compared against the predicted results, and in the second step, predictions were made for PA mix-2 on the basis of parameters obtained in Table 3.1.

$$P_a = a + (1-a)\frac{\exp(b + c\ln(\phi_b/(\phi_b + \phi_v)\times|G_b^*|) + d(\phi_b + \phi_v))}{1 + \exp(b + c\ln(\phi_b/(\phi_b + \phi_v)\times|G_b^*|) + d(\phi_b + \phi_v))} \qquad (3.7)$$

Table 3.1 Fitting results of constant parameters

Parameters	a	b	c	d
Values	0.00022	-0.0055	0.8	-0.15

3.4.2 Validation of the modified expression of Christensen's model

Figure 3.7a and Figure 3.7b show the predicted results of $|E_{mix}^*|$ for PA mix-1 and PA mix-2, respectively. It can be observed that the predicted results of $|E_{mix}^*|$ for PA mix-1 are in good agreement with the laboratory tests, which provides a good check for the calibration procedure.
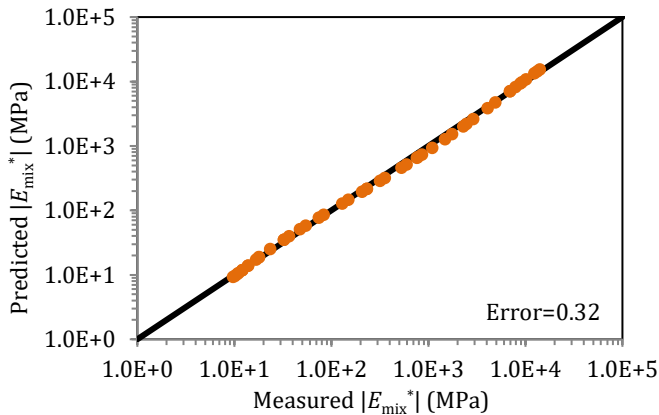
a. PA mix-1
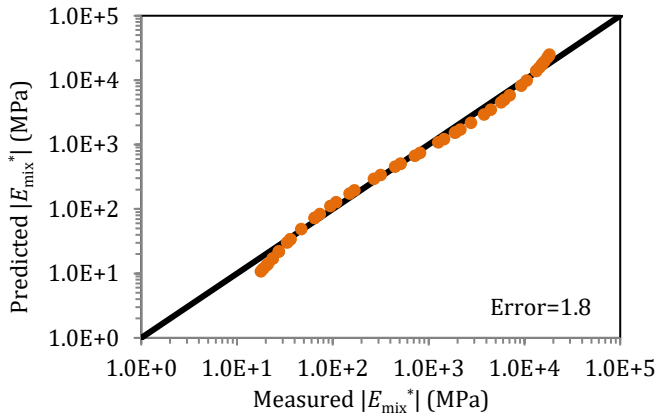
b. PA mix-2

Figure 3.7 Comparison between predicted results of $|E_{mix}^*|$ to laboratory tests

The predicted results of $|E_{mix}^*|$ for PA mix-2 on the basis of the parameters obtained from PA mix-1 fit with reasonable accuracy. These differences were already expected because the parameters used for both PA mixes in Equation (3.7), although with different properties, are the same. Despite these differences, the predicted and the test results for practical purposes match quite well for PA mixes.

3.4.3 Contribution of each phase in the $|E_{mix}^*|$ prediction

According to Equation (3.5), the contribution of the aggregate phase to the total mix modulus is obtained as $P_a\phi_a E_a$, whereas the contribution of the asphalt binder phase is obtained as $3\phi_b|G_b^*|$. Figure 3.8a and Figure 3.8b show the plots of the relative contribution of each phase in the overall response of PA mixes. It can be seen that both phases are frequency-dependent, as explained earlier.
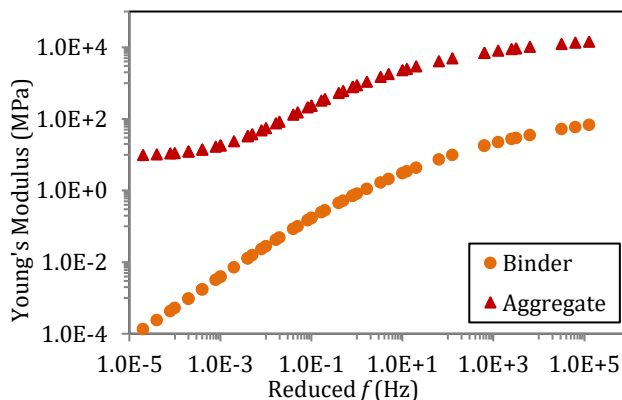
a. PA mix-1
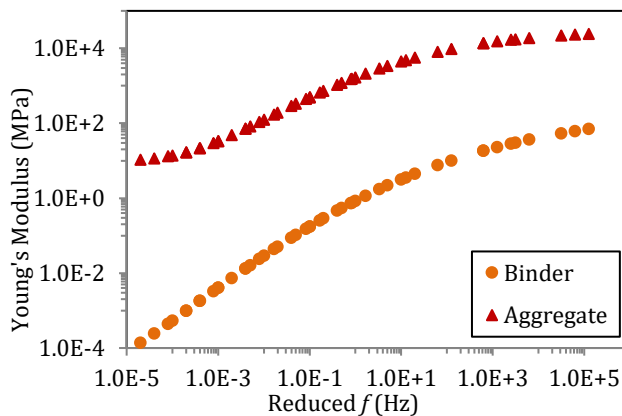
b. PA mix-2

Figure 3.8 Modulus provided by aggregates and asphalt binder in PA mix

When the moduli of each phase are compared, it is found that the aggregate phase makes a more significant contribution to the modulus of PA mixes, as expected. It can be further deduced that in PA mixes, the aggregate phase provides the load-bearing capacity while the role of the asphalt binder phase is to bind the aggregate particles together, ensuring the structural organization of the composite material.

3.5 Summary

SEMM, which have shown their capabilities of accurately predicting the mechanical properties of DA mixes, were evaluated for PA mixes in this chapter. Christensen's model, as one of the most commonly used SEMM, was expected to be able to estimate the modulus of PA mixes. However, a following thorough investigation into the development of this model showed that it does not consider the aggregate contact interaction aptly. Therefore, a modified expression for Christensen's model, with the addition of a temperature/frequency-dependent aggregate organization factor, was proposed. Furthermore, a function for calculating the aggregate organization factor was determined and verified against test results. In the end, based upon the proposed modified Christensen's model, the contributions made by each phase to the modulus of PA mixes were analysed. The following conclusions can be drawn:

- By means of the aggregates organization factor, the effects of the frequency/temperature-dependent contribution of the aggregate phase on the overall mix response can be accounted for, and the modified expression of Christensen's model can produce the shape and values of the frequency/temperature-dependent modulus of asphalt mixes.

- A sigmoidal curve function can be used to describe the characteristics of the aggregate organization factor in the whole frequency range.

- In the whole range of frequencies/temperatures, the contributions made by the aggregate phase to the overall modulus of PA mixes are much more significant than the contribution of the asphalt binder.

3.6 References

AL-KHATEEB, G., SHENOY, A., GIBSON, N. & HARMAN, T. 2006. A New Simplistic Model for Dynamic Modulus Predictions of Asphalt Paving Mixtures. *Journal of the Association of Asphalt Paving Technologists,* 75**,** 1254-1293.

BARI, J. & WITCZAK, M. W. 2006. *Development of a new revised version of the Witczak E Predictive Model for hot mix asphalt mixtures.*

CEYLAN, H., GOPALAKRISHNAN, K. & KIM, S. 2008. Advanced approaches to hot-mix asphalt dynamic modulus prediction. *Canadian Journal of Civil Engineering,* 35**,** 699-707.

CHRISTENSEN, D. W. & BONAQUIST, R. 2015. Improved Hirsch model for estimating the modulus of hot-mix asphalt. *Road Materials and Pavement Design,* 16**,** 254-274.

CHRISTENSEN, D. W., PELLINEN, J. T. & BONAQUIST, R. F. 2003a. Hirsch model for estimating the modulus of asphalt concrete. *Journal of the Association of Asphalt Paving Technologists,* 72**,** 97-121.

CHRISTENSEN, D. W., PELLINEN, T. & BONAQUIST, R. F. 2003b. HIRSCH MODEL FOR ESTIMATING THE MODULUS OF ASPHALT CONCRETE. *Journal of the Association of Asphalt Paving Technologists,* 72**,** 97-121.

DONGRE, R., MYERS, L., D'ANGELO, J., PAUGH, C. & GUDIMETTLA, J. 2005. Field Evaluation of Witczak and Hirsch Models for Predicting Dynamic Modulus of Hot-Mix Asphalt. *Journal of the Association of Asphalt Paving Technologists,* 74**,** 381-442.

HIRSCH, T. J. 1962. Modulus of elasticity of concrete affected by elastic moduli of cement paste matrix and aggregate. *Proceeding of the American Concrete Institute,* 59**,** 427-452.

KING, M., MOMEN, M. & KIM, Y. R. 2005. Typical Dynamic Modulus Values of Hot-Mix Asphalt in North Carolina and Their Prediction. *84th Annual Meeting of the Transportation Research Board.* Washington, D.C.

PELLINEN, T., ZOFKA, A., MARASTEANU, M. & FUNK, N. 2007. Asphalt Mixture Stiffness Predictive Models *Journal of the Association of Asphalt Paving Technologists,* 76**,** 575-625.

SINGH, D., ZAMAN, M. & COMMURI, S. 2011. Evaluation of Predictive Models for Estimating Dynamic Modulus of Hot-Mix Asphalt in Oklahoma. *Transportation Research Record,* 2210**,** 57-72.

YOUSEFDOOST, S., VUONG, B., RICKARDS, I., ARMSTRONG, P. & SULLIVAN, B. 2015. *Evaluation of Dynamic Modulus Predictive Models for Typical Australian Asphalt Mixes.*

4

Continuum-based micromechanical models

4.1 Introduction

The application of SEMM for predicting the mechanical properties of PA mixes has been discussed in the previous chapter. Although SEMM can provide fairly accurate predictions, the calibration of the aggregate organization factor is always required for a different type of asphalt mixes. This limitation of SEMM is probably due to the fact that in this type of micromechanical models, individual phases are simply arranged in parallel or series. In that case, the stress/strain field in the macroscale and that in the microscale can only have a relationship of either a uniform stress or a uniform strain. However, considering the complicated microstructure of a mix, it is expected that the assumption of a uniform stress or strain field is not accurate enough with respect to predicting the mechanical properties of the mix.

In comparison to Christensen's model, CBMM provide more rigorous relationships of the stress/strain fields between macroscale and microscale. The development of these models is on the basis of Eshelby's solution (Eshelby, 1957) for the inhomogeneity problem where an ellipsoid inclusion is embedded into an infinite matrix, see Figure 4.1. The strain in the macroscale and that in the microscale is related via the strain localization tensor which is a function of the mechanical and geometrical properties of the inclusion and the matrix. Depending on different assumptions about the strain localization tensor, various CBMM, i.e. the Dilute model, the SC model (Hill, 1965, Walpole, 1969), the GSC model (Christensen and Lo, 1979), the MT model (Mori and Tanaka, 1973, Benveniste, 1987), etc., have been developed.
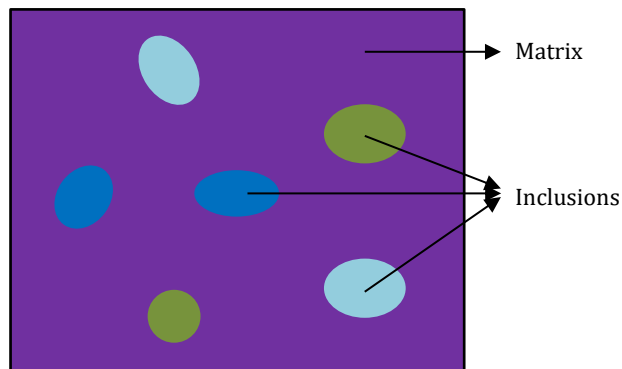
Figure 4.1 Illustration of a mix in CBMM

CBMM were initially developed for elastic composites. In the past few decades, these models have drawn the attention of researchers in the pavement community with the attempt to accurately predict the mechanical properties of asphalt materials without the need for calibrations. Up to now, the evaluation of different CBMM has been conducted in a large number of research studies (Buttlar et al., 1999, Kim and Little,

2004, Abbas et al., 2005, Shu and Huang, 2008, Yin et al., 2008, Pichler et al., 2012, Underwood and Kim, 2014). The performance of these models at different volume concentrations and test temperatures can be summarized as follows.

- At very low concentrations, most of the models can obtain good predictions (Buttlar et al., 1999, Kim and Little, 2004, Abbas et al., 2005). This is because all these models are developed on the basis of Eshelby's solution which is suitable for a composite with a low concentration of inclusions.

- At high concentrations and low temperatures, the accuracy of the predicted results varies from one model to the other (Underwood and Kim, 2014, Yin et al., 2008, Pichler and Lackner, 2009, Pichler et al., 2012). The Dilute model and the MT model have been generally found to under-predict the moduli (or over-predict the creep compliances) of an asphalt material (Pichler and Lackner, 2009, Underwood and Kim, 2013). On the contrary, the SC model and the GSC model have been found to be more suitable for high concentrations of asphalt materials (Pichler and Lackner, 2009, Underwood and Kim, 2013, Zhang et al., 2018).

- At high concentrations and high temperatures, none of these models have been found to provide accurate predictions, and in general, the predicted moduli are much lower than the measured values (Buttlar et al., 1999, Kim and Little, 2004, Underwood and Kim, 2014).

Although many efforts have been made on evaluating CBMM for asphalt materials, the above observations may not be directly used for PA mixes since these observations were typically obtained based upon laboratory tests performed on DA mixes. It is known that PA mixes and DA mixes are quite different from each other. In comparison to DA mixes, PA mixes have much higher contents of air voids and coarse aggregates but a lower content of fine aggregates. As a result, the microstructure of PA mixes may significantly differ from that of DA mixes. For example, the mortar phase is generally considered as continuous in a DA mix. In contrast, in a PA mix, the mortar may not wholly form a continuum medium due to the higher volume of air voids and the lower volume of fine aggregates. Besides, since a large number of coarse aggregates form a stone-on-stone skeleton in PA mixes, it is expected that these connected stone particles would play a more significant role in the behaviour of the mix.

Considering the significantly different microstructures between PA mixes and DA mixes, it is not expected that the performances of CBMM for different mixes are the same. Models that perform well in predicting the mechanical properties of DA mixes may not be suitable for PA mixes, and methods to improve the accuracy of predictions can also be different. Therefore, although the performance of various CBMM has been

widely evaluated for DA mixes, it is still necessary to carry out studies to investigate the performance of these models for PA mixes.

In light of the above discussions, the current chapter aims to provide a comprehensive investigation into the performances of the commonly used CBMM for predicting the modulus of PA materials. The focus of this chapter can be subdivided into three parts. The first and the second part show the performances of CBMM in predicting the moduli of PA mastic and PA mixes, respectively. Moreover, in the second part, comprehensive analyses are carried out aiming to explore the sensitivity of the predictions' accuracy to (1) the scale of the matrix phase (i.e. asphalt binder, mastic, and mortar); (2) the utilization of different micromechanical models; (3) the utilization of the DS approach; and (4) the Poisson's ratio of the matrix phase. Based on the analysis results, the limitations of CBMM are further discussed at the end of this chapter.

4.2 Introduction of commonly used CBMM

4.2.1 Stiffness tensor

In linear elasticity, the constitutive law of a material is generally given as:

$$\boldsymbol{\sigma} = \mathbf{C} : \boldsymbol{\varepsilon} \tag{4.1}$$

where $\boldsymbol{\sigma}$ is the second-order stress tenser; $\boldsymbol{\varepsilon}$ is the second-order stain tenser; $\mathbf{C}$ is the fourth-order stiffness tensor; the symbol ':' means the double dot product between two tensors.

For isotropic elastic materials, five material constants, i.e. Young's modulus E, shear modulus G, bulk modulus K, Lame constant λ, and Poisson's ratio v, are commonly used. However, only two of them are required to describe the characteristic of $\mathbf{C}$ completely (Huiming Yin, 2018). For example, by using the values of K and G, $\mathbf{C}$ can be represented as:

$$\mathbf{C} = 3K\mathbf{I}^{\mathrm{v}} + 2G\mathbf{I}^{\mathrm{d}} \tag{4.2}$$

and the value of E can be calculated as

$$E = \frac{9KG}{3K+G} \tag{4.3}$$

In Equation (4.2), $\mathbf{I}^{\mathrm{v}}$ and $\mathbf{I}^{\mathrm{d}}$ denote the volumetric part and the deviatoric part of a four-order tensor, respectively; and they are defined as

$$I^{\mathrm{v}}_{ijkl} = \frac{1}{3}\delta_{ij}\delta_{kl} \, ; I^{\mathrm{d}}_{ijkl} = \frac{1}{2}(\delta_{ik}\delta_{jl} + \delta_{il}\delta_{jk}) - \frac{1}{3}\delta_{ij}\delta_{kl} \tag{4.4}$$

where δ is the Kronecker's delta. From these definitions, the following relations between $\mathbf{I}_v$ and $\mathbf{I}_d$ can be derived:

$$\mathbf{I}^v : \mathbf{I}^v = \mathbf{I}^v ; \mathbf{I}^d : \mathbf{I}^d = \mathbf{I}^d ; \mathbf{I}^v : \mathbf{I}^d = \mathbf{0}; \mathbf{I}^d : \mathbf{I}^v = \mathbf{0}; \text{and } \mathbf{I}^v + \mathbf{I}^d = \mathbf{I} \tag{4.5}$$

where $\mathbf{I}$ is the unit fourth-order tensor, which is written as

$$I_{ijkl} = \frac{1}{2}(\delta_{ik}\delta_{jl} + \delta_{il}\delta_{jk}) \tag{4.6}$$

On the basis of the relations in Equation (4.5), it can be found that if two fourth-order tensors $\mathbf{B}_1$ and $\mathbf{B}_2$ are represented as

$$\mathbf{B}_1 = B_1^v \mathbf{I}^v + B_1^d \mathbf{I}^d \tag{4.7}$$

$$\mathbf{B}_2 = B_2^v \mathbf{I}^v + B_2^d \mathbf{I}^d \tag{4.8}$$

the double dot product of $\mathbf{B}_1$ and $\mathbf{B}_2$ can be directly given by

$$\mathbf{B}_1 : \mathbf{B}_2 = B_1^v B_2^v \mathbf{I}^v + B_1^d B_2^d \mathbf{I}^d \tag{4.9}$$

4.2.2 Homogenization process of CBMM

The effective stiffness of an N-phase composite $\mathbf{C}_{eff}$ is defined using the average stress $<\boldsymbol{\sigma}>_c$ and the average strain $<\boldsymbol{\varepsilon}>_c$:

$$<\boldsymbol{\sigma}>_c = \mathbf{C}_{eff} :< \boldsymbol{\varepsilon} >_c \tag{4.10}$$

The values of $<\boldsymbol{\sigma}>_c$ and $<\boldsymbol{\varepsilon}>_c$ for a given volume V of a representative volume element (RVE) can be described by Equation (4.11).

$$<\boldsymbol{\sigma}>_c = \frac{1}{V}\int_V \boldsymbol{\sigma}dV, <\boldsymbol{\varepsilon}>_c = \frac{1}{V}\int_V \boldsymbol{\varepsilon}dV \tag{4.11}$$

At the component level, the average stress $<\boldsymbol{\sigma}>_r$ and average strain $<\boldsymbol{\varepsilon}>_r$ of phase r over the volume of this phase (V_r) are given as Equation (4.12).

$$<\boldsymbol{\sigma}>_r = \frac{1}{V_r}\int_{V_r} \boldsymbol{\sigma}dV_r, <\boldsymbol{\varepsilon}>_r = \frac{1}{V_r}\int_{V_r} \boldsymbol{\varepsilon}dV_r \tag{4.12}$$

Substituting Equation (4.12) into Equation (4.11), $<\boldsymbol{\sigma}>_c$ and $<\boldsymbol{\varepsilon}>_c$ are rearranged as

$$<\boldsymbol{\sigma}>_c = \sum_{r=1}^{N} \phi_r <\boldsymbol{\sigma}>_r \tag{4.13}$$

$$<\boldsymbol{\varepsilon}>_c = \sum_{r=1}^{N} \phi_r <\boldsymbol{\varepsilon}>_r \tag{4.14}$$

where ϕ_r is the volume fraction of phase r in the RVE, which is defined as

$$\phi_r = \frac{V_r}{V} \tag{4.15}$$

For each phase, it is also known that $<\boldsymbol{\sigma}>_r$ and $<\boldsymbol{\varepsilon}>_r$ satisfy the constitutive law:

$$<\boldsymbol{\sigma}>_r = \mathbf{C}_r :<\boldsymbol{\varepsilon}>_r \tag{4.16}$$

where $\mathbf{C}_r$ is the stiffness tensor of phase r. By substituting Equations (4.10) and (4.16) into Equation (4.13), the value of $\mathbf{C}_{\text{eff}}$ can be related to the values of $\mathbf{C}_r$:

$$\mathbf{C}_{\text{eff}} :<\boldsymbol{\varepsilon}>_c = \sum_{r=1}^{N} \phi_r \mathbf{C}_r :<\boldsymbol{\varepsilon}>_r \tag{4.17}$$

Equation (4.18) shows a typical relationship between $<\boldsymbol{\varepsilon}>_r$ and $<\boldsymbol{\varepsilon}>_c$, which is used in CBMM (Eshelby, 1957):

$$<\boldsymbol{\varepsilon}>_r = \mathbf{A}_r :<\boldsymbol{\varepsilon}>_c \tag{4.18}$$

where $\mathbf{A}_r$ is called the strain localization tensor of phase r. By combining Equations (4.17)-(4.18), the value of $\mathbf{C}_{\text{eff}}$ is further expressed as:

$$\mathbf{C}_{\text{eff}} = \sum_{r=1}^{N} \phi_r \mathbf{C}_r : \mathbf{A}_r \tag{4.19}$$

Equation (4.20) can be easily derived once Equation (4.18) is substituted into Equation (4.14).

$$\sum_{r=1}^{N} \phi_r \mathbf{A}_r = \mathbf{I} \tag{4.20}$$

Equations (4.19)-(4.20) show that the values of ϕ_r, $\mathbf{C}_r$ and $\mathbf{A}_r$ must be determined or estimated to obtain the value of $\mathbf{C}_{\text{eff}}$. In general, the constituents of a composite are known which means the values of ϕ_r and $\mathbf{C}_r$ can be either determined in the laboratory or readily available in the literature. It is highlighted here that although the value of $\mathbf{A}_r$ to a certain extent can also be measured by sophisticated technologies such as digital image processing, smart sensors, etc., they are not frequently available to pavement engineers and researchers. The central idea behind CBMM is primarily to calculate the value of $\mathbf{A}_r$.

4.2.3 Localization tensors of different CBMM

4.2.3.1 *Eshelby's solution*

In Eshelby's solution (see Figure 4.2), the strain of the inclusion $<\boldsymbol{\varepsilon}>_2$ and the strain at infinity $<\boldsymbol{\varepsilon}>_0$ are related using Equation (4.21).

$$<\boldsymbol{\varepsilon}>_2 = \mathbf{T} :< \boldsymbol{\varepsilon}>_0 \tag{4.21}$$

with

$$\mathbf{T} = [\mathbf{I} + \mathbf{S}_1 : (\mathbf{C}_1)^{-1} : (\mathbf{C}_2 - \mathbf{C}_1)]^{-1} \tag{4.22}$$

where $\mathbf{C}_1$ and $\mathbf{C}_2$ are the stiffness tensors of the matrix and the inclusion, respectively; and $\mathbf{S}_1$ is known as Eshelby's fourth-order tensor.
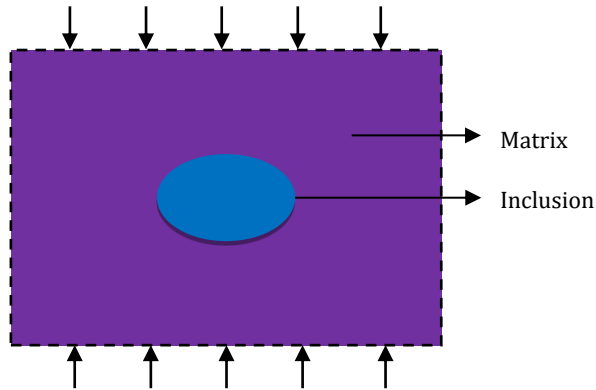
Figure 4.2 Eshelby's inhomogeneity problem

The value of $\mathbf{S_1}$ is a function of the matrix's mechanical properties and the inclusion's mechanical and geometrical properties (Wu, 1966, Walpole, 1969, Tandon and Weng, 1984, Mura, 1982). When the matrix and the inclusion are isotropic materials and the inclusion is a sphere, $\mathbf{S_1}$ is calculated as

$$\mathbf{S}_1 = \alpha_1 \mathbf{I}^{\mathrm{v}} + \beta_1 \mathbf{I}^{\mathrm{d}} \tag{4.23}$$

with

$$\alpha_1 = \frac{3K_1}{3K_1 + 4G_1}, \beta_1 = \frac{6(K_1 + 2G_1)}{5(3K_1 + 4G_1)} \tag{4.24}$$

where K_1 denotes the matrix's bulk modulus, and G_1 denotes the matrix's shear modulus.

4.2.3.2 *The Dilute model*

The Dilute model is developed directly from Eshelby's solution. For an *N*-phase composite, the value of $\mathbf{A}_r$ for each inclusion phase (from phase 2 to phase *N*) is identical to $\mathbf{T}$ by replacing $\mathbf{C}_2$ in Equation (4.22) with $\mathbf{C}_r$, see Equation (4.25). The value of $\mathbf{A}_1$ is further obtained by using Equation (4.20).

$$\mathbf{A}_r = [\mathbf{I} + \mathbf{S}_1 : (\mathbf{C}_1)^{-1} : (\mathbf{C}_r - \mathbf{C}_1)]^{-1}, r = 2, 3, ..., N \tag{4.25}$$

When all the phases are isotropic, and the inclusions are spherical, the effective bulk modulus K_{eff} and effective shear modulus G_{eff} of the composite are calculated using Equations (4.26) and (4.27), respectively.

$$K_{\text{eff}} = K_1 + \sum_{r=2}^{N} \frac{\phi_r (K_r - K_1)(3K_1 + 4G_1)}{3K_r + 4G_1} \tag{4.26}$$

$$G_{\text{eff}} = G_1 + \sum_{r=2}^{N} \frac{5\phi_r G_1 (G_r - G_1)(3K_1 + 4G_1)}{3K_1(3G_1 + 2G_r) + 4G_1(2G_1 + 3G_r)} \tag{4.27}$$

4.2.3.3 *SC model*

In the SC model, the inclusion itself is embedded into an infinite medium with the same properties as the composite itself, see Figure 4.3. The value of $\mathbf{A}_r$ for each inclusion phase is obtained by replacing the mechanical properties of the matrix in Equation (4.22) with the unknown mechanical properties of the composite ($\mathbf{C}_{\text{eff}}$), see Equation (4.28). The value of $\mathbf{A}_1$ can still be obtained from Equation (4.20).

$$\mathbf{A}_r = [\mathbf{I} + \mathbf{S}_{\text{eff}} : (\mathbf{C}_{\text{eff}})^{-1} : (\mathbf{C}_r - \mathbf{C}_{\text{eff}})]^{-1}, r = 2, 3, ..., N \tag{4.28}$$
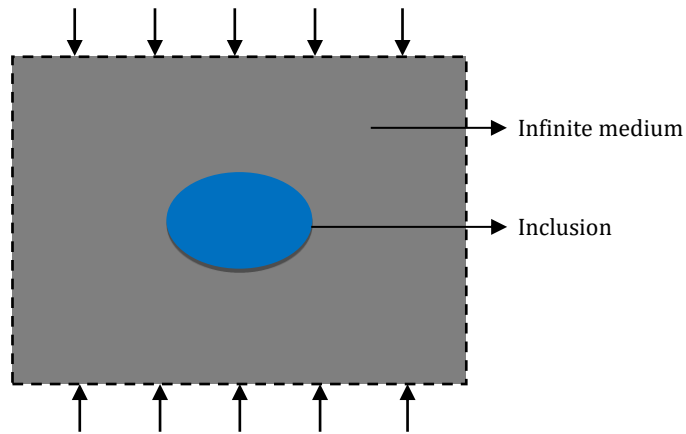
Figure 4.3 Illustration for the SC model

K_{eff} and G_{eff} for isotropic and spherical inclusions can be calculated using Equations (4.29)-(4.30). The expressions of K_{eff} and G_{eff} are not explicit, and thus numerical techniques should be used to solve these equations.

$$K_{\text{eff}} = K_1 + \sum_{r=2}^{N} \frac{\phi_r (K_r - K_1)(3K_{\text{eff}} + 4G_{\text{eff}})}{3K_r + 4G_{\text{eff}}} \tag{4.29}$$

$$G_{\text{eff}} = G_1 + \sum_{r=2}^{N} \frac{5\phi_r G_{\text{eff}}(G_r - G_1)(3K_{\text{eff}} + 4G_{\text{eff}})}{3K_{\text{eff}}(3G_{\text{eff}} + 2G_r) + 4G_{\text{eff}}(2G_{\text{eff}} + 3G_r)} \tag{4.30}$$

4.2.3.4 *GSC model/Three-phase model*

The geometrical description of a composite in the GSC model (or three-phase model) is similar to that in the SC model, while the only difference is that the inclusion is surrounded by a matrix layer, see Figure 4.4. It is noted here that although it seems that the model contains three phases, in reality, it is only suitable for a two-phase composite as the infinite medium is the composite itself.
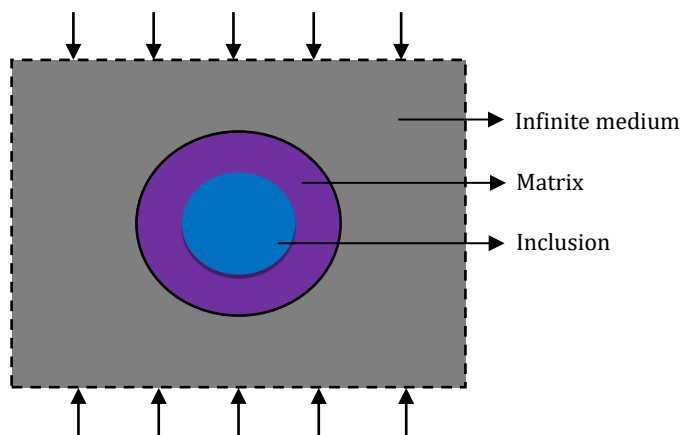
Figure 4.4 Illustration for the GSC model

Regarding an isotropic and spherical inclusion, the solutions for the values of K_{eff} and G_{eff} of a two-phase composite are given as Equations (4.31) and (4.32), respectively.

$$K_{\text{eff}} = K_1 + \frac{\phi_2 (K_2 - K_1)(3K_1 + 4G_1)}{3K_1 + 4G_1 + 3\phi_1 (K_2 - K_1)} \tag{4.31}$$

$$A\left(\frac{G_{\text{eff}}}{G_1}\right)^2 + B\left(\frac{G_{\text{eff}}}{G_1}\right) + C = 0 \tag{4.32}$$

Coefficients of A, B and C can be obtained using the following equations:

$$A = 8(G_2/G_1 - 1)(4 - 5\nu_1)\eta_1\phi_2^{10/3} - 2\left[63(G_2/G_1 - 1)\eta_2 + 2\eta_1\eta_3\right]\phi_2^{7/3} + 252(G_2/G_1 - 1)\eta_2\phi_2^{5/3}$$
$$- 25(G_2/G_1 - 1)(7 - 12\nu_1 + 8\nu_1^2)\eta_2\phi_2 + 4(7 - 10\nu_1)\eta_2\eta_3$$
$$B = -4(G_2/G_1 - 1)(1 - 5\nu_1)\eta_1\phi_2^{10/3} + 4\left[63(G_2/G_1 - 1)\eta_2 + 2\eta_1\eta_3\right]\phi_2^{7/3} - 504(G_2/G_1 - 1)\eta_2\phi_2^{5/3}$$
$$+ 150(G_2/G_1 - 1)(3 - \nu_1)\nu_1\eta_2\phi_2 + 3(15\nu_1 - 7)\eta_2\eta_3$$
$$C = 4(G_2/G_1 - 1)(5\nu_1 - 7)\eta_1\phi_2^{10/3} - 2\left[63(G_2/G_1 - 1)\eta_2 + 2\eta_1\eta_3\right]\phi_2^{7/3} + 252(G_2/G_1 - 1)\eta_2\phi_2^{5/3}$$
$$+ 25(G_2/G_1 - 1)(\nu_1^2 - 7)\eta_2\phi_2 - (7 + 5\nu_1)\eta_2\eta_3$$

where

$$\eta_1 = (G_2/G_1 - 1)(49 - 50\nu_1\nu_2) + 35(G_2/G_1)(\nu_2 - 2\nu_1) + 35(2\nu_2 - \nu_1)$$
$$\eta_2 = 5\nu_2(G_2/G_1 - 8) + 7(G_1 + G_2 + 4)$$
$$\eta_3 = (G_2/G_1)(8 - 10\nu_1) + (7 - 5\nu_1)$$

G_1 and G_2 = the shear moduli of the matrix and the inclusion, respectively;

ν_1 and ν_2 = the Poisson's ratios of the matrix and the inclusion, respectively;

ϕ_2 = the volume fraction of the inclusion.

4.2.3.5 *MT model*

The MT model assumes that inclusions are included into a finite matrix, Figure 4.5, and it is assumed that the value of $<\varepsilon>_r$ for each inclusion phase is calculated from Equation (4.33).

$$<\varepsilon>_r = \mathbf{T}_r :<\varepsilon>_1, r = 2,3,...,N \tag{4.33}$$

where $\mathbf{T}_r$ is identical to $\mathbf{T}$ by replacing $\mathbf{C}_2$ with $\mathbf{C}_r$ in Equation (4.22). By substituting Equation (4.33) into Equation (4.14), $<\varepsilon>_1$ is related to $<\varepsilon>_c$ via Equation (4.34). From Equation (4.34), the value of $\mathbf{A}_1$ is directly obtained as Equation (4.35); whereas the value of $\mathbf{A}_r$ for each inclusion phase is obtained by combining Equations (4.33) and (4.34), see Equation (4.36).

$$<\varepsilon>_1 = \left(\phi_1\mathbf{I} + \sum_{r=2}^{N}\phi_r\mathbf{T}_r\right)^{-1} :<\varepsilon>_c \tag{4.34}$$

$$\mathbf{A}_1 = \left(\phi_1\mathbf{I} + \sum_{r=2}^{N}\phi_r\mathbf{T}_r\right)^{-1} \tag{4.35}$$

$$\mathbf{A}_r = \mathbf{T}_r : \left(\phi_1\mathbf{I} + \sum_{r=2}^{N}\phi_r\mathbf{T}_r\right)^{-1}, r = 2,3,...,N \tag{4.36}$$
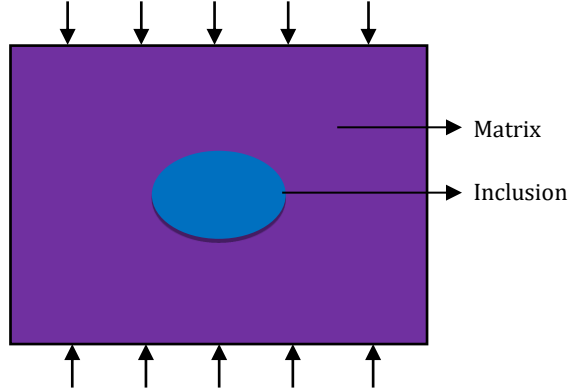
Figure 4.5 Illustration for the MT model

The values of K_{eff} and G_{eff} for isotropic and spherical inclusions can be calculated from Equations (4.37) and (4.38), respectively. It is highlighted that when N=2 the solution for K_{eff} in Equation (4.37) is the same as that in Equation (4.31).

$$K_{eff} = K_1 + \sum_{r=2}^{N} \frac{\phi_r (K_r - K_1)(3K_1 + 4G_1)}{\phi_1 (3K_r + 4G_1) + \sum_{s=2}^{N} \phi_s \dfrac{(3K_1 + 4G_1)(3K_r + 4G_1)}{(3K_s + 4G_1)}} \tag{4.37}$$

$$G_{eff} = G_1 + \sum_{r=2}^{N} \frac{5\phi_r G_1 (G_r - G_1)(3K_1 + 4G_1)}{\phi_1 B_r + \sum_{s=2}^{N} \phi_s \dfrac{5G_1(3K_1 + 4G_1)B_r}{B_s}} \tag{4.38}$$

$$B_r = 5G_1(3K_1 + 4G_1) + 6(K_1 + 2G_1)(G_r - G_1)$$

4.2.3.6 *Differential scheme*

The DS approach is another method to deal with the inter-particle interaction in a high concentrated composite. The idea behind this model is to develop a process where the inclusions are added in steps, and thus the interactions can be neglected (McLaughlin, 1977, Norris, 1985), see Figure 4.6.

For a three-phase composite, the value of $\mathbf{C}_{eff}$ can be expressed using the following equation:

$$\frac{d\mathbf{C}_{eff}}{d\phi} = \frac{1}{1-\phi}\left[\frac{\phi_2^{(c)}}{\phi^{(c)}}\left(\mathbf{C}_2 - \mathbf{C}_{eff}\right) : \mathbf{A}_2(\mathbf{C}_{eff}) + \frac{\phi_3^{(c)}}{\phi^{(c)}}\left(\mathbf{C}_3 - \mathbf{C}_{eff}\right) : \mathbf{A}_3(\mathbf{C}_{eff}) \right] \tag{4.39}$$

where ϕ is the sum of the inclusion phases' volume fractions, $\phi_2 + \phi_3$; the superscript "c" indicates the final composite; the value of $\mathbf{A}$ can be obtained through any of the above models (Yin and Zhao, 2016).
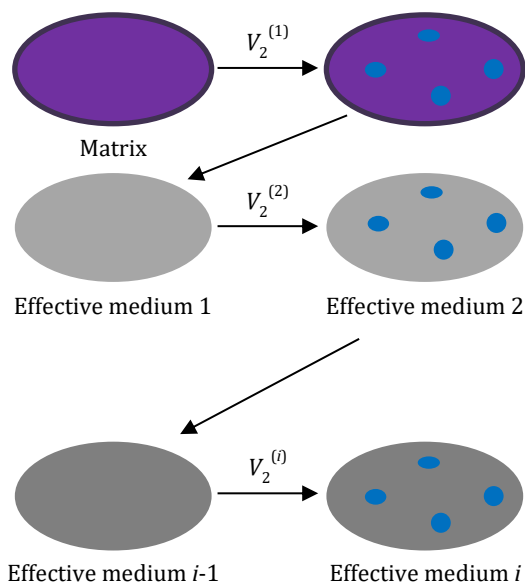
Figure 4.6 Illustration of the DS approach

Equation (4.39) can be solved numerically by discretizing it as Equation (4.40):

$$\mathbf{C}_{\text{eff}}^{(i)} = \mathbf{C}_{\text{eff}}^{(i-1)} + \frac{\Delta\phi_2^{(i)}}{1-\phi^{(i-1)}}\left(\mathbf{C}_2 - \mathbf{C}_{\text{eff}}^{(i-1)}\right):\mathbf{A}_2^{(i-1)} + \frac{\Delta\phi_3^{(i)}}{1-\phi^{(i-1)}}\left(\mathbf{C}_3 - \mathbf{C}_{\text{eff}}^{(i-1)}\right):\mathbf{A}_3^{(i-1)} \qquad (4.40)$$

where the superscripts "i" and "i-1" represent step i and step i-1, respectively; $\Delta\phi_2$ and $\Delta\phi_3$ are the increments of the volume fractions of the inclusion phases. In this research work, after the sensitivity analysis of the effect of different calculation steps on the predicted results, a total of 50 steps were finally conducted to calculate the value of $\mathbf{C}_{\text{eff}}$. The initial condition for $\mathbf{C}_{\text{eff}}$ was that when ϕ=0, $\mathbf{C}_{\text{eff}}$=$\mathbf{C}_1$. For each step, the values of $\Delta\phi_2$ and $\Delta\phi_3$ were identical to ϕ_2/50 and ϕ_3/50, respectively.

4.2.4 General solution procedure for viscoelastic composites

All the CBMM described above are originally developed for elastic composites; however, asphalt materials are mostly treated as viscoelastic composites. This means that these models may not be directly applicable to asphalt materials. Therefore, this section describes a typical procedure that can be adapted to utilize the above models for viscoelastic composites.

According to the research work of Hashin (Hashin, 1965, Hashin, 1970), micromechanical models can be utilized for viscoelastic materials via the elastic-viscoelastic correspondence principle (Bland, 1960). Since the viscoelastic properties of asphalt materials in this study were measured in the frequency domain, the general

solution procedure in the frequency domain will be described here. In the following part, a two-phase composite is taken as an example, and it is assumed that the matrix (phase 1) is a viscoelastic material while the inclusion (phase 2) is an elastic material. The equations of the Dilute model (Equations (4.26)-(4.27)) for calculating the moduli of a composite are taken as examples to show the change of the formulas with the consideration of viscoelasticity.

In the frequency domain, the complex bulk modulus $K_1^*(\omega)$ and the complex shear modulus $G_1^*(\omega)$ of phase 1 can directly replace K_1 and G_1, respectively. Since phase 2 is an elastic material, the moduli of this phase (K_2 and G_2) are left unchanged, see Equations (4.41) and (4.42).

$$K_{\text{eff}}^*(\omega) = K_1^*(\omega) + \frac{\phi_2(K_2 - K_1^*(\omega))(3K_1^*(\omega) + 4G_1^*(\omega))}{3K_2 + 4G_1^*(\omega)} \tag{4.41}$$

$$G_{\text{eff}}^*(\omega) = G_1^*(\omega) + \frac{5\phi_2 G_1^*(\omega)(G_2 - G_1^*(\omega))(3K_1^*(\omega) + 4G_1^*(\omega))}{3K_1^*(\omega)(3G_1^*(\omega) + 2G_2) + 4G_1^*(\omega)(2G_1^*(\omega) + 3G_2)} \tag{4.42}$$

where K_{eff}^* and G_{eff}^* are the complex bulk and shear moduli of the composite, respectively.

The calculated values of K_{eff}^* and G_{eff}^* can be further represented in terms of dynamic moduli (the absolute values of complex moduli) and phase angle. It is noted here that in some research studies, dynamic moduli are taken as the corresponding elastic moduli to be used in the formulas of micromechanical models (Buttlar, 1996, Shashidhar and Shenoy, 2002, Kim and Little, 2004). However, this method can only obtain the effective dynamic moduli but not the phase angle of the composite.

Using the introduced CBMM above, both the upscaling of mastic's properties and the upscaling of a mix's properties were implemented in this study. Since the volume fraction of the inclusions in mastic (the volume fraction of filler is 26.3%) is much lower than that in a mix (the volume fraction of coarse aggregates in PA mix-1 is 62%), the comparison of the upscaling results between these two materials can be used to evaluate the performance of CBMM at different inclusion concentrations.

4.3 Upscaling of mastic's properties

Figure 4.7a and Figure 4.7b show the comparison of the predicted shear modulus $|G_{\text{mas}}^*|$ and phase angle δ_{mas} of mastic against the experimental results (labelled as "Mastic"), respectively. In general, it can be observed that the predicted $|G_{\text{mas}}^*|$-f curve and δ_{mas}-f curve follow the same shapes as those from laboratory tests. To clearly look into the performance of each model, the values of $|G_{\text{mas}}^*|/|G_b|$ and $\delta_{\text{mas}}/\delta_b$ were calculated, see Figure 4.7c and Figure 4.7d.

a. Dynamic shear modulus of mastic

b. Phase angle of mastic

c. Ratio of mastic's modulus to binder's modulus

d. Ratio of mastic's phase angle to binder's phase angle
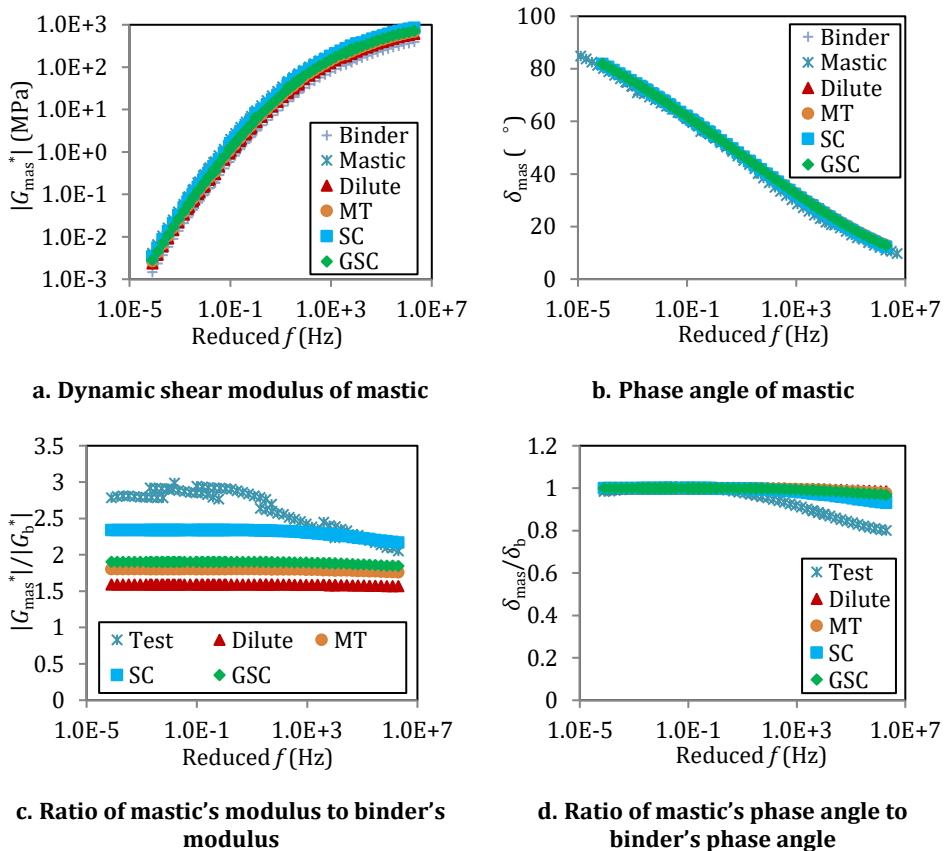
Figure 4.7 Upscaling from asphalt binder to mastic using different CBMM

It can be seen that the SC model performs better over other models, while the Dilute model provides the worst predictions. The poor performance of the Dilute model can be accounted for by the fact that its strain localization tensor is obtained directly from Eshelby's solution in which the matrix phase is considered as infinite. Therefore, the Dilute model is only suitable for composites where the volume fractions of inclusions are low enough to neglect the interaction of the stress/strain fields disturbed by different inclusions (known as the "inter-particle interaction").

4.4 Upscaling of a mix's properties

This section shows the performance of CBMM in predicting the mechanical properties of PA mixes. The analyses of the sensitivity of the predictions' accuracy to the (1) the scale of the matrix phase (i.e. asphalt binder, mastic, and mortar); (2) the use of different micromechanical models; (3) the utilization of the DS approach; and (4) the Poisson's ratio of the matrix phase were presented as follows.

4.4.1 Sensitivity to the matrix phase

Asphalt binder, mastic, and mortar can all be used as the matrix phase to predict the properties of a mix. In this study, the effect of the scale of the matrix phase on the accuracy of the predictions was investigated. This investigation can help understand the relations of a mix's behaviour to the behaviour of its different scale constituents. Furthermore, based on the obtained results, the most suitable matrix can be selected to predict the properties of PA mixes.

The Dilute model was used as an example for this analysis. The calculated results of $|E_{mix}^*|$ and δ_{mix} of PA mix-1 were compared to the experimental results in Figure 4.8. It can be seen that both for $|E_{mix}^*|$ and δ_{mix}, upscaling from a higher scale matrix provides more accurate predictions than that from a lower scale matrix. This can be explained by the following two facts:

- In comparison to a lower scale matrix, more aggregate particles are included in a higher scale matrix. Therefore, the concentration of inclusions decreases, and thus the accuracy of the predictions improves.

- When a higher scale matrix is used for upscaling, the inaccuracy in the prediction from the lower scale matrix to the higher scale matrix is avoided because the properties of the higher scale matrix are accurately measured from laboratory tests.

a. Dynamic Young's modulus   b. Phase angle
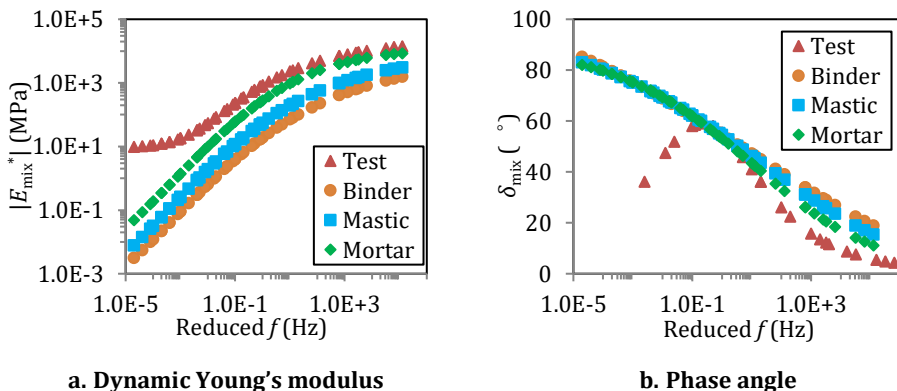
Figure 4.8 Predicted Young's modulus of PA mix-1 from materials at different scales

Since upscaling from mortar provides the most accurate predictions, it was chosen as the matrix phase for further analyses.

4.4.2 Sensitivity to different CBMM

A comparison of $|E_{mix}^*|$ and δ_{mix} between the predicted results and the experimental values (labelled as "Mix") is shown in Figure 4.9. It is noted that for the GSC model, the solutions to the moduli of a three-phase mix are too cumbersome to be solved analytically (Benveniste, 2008). Therefore, In order to employ the classical two-phase GSC model for a three-phase mix, researchers (Pichler et al., 2012) typically divide the prediction procedure into two steps: 1) either the aggregate phase or the air void phase is added into the matrix phase; 2) the other phase is added into the composite obtained from the previous step. In this research study, both orders of phase additions were considered. In Figure 4.9, "GSC 1" represents the case where aggregates were added first while "GSC 2" represents the case in which air voids were added first.

a. Dynamic Young's modulus of PA mix-1   **b. Phase angle of PA mix-1**

c. Dynamic Young's modulus of PA mix-2   **d. Phase angle of PA mix-2**

Figure 4.9 Upscaling from mortar to PA mix using different CBMM

Among all the models, the SC model performs the worst since its predictions are almost independent of frequencies. This is quite different from the former case where this model provided the most accurate predictions for mastic. These different performances of the SC model can be explained by the fact that in the SC model, the

predictions are always controlled by the phase with the highest concentration. Therefore, for the mastic with a low concentration of filler particles, the predicted results are controlled by the frequency-dependent properties of asphalt binder, while for the mix with a high concentration of aggregate particles, the frequency-independent properties of aggregates control the predictions.

Except for the SC model, all the other models still just provide matrix-like properties of a mix that the predicted $|E_{mix}^*|$-f and δ_{mix}-f curves follow the same shapes as those of the matrix phase. At high frequencies, the behaviour of the matrix phase is similar to that of the mix, and thus all the models perform well in terms of the shapes of the predictions. In terms of the magnitude of the predictions, the Dilute model results in the lowest values of $|E_{mix}^*|$ while the GSC1 model produces the highest. However, it can also be observed that the predicted values from the GSC2 model are much lower than those from the GSC1 model. This indicates that when the two-phase GSC model is used for a three-phase composite, the predictions depend on the order of adding different phases.
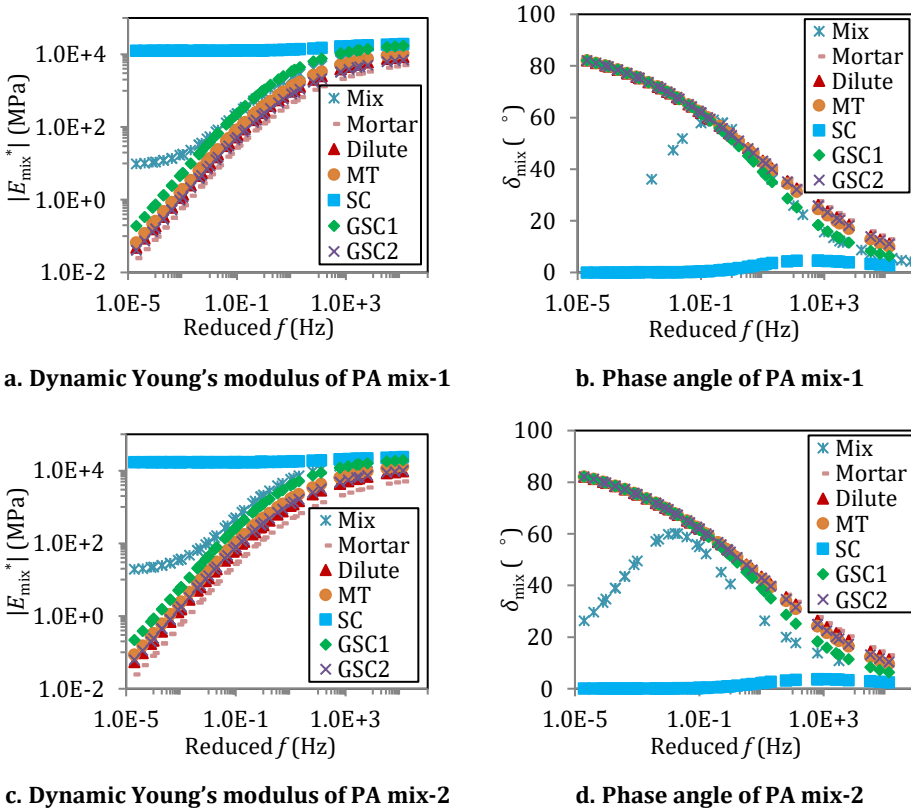
Further investigation of the figures shows that CBMM perform better in predicting the modulus of PA mix-1 than their performances for PA mix-2. For example, at higher frequencies, the predicted values of $|E_{mix}^*|$ and δ_{mix} from the GSC1 model almost match the experimental results of PA mix-1, while for PA mix-2, the predictions show notable differences (lower values of $|E_{mix}^*|$ and higher values of δ_{mix}) over the experimental values. From Chapter 2, it was known that more compaction effort was performed on PA mix-2 than that performed on PA mix-1. As a consequence, a denser aggregates pack formed in PA mix-2. Therefore, the better performance of CBMM for PA mix-1 over PA mix-2 indicates that CBMM is more suitable for mixes with less densely packing aggregate particles.

It can also be observed that the performances of all the models at low frequencies are much worse than their performances at high frequencies. The experimental results of $|E_{mix}^*|$ show an asymptotic behaviour while the predicted values show a continuous decrease. The measured values of δ_{mix} decrease after reaching a peak value, whereas the predictions keep increasing. Furthermore, except for the SC model, all the models significantly underestimate $|E_{mix}^*|$ and overestimate δ_{mix}.

Overall, comparing the performances of CBMM in predicting the properties of mastic to their performances for a mix, better performance for mastic against a mix is found. This can be associated with the fact that these models were primarily developed to account for the stiffening effect caused by the embedded inclusions in a mix with minimal particle interactions. In other words, these models tend to be applicable for dispersed suspensions, the behaviour of which is dominated by the matrix phase. Since mortar is expected to be a dispersed suspension while for PA mixes, particularly at lower frequencies, a dispersed suspension is not expected because of the packing

aggregates, the predicted results by these models are acceptable for mastic, but for mixes, they are inaccurate.

In order to address the above issue, micromechanical modelling based upon the DS approach was further conducted. It is expected that this method can avoid the interactions between aggregate particles, and thus it can provide better predictions. In the following section, the applicability of this scheme will be judged in the context of PA mixes.

4.4.3 Effect of the DS approach

The predicted results of $|E_{mix}^*|$ and δ_{mix} of PA mix-1 on the basis of the DS approach are shown in Figure 4.10a-e. In order to understand the difference between the DS approach and the Non-DS approach, the plots from the Non-DS approach (Figure 4.9) are plotted against predictions by the DS approach in the same figures.
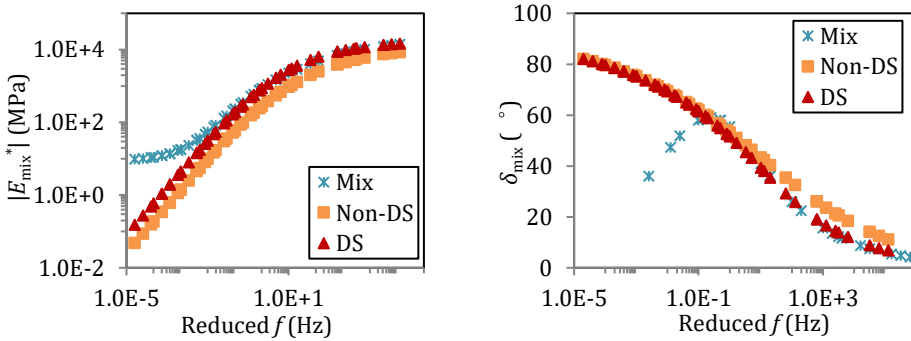
a. Dilute model
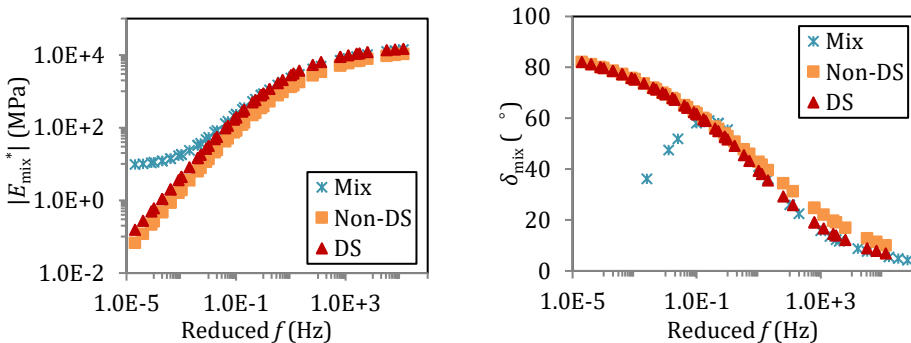
b. MT model
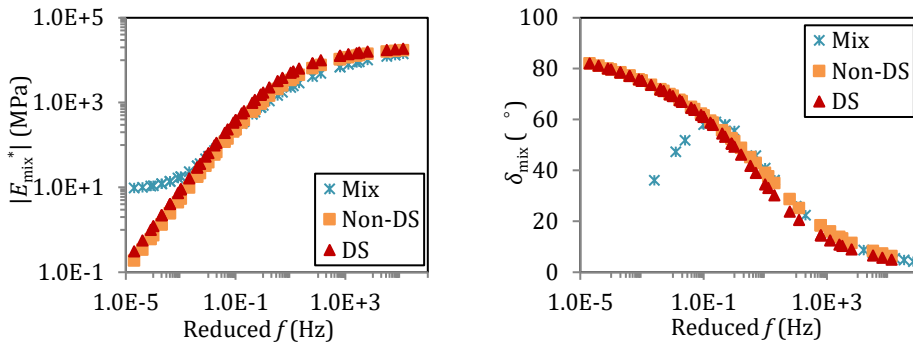
c. GSC-1 model
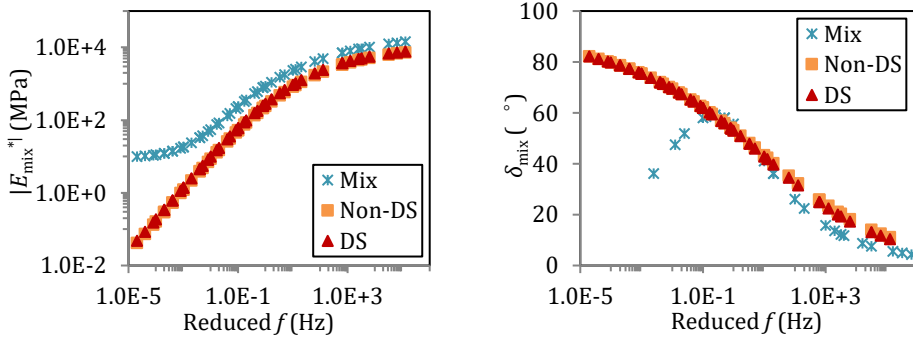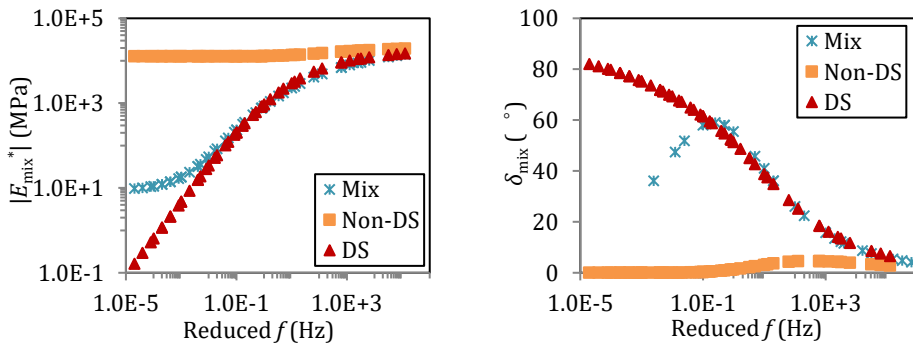
d. GSC-2 model

e. SC model

Figure 4.10 Effect of the DS approach on the performance of micromechanical models

It can be observed that with the exception of the GSC 2 model, the performance of all the models improves significantly, especially at higher frequencies. However, it is also observed that the DS approach does not change the shape of the curve, but more or less has a scaling effect. At lower frequencies, even the DS approach fails to predict

$|E_{mix}^*|$ and δ_{mix} accurately. The failure of the DS can be attributed to the fact that it does not change the fundamental theory of the micromechanical models.

Furthermore, the performances of different CBMM after the introduction of the DS approach were compared, see Figure 4.11. It can be seen that with the utilization of the DS approach, the predictions from the Dilute model, the MT model, and the SC model are quite similar to each other. This can be explained by the fact that all these models are originally developed on the basis of the same fundamental theory, Eshelby's solution. When the volume fractions of the inclusions are quite small, and thus the inter-particle interactions can be ignored, the predicted properties of a composite using different micromechanical models all have the same limits as the values given by Eshelby's solution.

a. Dynamic modulus of PA mix-1   **b. Phase angle of PA mix-1**

c. Dynamic modulus of PA mix-2   **d. Phase angle of PA mix-2**
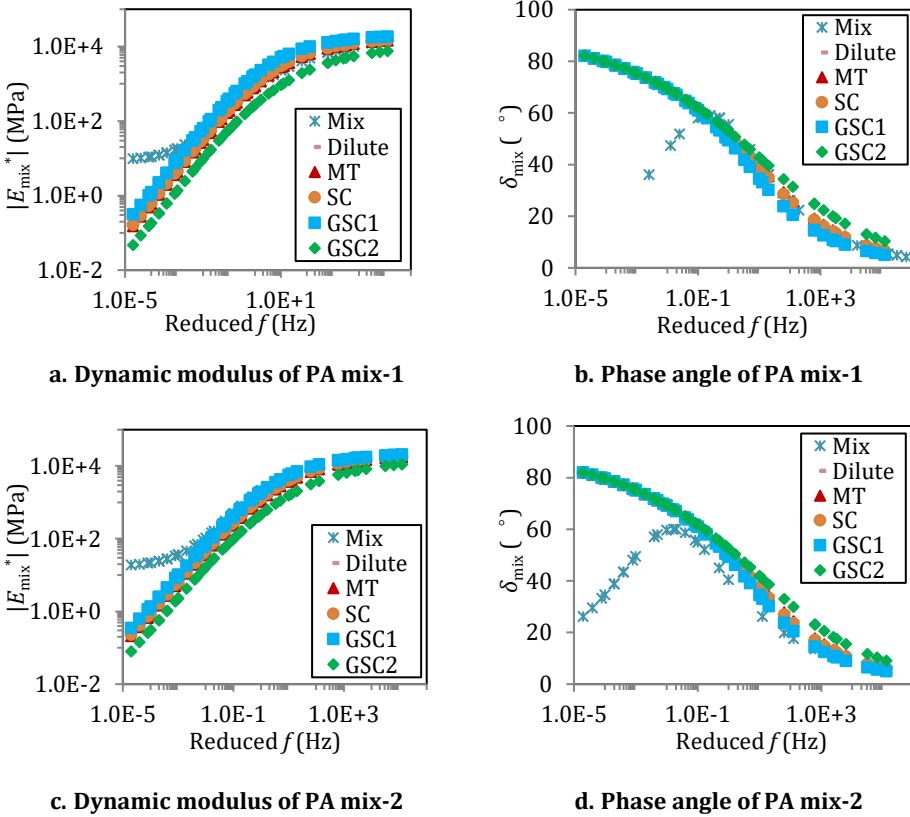
Figure 4.11 Comparison of the performance of CBMM using the DS approach

Figure 4.11 also shows that the utilization of the DS approach does not affect the difference in the predictions resulting from the order of adding different inclusion phases. The predicted values of $|E_{mix}^*|$ using the GSC-1 model where the aggregate phase

is added first are still significantly higher than those using the GSC-2 model where the air voids phase is the first phase to add.

Apart from the introduction of the DS approach, further investigation was also conducted regarding the Poisson's ratio of the mortar to examine if the accuracy of the predictions can be improved.

4.4.4 Sensitivity of predicted modulus to mortar's Poisson's ratio

The Poisson's ratio of an asphalt matrix (asphalt binder, mastic, and mortar) used in the literature typically ranges from 0.35 to 0.5 (Underwood and Kim, 2014). Thus, three different values of the mortar's Poisson's ratio v_{mor}, 0.3, 0.4, and 0.49999, were used in the sensitivity analysis. It is noted that the bulk modulus of mortar K_{mor} is calculated as infinity when v_{mor} is equal to 0.5. Thus, to avoid dealing with an infinite value in the calculation, a value of v_{mor} that approaches 0.5 was used.
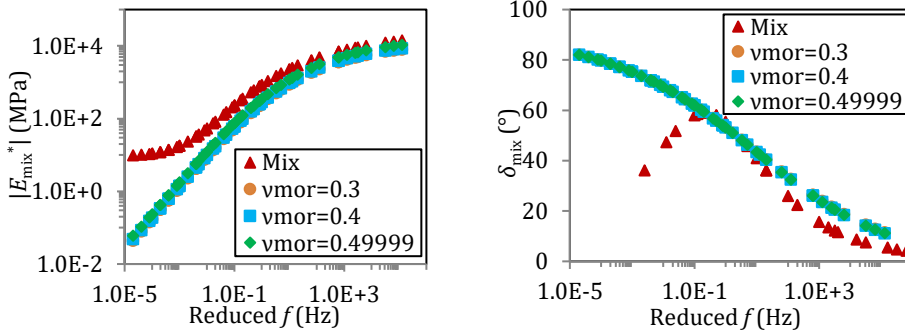
a. Dilute model
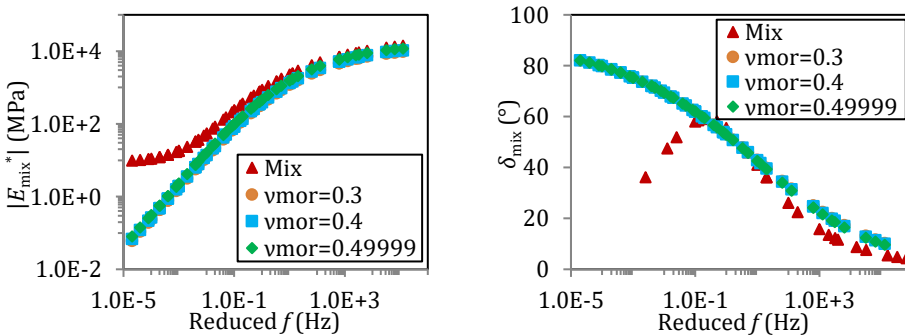
b. MT model
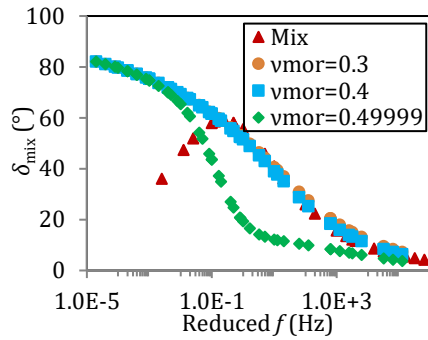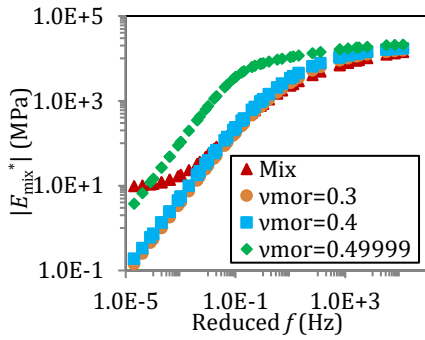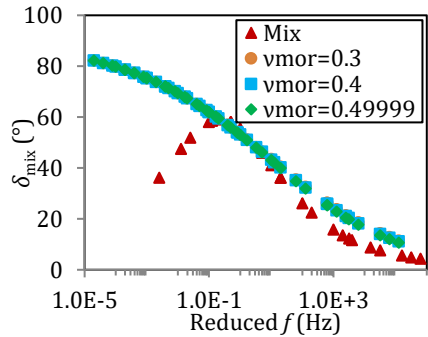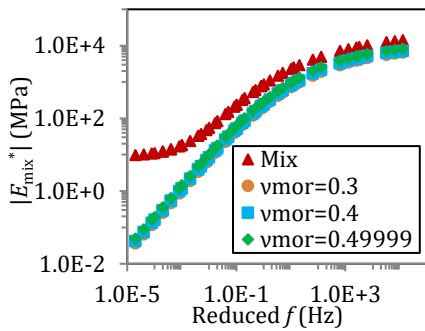
c. GSC 1 model

d. GSC 2 model
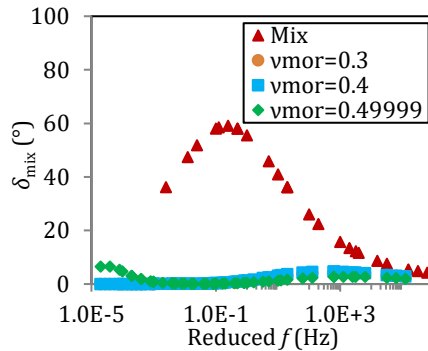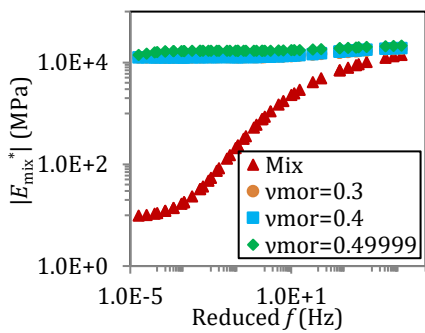
e. SC model
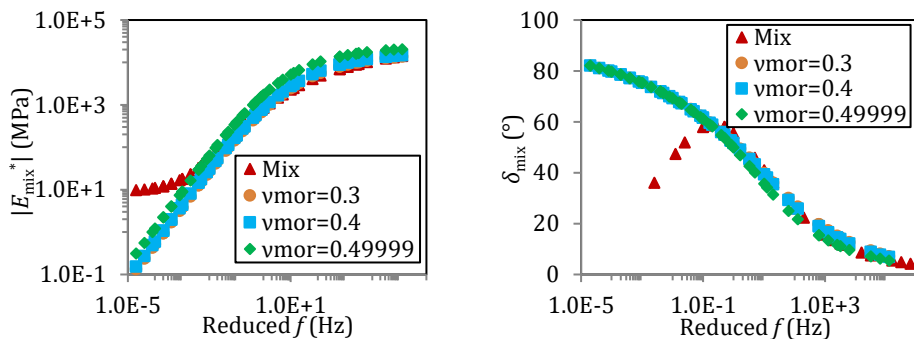
f. Dilute model using the DS approach

Figure 4.12 Sensitivity of predicted modulus to mortar's Poisson's ratio

The predicted results of $|E_{mix}^*|$ and δ_{mix} for PA mix-1 are shown in Figure 4.12. Except for the GSC 1 model, the change of ν_{mor} does not significantly affect the predictions. For the GSC 1 model, although the values of $|E_{mix}^*|$ and δ_{mix} change substantially when the value of ν_{mor} increases from 0.4 to 0.5, the predictions still cannot match the experimental results.

On the basis of all the above discussions, it can be concluded that regardless of the scale of the matrix phase, the utilization of the DS approach, or the change of the matrix's Poisson's ratio, CBMM are not capable of accurately predicting the mechanical properties of PA mixes, especially at lower frequencies. This observation may be different from the result obtained by other researchers (Underwood and Kim, 2013) that when mortar was used as the matrix phase, accurate predictions could be obtained from CBMM in a wide frequency range (even at high temperatures). In the author's opinion, depending on the properties of the mortar, both observations can be valid. In this study, the mortar contained a high content of asphalt binder, and thus it showed liquid-like behaviour which was quite different from the behaviour of the mix. Since most CBMM can only shift the matrix modulus curves without changing their shapes, it is not expected that the predicted properties of the mix can agree with the experimental results. On the other hand, in the study of other researchers (Underwood and Kim, 2013), since mortar behaved quite similar to the mix, it was not surprising that using mortar as the matrix phase, accurate predictions were obtained.

Realizing the limitations of CBMM, it is important to further understand the reasons behind these limitations since it benefits the development of a new micromechanical model for accurately predicting the mechanical properties of PA mixes. Therefore, in the following section, explanations for the limitations of CBMM are discussed.

4.5 Explanations for the limitations of CBMM

In order to explain the limitations of CBMM, it is necessary to understand the mechanisms behind the stiffening of an asphalt material due to the addition of inclusions (known as "stiffening mechanisms"). In this section, the stiffening mechanisms of asphalt materials are discussed, on the basis of which, the limitations of the models are explained.

4.5.1 Stiffening mechanisms of asphalt materials

There are three generally accepted stiffening mechanisms for asphalt materials (Buttlar et al., 1999): the volume-filling stiffening effect, the physiochemical stiffening effect, and the stiffening effect of the particle-to-particle direct contact. The physical explanations of these mechanisms are presented as follows.

4.5.1.1 *Volume-filling stiffening effect*

The volume-filling stiffening effect can be explained as the stiffening due to the disturbance of the stress/strain fields in the soft matrix caused by the addition of stiff inclusion particles (Underwood, 2011). When the particles' concentration is very low, the disturbed area caused by each particle does not interact with each other, Figure 4.13a; while as the concentration increases, the disturbed areas caused by different particles may overlap and interact with each other, which is called as the "inter-particle interaction" as mentioned in the previous sections, Figure 4.13b.

a. Low concentration   b. High concentration
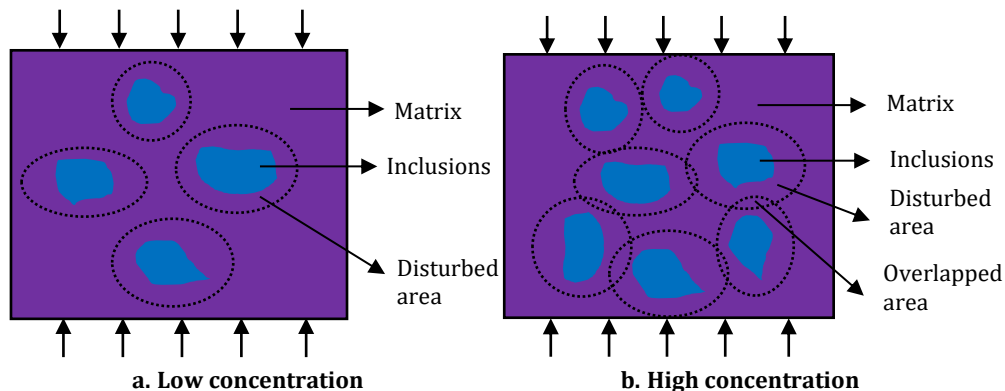
Figure 4.13 Disturbed areas caused by different inclusion particles

According to the above definition, it is obvious that the volume-filling stiffening effect is dependent on the volume fraction of the particles. In addition, the geometrical properties of the particles (i.e. the size, the shape, the angularity, etc.) make a major contribution as well.

4.5.1.2 *Physiochemical stiffening effect*
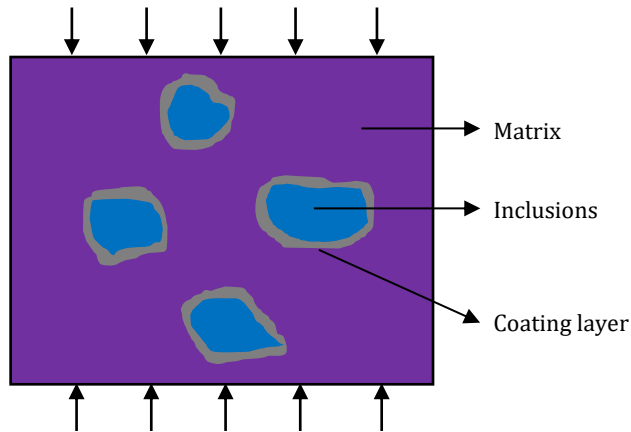
Figure 4.14 Illustration of the physiochemical stiffening effect

The physiochemical stiffening effect is defined as the stiffening because of the physicochemical interactions (i.e. absorption, adsorption, etc.) at the interface between the matrix and inclusion particles (Buttlar et al., 1999). These interactions yield coating layers around the inclusion particles, which increase the composite's stiffness (D.G., 1962), Figure 4.14.

The physiochemical stiffening effect is mainly affected by the geometrical and mineral characteristics of the inclusions. High surface area, rough surface texture, and high surface activity contribute to the increase of the composite's stiffness (Rigden, 1947, Anderson D. A., 1973, Little and Petersen, 2005, Faheem and Bahia, 2010, Craus et al., 1978).

4.5.1.3 *Stiffening effect of the particle-to-particle direct contacts*

The stiffening effect of the particle-to-particle direct contacts refers to the stiffening resulting from the contacts among different particles (Shashidhar and Shenoy, 2002, Buttlar et al., 1999). When the concentration of particles is low, the particles are randomly distributed within the matrix and do not contact each other, Figure 4.15a. Whereas, with the increase of the particles' concentration, a group of particles start touching each other and gradually form a skeleton framework (Underwood, 2011, Shashidhar and Shenoy, 2002), see Figure 4.15b. Due to the formation of the skeleton framework, the stiffness of the composite becomes much higher than the bulk matrix.

It is obvious that the stiffening effect of the particle-to-particle direct contacts depends on the particles' concentration. Apart from that, it also depends on the loading condition, the temperature/frequency of the material, the geometrical properties of the particles, etc.

a. Low concentration   **b. High concentration**
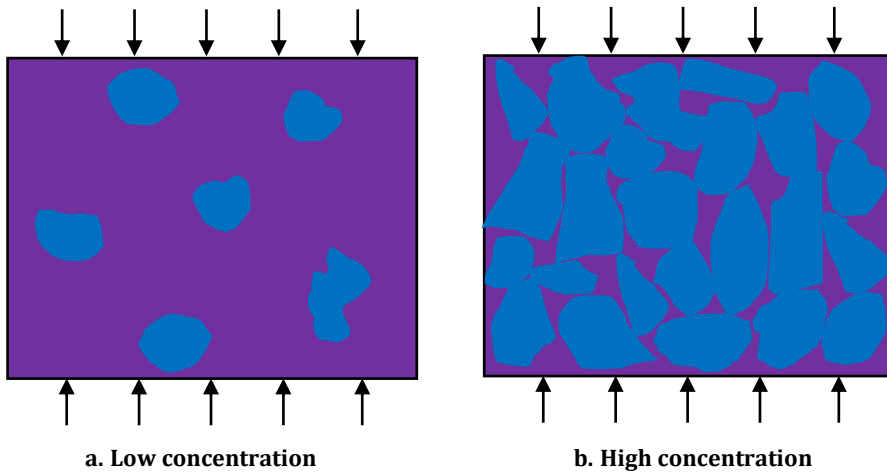
Figure 4.15 Particles' contacts at different concentrations

Overall, three different mechanisms result in the stiffening of asphalt material. It is highlighted here that at a certain condition, it is possible that all of these mechanisms simultaneously play important roles in the stiffening of the material. It is also possible that the material's overall behaviour is dominated by only one mechanism or two mechanisms, and the stiffening effects of the other(s) can be neglected. Therefore, in order to effectively predict an asphalt material's properties, it is important to figure out the dominant stiffening mechanism(s) beforehand.

4.5.2 Explanations for the poor performance of CBMM

Based upon the stiffening mechanisms of an asphalt mixture, the poor performance of CBMM in predicting the stiffness of a PA mix can be explained as follows.

- Concerning the upscaling from mortar to PA mixes, the physicochemical stiffening effect due to the addition of coarse aggregates can be neglected because it is generally considered that physicochemical interactions mainly occur between asphalt binder and filler particles. Therefore, the dominant stiffening mechanisms from mortar to mixes are the volume-filling stiffening effect and the stiffening effect of the particle-to-particle direct contacts.

- CBMM can only take into account the volume-filling stiffening effect to a certain extent (Yin et al., 2008, Underwood, 2011). These models only consider few factors that impact the stress and strain distributions, i.e. the shape of the inclusions (either spheres or ellipsoids). Other factors, such as the particles' locations or their relative configurations, the particles' size, irregular shape, angularity, etc., are not taken into consideration in the predictions.

- There are no particle contacts considered in CBMM, and thus, they cannot capture the stiffening effect of the particle-to-particle direct contacts at all (Yin et al., 2008).

4.6 Summary

This chapter comprehensively evaluated the performance of commonly used CBMM for predicting the modulus of mastic and PA mixes. More attention was given to the upscaling of a mix's properties where the sensitivities of the predictions' accuracy to (1) the scale of the matrix phase, (2) the utilization of the DS approach, and (3) the value of the matrix's Poisson's ratio were analysed. In order to explain the inaccuracy of the predicted results, the stiffening mechanisms of an asphalt material due to the addition of aggregate particles were described. On the basis of that, possible explanations for the limitations of CBMM were further discussed. Based on all the discussions, the following general conclusions can be made:

- CBMM performed better in predicting the modulus of a composite with a low concentration of inclusions (i.e. mastic) than their performances for a highly concentrated composite (i.e. mixes). This can be associated with the fact that these models were primarily developed to account for the stiffening effect caused by the embedded inclusions in a mix with minimal particle interactions.

- Upscaling from a higher scale matrix phase (i.e. mortar) provided more accurate predictions of a PA mix's properties than upscaling from a lower scale matrix phase (i.e. asphalt binder and mastic). This is because upscaling from a higher scale matrix phase means the addition of a lower volume fraction of inclusions, and it avoids the inaccuracy resulting from the prediction of the properties of the higher scale matrix phase.

- At higher frequencies, the predicted dynamic modulus and phase angle of a PA mix using different CBMM all followed the same shapes as those measured from laboratory tests. The predictions using the GSC model when the aggregate phase was added before the addition of the air voids phase were in the best agreement with the experimental values. Furthermore, at higher frequencies, better performances of CBMM were found in predicting the modulus of a mix with less densely packing aggregate particles (i.e. PA mix-1).

- The performance of CBMM at lower frequencies was much worse than that at high frequencies. None of the applied micromechanical models could adequately predict the mechanical properties of PA mixes. The shapes of the predicted dynamic modulus and phase angle were not consistent with experimental results, and moreover, in general, all the models significantly

underestimate the values of dynamic modulus and overestimate the values of phase angle.

- After the introduction of the DS approach, the accuracy of the predictions improved at higher frequencies, whereas at lower frequencies, it did not. This can be attributed to the fact that this scheme does not change the fundamental theory of the micromechanical models. Also, the accuracy of the predictions did not show a considerable increase by adjusting the Poisson's ratio of the matrix phase.

- The poor performance of CBMM in predicting the mechanical properties of a PA mix can be related to the facts that (1) CBMM cannot explicitly account for the volume-filling stiffening effect, and (2) they cannot capture the stiffening effect of the particle-to-particle direct contacts at all.

4.7 References

ABBAS, A., MASAD, E., PAPAGIANNAKIS, T. & SHENOY , A. 2005. Modelling asphalt mastic stiffness using discrete element analysis and micromechanics-based models. *International Journal of Pavement Engineering,* 6**,** 137-146.

ANDERSON D. A., G. W. H. 1973. Mechanical behavior and reinforcement of mineral fillerasphalt mixtures. *Proc., Association of Asphalt Paving Technologists,* 42**,** 37-66.

BENVENISTE, Y. 1987. A new approach to the application of Mori-Tanaka's theory in composite materials. *Mechanics of Materials,* 6**,** 147-157.

BENVENISTE, Y. 2008. Revisiting the generalized self-consistent scheme in composites: Clarification of some aspects and a new formulation. *Journal of the Mechanics and Physics of Solids,* 56**,** 2984-3002.

BLAND, D. R. 1960. *The theory of linear viscoelasticity*, Courier Dover Publications.

BUTTLAR, W., BOZKURT, D., AL-KHATEEB, G. & WALDHOFF, A. 1999. Understanding Asphalt Mastic Behavior Through Micromechanics. *Transportation Research Record: Journal of the Transportation Research Board,* 1681**,** 157-169.

BUTTLAR, W. G. R., R 1996. Evaluation of Empirical and Theoretical Models to Determine Asphalt Mixture Stiffnesses at Low Temperatures. *Journal of the Association of Asphalt Paving Technologists,* 65**,** 99-141.

CHRISTENSEN, R. M. & LO, K. H. 1979. Solutions for effective shear properties in three phase sphere and cylinder models. *Journal of the Mechanics and Physics of Solids,* 27**,** 315-330.

CRAUS, J., ISHAI, I. & SIDES, A. Some Physico-Chemical Aspects of the Effect and the Role of the Filler in Bituminous Paving Mixtures. Association of Asphalt Paving Technologists Proc, 1978. 558-588.

D.G., T. 1962. Review of Mineral Fillers. *Journal of Association of Asphalts Paving Technologists,* 3**,** 118-150.

ESHELBY, J. D. 1957. The determination of the elastic field of an ellipsoidal inclusion, and related problems. *Proceedings of the Royal Society of London. Series A. Mathematical and Physical Sciences,* 241**,** 376.

FAHEEM, A. F. & BAHIA, H. U. 2010. Modelling of Asphalt Mastic in Terms of Filler-Bitumen Interaction. *Road Materials and Pavement Design,* 11**,** 281-303.

HASHIN, Z. 1965. Viscoelastic Behavior of Heterogeneous Media. *Journal of Applied Mechanics,* 32**,** 630-636.

HASHIN, Z. 1970. Complex moduli of viscoelastic composites—I. General theory and application to particulate composites. *International Journal of Solids and Structures,* 6**,** 539-552.

HILL, R. 1965. A self-consistent mechanics of composite materials. *Journal of the Mechanics and Physics of Solids,* 13**,** 213-222.

HUIMING YIN, Y. Z. 2018. *Introduction to the Micromechanics of Composite Materials*.

KIM, Y.-R. & LITTLE, D. N. 2004. Linear Viscoelastic Analysis of Asphalt Mastics. *Journal of Materials in Civil Engineering,* 16**,** 122-132.

LITTLE, D. N. & PETERSEN, J. C. 2005. Unique Effects of Hydrated Lime Filler on the Performance-Related Properties of Asphalt Cements: Physical and Chemical Interactions Revisited. *Journal of Materials in Civil Engineering,* 17**,** 207-218.

MCLAUGHLIN, R. 1977. A study of the differential scheme for composite materials. *International Journal of Engineering Science,* 15**,** 237-244.

MORI, T. & TANAKA, K. 1973. Average stress in matrix and average elastic energy of materials with misfitting inclusions. *Acta Metallurgica,* 21**,** 571-574.

MURA, T. 1982. *Micromechanics of defects in solids*.

NORRIS, A. N. 1985. A differential scheme for the effective moduli of composites. *Mechanics of Materials,* 4**,** 1-16.

PICHLER, C. & LACKNER, R. 2009. Upscaling of viscoelastic properties of highly-filled composites: Investigation of matrix–inclusion-type morphologies with power-law viscoelastic material response. *Composites Science and Technology,* 69**,** 2410-2420.

PICHLER, C., LACKNER, R. & AIGNER, E. 2012. Generalized self-consistent scheme for upscaling of viscoelastic properties of highly-filled matrix-inclusion composites – Application in the context of multiscale modeling of bituminous mixtures. *Composites Part B: Engineering,* 43**,** 457-464.

RIGDEN, P. J. 1947. The use of fillers in bituminous road surfacings. A study of filler-binder systems in relation to filler characteristics. *Journal of the Society of Chemical Industry,* 66**,** 299-309.

SHASHIDHAR, N. & SHENOY, A. 2002. On using micromechanical models to describe dynamic mechanical behavior of asphalt mastics. *Mechanics of Materials,* 34**,** 657-669.

SHU, X. & HUANG, B. 2008. Dynamic Modulus Prediction of HMA Mixtures Based on the Viscoelastic Micromechanical Model. *Journal of Materials in Civil Engineering,* 20**,** 530-538.

TANDON, G. P. & WENG, G. J. 1984. The effect of aspect ratio of inclusions on the elastic properties of unidirectionally aligned composites. *Polymer Composites,* 5**,** 327-333.

UNDERWOOD, B. S. 2011. *Multiscale constitutive modeling of asphalt concrete*.

UNDERWOOD, B. S. & KIM, Y. R. 2013. Effect of volumetric factors on the mechanical behavior of asphalt fine aggregate matrix and the relationship to asphalt mixture properties. *Construction and Building Materials,* 49**,** 672-681.

UNDERWOOD, B. S. & KIM, Y. R. 2014. A four phase micro-mechanical model for asphalt mastic modulus. *Mechanics of Materials,* 75**,** 13-33.

WALPOLE, L. J. 1969. On the overall elastic moduli of composite materials. *Journal of the Mechanics and Physics of Solids,* 17**,** 235-251.

WU, T. T. 1966. The effect of inclusion shape on the elastic moduli of a two-phase material. *International Journal of Solids and Structures,* 2**,** 1-8.

YIN, H. & ZHAO, Y. 2016. *Introduction to the Micromechanics of Composite Materials*, CRC Press.

YIN, H. M., BUTTLAR, W. G., PAULINO, G. H. & DI BENEDETTO, H. 2008. Assessment of Existing Micro-mechanical Models for Asphalt Mastics Considering Viscoelastic Effects. *Road Materials and Pavement Design,* 9**,** 31-57.

ZHANG, H., ANUPAM, K., SCARPAS, A. & KASBERGEN, C. 2018. Comparison of Different Micromechanical Models for Predicting the Effective Properties of Open Graded Mixes. *Transportation Research Record,* 2672**,** 404-415.

5

Discrete particles-based micromechanical models

5.1 Introduction

The previous chapter showed that CBMM failed to produce accurate predictions, especially for densely compacted PA mixes or at lower test frequencies. The inaccuracy of the predictions is attributed to the fact that CBMM cannot explicitly account for the volume-filling stiffening effect and stiffening effect of the particle-to-particle direct contacts. In order to address these limitations, researchers (Li et al., 1999, Shashidhar and Shenoy, 2002) have tried to make modifications on the basis of the currently used CBMM.

For example, Li et al. (Li et al., 1999) have developed a modified version of the GSC model (termed as "Li's model") to take the effect of the aggregates' size into account. Unlike the GSC model, where the ratio of the inclusion's radius to that of the matrix is only related to the volume fraction of the inclusion particles, in Li's model, this ratio is also dependent on the size and the gradation of the particles. Using Li's model, researchers (Shu and Huang, 2008) observed that the predicted modulus increased by around 20% when the maximum aggregate size increased from 4.75 mm to 19 mm. However, this limited increase of modulus was not enough to account for the significant difference between the predictions and the experimental results at lower frequencies.
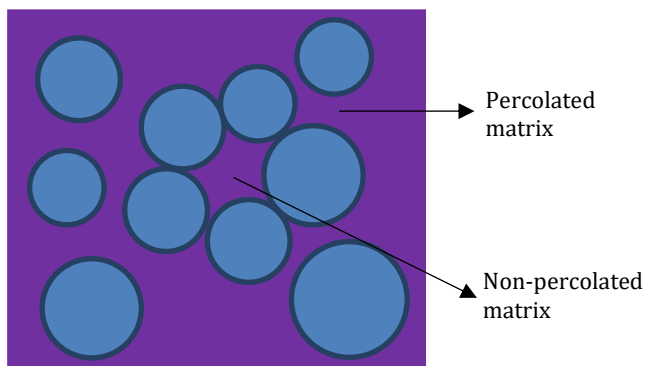
Figure 5.1 Illustration of the percolated and non-percolated matrix

Furthermore, in order to consider the stiffening effect of the particle-to-particle direct contacts, researchers (Shashidhar and Shenoy, 2002) introduced the percolation theory into the GSC model. Percolation theory considers the non-percolated matrix within the clusters of connected particles, see Figure 5.1. Using this theory, a modified GSC model (termed as "the percolation-introduced GSC model") where the non-percolated matrix was assumed as part of the inclusion phase was constructed. It was observed that the percolation-introduced GSC model could provide more accurate predictions than the GSC model. However, the accuracy could only improve up to a

concentration of around 40%, beyond which it significantly decreased (Underwood and Kim, 2014).

Further failure of modified CBMM indicates that all the CBMM have an intrinsic drawback, and because of that, it is impossible for these models, even if they are modified, to explicitly account for the volume-filling stiffening effect and the stiffening effect of the particle-to-particle direct contacts. In fact, researchers (Marcadon et al., 2007) have pointed out that one of the main reasons for the failure of CBMM is that in such models, the set of all the individual particles is simply represented as one inclusion phase. In this case, it is impossible to consider any characteristics of individual particles, not to mention their interactions and direct contacts.
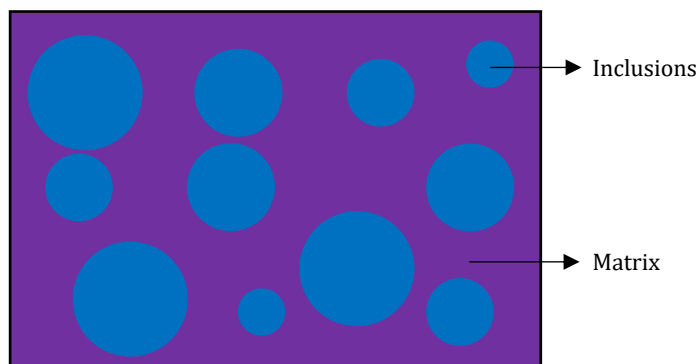
Figure 5.2 Illustration of the physical interaction model

In light of the above discussions, it can be deduced that in order to improve the accuracy of the predictions, one potential solution is to use models that are capable of taking into account the characteristics of individual particles. Micromechanical models where specific characteristics of individual particles in an asphalt composite can be defined have been developed by researchers. For example, in the physical interaction model (Underwood, 2011), different sizes of individual particles are embedded into a continuous matrix, see Figure 5.2. On the basis of the distribution of the particles and their different sizes, the stiffness of the composite can be estimated by quantifying the stiffening effects of individual particles and their interactions.

Although the physical interaction model provides a way to consider the characteristics of individual particles, it is only suitable for composites without or with few air voids, such as mastic and dense asphalt mixtures. This is because the matrix in the model is considered to be continuous. However, in PA mixes, since there is a high content of air voids, the matrix phase is expected to be discontinuously located between adjacent particles. Therefore, in order to reasonably describe the microstructure of PA mixes, a different micromechanical model is required.

Apart from the physical interaction model, DBMM can also take into account the characteristics of individual particles (Dvorkin et al., 1994, Zhu and Nodes, 2000, Chang and Liao, 1994). In DBMM, a bonded granular material, such as concrete, asphalt mixture, etc., is described as an assembly of packing individual particles that are bonded by elastic/viscoelastic binders (Dvorkin et al., 1994, Zhu et al., 1996, Chang et al., 1999), see Figure 5.3. Based upon such geometric configuration, different researchers have derived equations for calculating the mechanical properties of bonded granular materials. In this study, the equations derived by Dvorkin et al (Dvorkin et al., 1994) were adopted, and thus, DBMM for bonded granular materials is referred to as Dvorkin's model in the following sections.
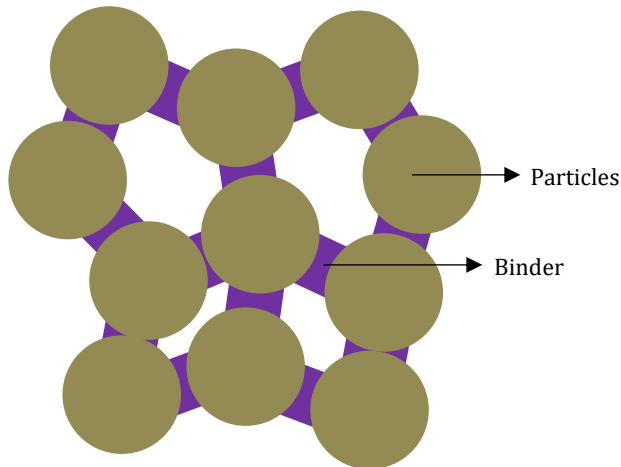
Figure 5.3 Illustration of DBMM for bonded granular materials

Comparing the illustrated geometries in Figure 5.2 and Figure 5.3, it can be clearly seen that the arrangement described by Dvorkin's model is naturally a more reasonable and realistic microstructure for PA type mixes. Moreover, Dvorkin's model includes several geometric parameters to describe the characteristics of individual particles, such as the radius of the particles, the average number of contacts per particle, the radius and the thickness of the binders (which determines the distance between adjacent particles). With these various geometric parameters, it is expected that the inter-particle interactions can be characterized by Dvorkin's model in a more explicit way.

The application of Dvorkin's model on granular materials such as glass beads packs, frozen sand, etc. has been investigated (Chang and Liao, 1994, Dvorkin et al., 1994, Chang and Gao, 1997, Zhu and Nodes, 2000); however, limited research work has been conducted to use this model for asphalt materials. Relevant studies can be found in the work of Cheung et al. (Cheung et al., 1999), Zhu and Nodes (Zhu and Nodes, 2000), etc., where Dvorkin's model was used to simulate the creep characteristics of asphalt

mixtures. However, these studies did not provide a rigorous way to implement the model for asphalt materials, especially in terms of the determination of the geometric parameters. Therefore, more efforts are required to investigate the implementation and the evaluation of Dvorkin's model for asphalt materials.

Based upon the above discussions, the main aim of this chapter is to investigate the implementation and the performance of Dvorkin's model in predicting the modulus of PA mixes. To achieve this, a framework that describes how to use Dvorkin's model for predicting the stiffness of PA mixes is firstly proposed. On the basis of that, the performance of Dvorkin's model is evaluated and in the end, both the advantages and the limitations of the model are highlighted.

5.2 Introduction of Dvorkin's model

In DBMM, the overall effective moduli of a granular material are derived by homogenizing the stiffness of an assembly of two-particle systems that orient in different directions. This section firstly describes the contact law of a two-bonded particle system (i.e. the relationship between the applied force and the corresponding displacement), on the basis of which, a homogenization technique is introduced to obtain the effective (homogenized) moduli of a bonded granular material.

5.2.1 Contact law of a two-bonded particles system

A two-bonded particle system consisting of two equal-sized spheres and the binder material (which was considered as mortar in this study) between the particles is illustrated in Figure 5.4a. The spherical particles are assumed to have an arbitrary radius R, with the mortar's radius of a and a minimum height of $2h_0$. It is noted here that generally, particles in a granular material have different sizes and irregular shapes. Since it is a big challenge to derive closed-form solutions for the contact law of adjacent particles with irregular shapes and different sizes, most studies have simplified all the particles as identical spheres (Dvorkin et al., 1994, Chang and Liao, 1994).

The stiffness of a two-bonded particles system, denoted as S, can be generally defined as:

$$F_n = S_n \delta_n, F_\tau = S_\tau \delta_\tau \tag{5.1}$$

where F is the applied force on the system; δ is the displacement of the centre of one particle relative to the median plane (the x-axis); and the subscripts n and τ denote the normal and the tangential direction, respectively.

a. Two bonded particles   **b. Stress distribution at the interface**
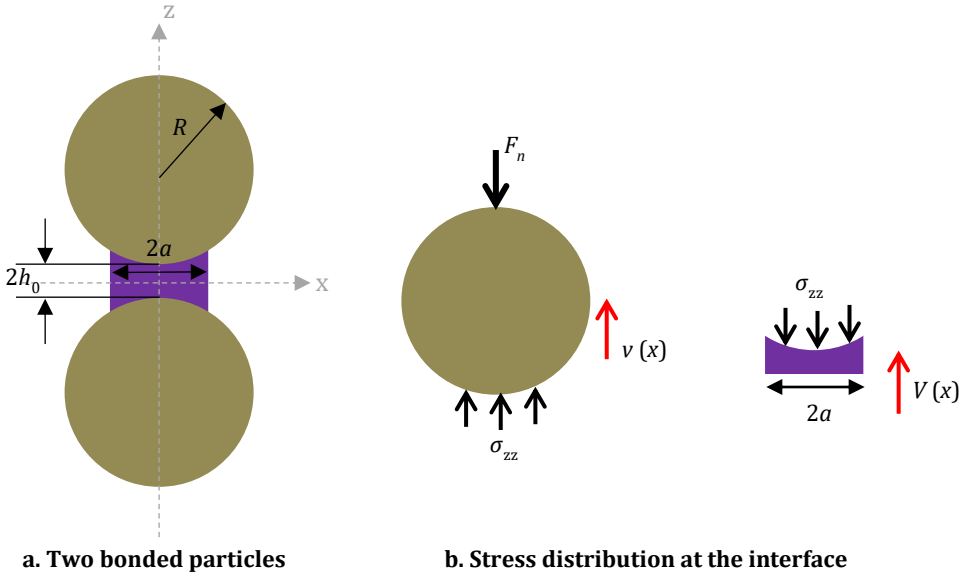
Figure 5.4 A two-bonded particle system

The value of δ is related to the displacement of the mortar's surface (represented as V and U in the normal direction and the tangential direction, respectively) as well as the displacement of the sphere's surface (represented as v and u in the normal direction and the tangential direction, respectively), see Equations (5.2) and (5.3).

$$\delta_n = v(x) - V(x) \tag{5.2}$$

$$\delta_\tau = u(x) - U(x) \tag{5.3}$$

In order to calculate the displacement of the mortar, researchers (Dvorkin et al., 1994) proposed a solution for a similar problem assuming the thin mortar as an elastic base. In this solution, $V(x)$ and $U(x)$ were related to the stress along the interface σ via Equations (5.4) and (5.5), respectively. Furthermore, for a case where a is much smaller than R, $v(x)$ and $u(x)$ can be approximated by the surface's displacement of an elastic half-space, see Equations (5.6) and (5.7), respectively.

$$\sigma_n(x) = -\frac{2G_{\text{mor}}(1 - \nu_{\text{mor}})}{1 - 2\nu_{\text{mor}}} \frac{V(x)}{h(x)} \tag{5.4}$$

$$\sigma_\tau(x) = -G_{\text{mor}} \frac{U(x)}{h(x)} \tag{5.5}$$

$$v(x) = \frac{1 - \nu_a}{\pi G_a} \int_0^\pi d\varphi \int_0^\beta \sigma_n(r) ds \tag{5.6}$$

$$u(x) = \frac{1}{2\pi G_a} \int_0^\pi d\varphi \int_0^\beta \sigma_\tau(r)(1 - v_a \sin^2 \varphi) ds \qquad (5.7)$$

where

$$\beta = x\cos\varphi + \sqrt{a^2 - x^2 \sin^2 \varphi}$$

$$r = \sqrt{x^2 + s^2 - 2xs\cos\varphi}$$

v_{mor} and G_{mor} are the Poisson's ratio and the shear modulus of the mortar, respectively; v_a and G_a are the Poisson's ratio and the shear modulus of the particles, respectively; $h(x)$ is the half-thickness of the mortar, which can be approximated as

$$h(x) = h_0 + \frac{x^2}{2R} \qquad (5.8)$$

By combining Equations (5.2), (5.4) and (5.6), or Equations (5.3), (5.5) and (5.7), the displacement of the mortar's surface can be obtained by giving a non-zero constant value of δ, see Equations (5.9) and (5.10). These two equations are known as the Volterra integral equations of the second kind. Since this type of integral equation is too complicated to be solved analytically, a numerical technique was used, see Appendix A.

$$\delta_n + V(x) = \Lambda_n \int_0^\pi d\varphi \int_0^\beta \frac{V(r)}{h(r)} ds \qquad (5.9)$$

$$\delta_\tau + U(x) = \Lambda_\tau \int_0^\pi d\varphi \int_0^\beta \frac{U(r)}{h(r)}(1 - v_a \sin^2 \varphi) ds \qquad (5.10)$$

where

$$\Lambda_n = -\frac{2G_{mor}}{\pi G_a} \frac{(1 - v_a)(1 - v_{mor})}{1 - 2v_{mor}}$$

$$\Lambda_\tau = -\frac{G_{mor}}{2\pi G_a}$$

Once the displacement of the mortar's surface is known, the value of σ can be calculated using Equations (5.4) and (5.5). The value of F is determined by integrating σ on the whole area of the interface, see Equations (5.11) and (5.12). Dividing the value of F by the given constant value of δ, the values of S_n and S_τ are finally obtained.

$$F_n = \int_0^a \sigma_n(x) \cdot 2\pi x \cdot dx \qquad (5.11)$$

$$F_\tau = \int_0^a \sigma_\tau(x) \cdot 2\pi x \cdot dx \qquad (5.12)$$

It is noted that the above solutions were developed for particles bonded by elastic binders. The utilization of these solutions for asphalt mixtures can be achieved according to the elastic-viscoelastic corresponding principle, which is the same as the method used for CBMM (see Chapter 4 Section 4.2.4).

5.2.2 Homogenization technique

In order to upscale the mechanical properties of a two-bonded particle system to the effective moduli of a granular material, a homogenization technique is needed. As the first step, an assembly of bonded particles, as illustrated in Figure 5.5, is considered as a representative volume element (RVE) of a bonded granular material.
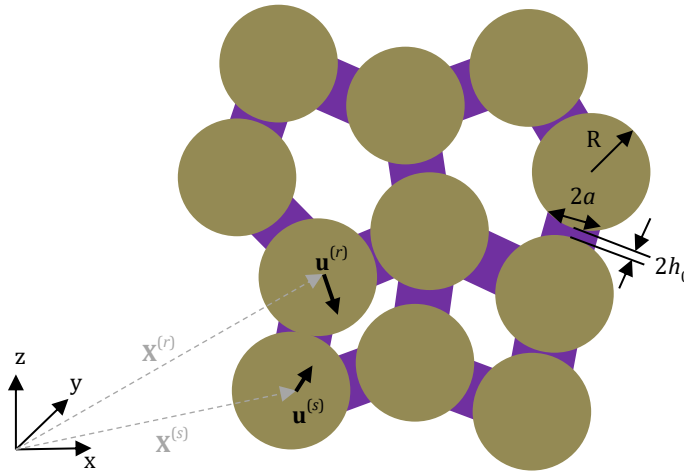
Figure 5.5 A pack of bonded spherical particles with uniform sizes

Two adjacent spheres r and s have the position vectors of $\mathbf{X}^{(r)}$ and $\mathbf{X}^{(s)}$ in the global coordinate system, respectively. Under a deformation $\mathbf{u}$ subjected to the boundary of the system, the centres of r and s also undergo displacements, represented as $\mathbf{u}^{(r)}$ and $\mathbf{u}^{(s)}$, respectively. By using the kinematic hypothesis that the strains throughout the pack are uniform, the values of $\mathbf{u}^{(r)}$ and $\mathbf{u}^{(s)}$ can be calculated via Equation (5.13).

$$u_i^{(r)} = \left\langle \varepsilon_{ij} \right\rangle : X_j^{(r)}, u_i^{(s)} = \left\langle \varepsilon_{ij} \right\rangle : X_j^{(s)} \tag{5.13}$$

where $\langle \varepsilon_{ij} \rangle$ is the average strain applied to the pack.

By symmetry, it can be obtained that the centre of the median plane between the sth and the rth particles undergoes a displacement of $(\mathbf{u}^{(r)}+\mathbf{u}^{(s)})/2$. Thus, relative to the median plane's centre point, the displacement of the rth sphere centre is $(\mathbf{u}^{(r)}-\mathbf{u}^{(s)})/2$. This relative displacement can be separated into a normal component $\boldsymbol{\delta}_n$ (Equation (5.14)) and a shear component $\boldsymbol{\delta}_\tau$ (Equation (5.15)). The total force $\mathbf{F}$ on the sth sphere

due to its connection with the rth sphere is given as the sum of the force in the normal direction and that in the tangential direction, see Equation (5.16). By substituting Equation (5.13) into Equation (5.16), the value of **F** can be further given as Equation (5.17).

$$\boldsymbol{\delta}_n = \delta_n \mathbf{I}^{(sr)} = \left[\frac{1}{2} \left(\mathbf{u}^{(r)} - \mathbf{u}^{(s)} \right) \cdot \mathbf{I}^{(sr)} \right] \mathbf{I}^{(sr)} \tag{5.14}$$

$$\boldsymbol{\delta}_\tau = \frac{1}{2} \left(\mathbf{u}^{(r)} - \mathbf{u}^{(s)} \right) - \boldsymbol{\delta}_n \tag{5.15}$$

$$\mathbf{F}^{(sr)} = \left(S_n - S_\tau \right) \left[\frac{1}{2} \left(\mathbf{u}^{(r)} - \mathbf{u}^{(s)} \right) \cdot \mathbf{I}^{(sr)} \right] \mathbf{I}^{(sr)} + S_\tau \left[\frac{1}{2} \left(\mathbf{u}^{(r)} - \mathbf{u}^{(s)} \right) \right] \tag{5.16}$$

$$F_i^{(sr)} = \left(S_n - S_\tau \right) \left(-\left(R + h_0 \right) \langle \varepsilon \rangle_{kl} I_k^{(sr)} I_l^{(sr)} \right) I_i^{(sr)} + S_\tau \left(-\left(R + h_0 \right) \langle \varepsilon \rangle_{ij} I_j^{(sr)} \right) \tag{5.17}$$

where **I** is the unit vector along the line of centres of two particles:

$$\mathbf{I}^{(sr)} = \frac{\mathbf{X}^{(s)} - \mathbf{X}^{(r)}}{2 \left(R + h_0 \right)} \tag{5.18}$$

The average stress filed <**σ**> of the granular material with a total volume V is related to the stresses within individual particles by using the following equation:

$$\langle \sigma \rangle_{ij} = \frac{1}{V} \sum_{N_a} \int_{V_s} \sigma_{ij}^{(s)} dV \tag{5.19}$$

where $\sigma_{ij}^{(s)}$ is the stress within the sth particle; V_s represents the volume of the sphere; N_a is the number of all the aggregate particles within V.

By using the divergence theorem, the value of $\sigma_{ij}^{(s)}$ can be calculated from the traction on the surface of the particle:

$$\int_{V_s} \sigma_{ij}^{(s)} dV = \frac{1}{2} \int_{S_s} \left(x_i' \tau_j^{(s)} + x_j' \tau_i^{(s)} \right) dS \tag{5.20}$$

where S_s is the surface of the sth particle; **x'** denotes the position vector of a point on S_s relative to the center of the particle; **τ**$^{(s)}$ denotes the traction across S_s. From Figure 5.5, it can be seen that the value of **τ**$^{(s)}$ is non-zero only at the position where the particle connects with other particles. Therefore, Equation (5.20) can be further written as

$$\int_{V_s} \sigma_{ij}^{(s)} dV = \frac{1}{2} \sum_n \left(x_i' F_j^{(sr)} + x_j' F_i^{(sr)} \right) \tag{5.21}$$

where n is the average number of the particles that connect to one particle.

When the connection area between the sth and the rth particle is small, the value of **x'** can be approximated by the position vector of the centre of the connection area relative to the centre of the sth particle:

$$\int_{V_s} \sigma_{ij}^{(s)} dV = \frac{1}{2} \sum_n \left[\frac{1}{2} \left(X_i^{(r)} - X_i^{(s)} \right) F_j^{(sr)} + \frac{1}{2} \left(X_j^{(r)} - X_j^{(s)} \right) F_i^{(sr)} \right] \tag{5.22}$$

By substituting Equation (5.22) into Equation (5.19), the value of **<σ>** can be written as

$$\langle \sigma \rangle_{ij} = \frac{1}{2V} \sum_{N_a} \sum_n \left[\frac{1}{2} \left(X_i^{(r)} - X_i^{(s)} \right) F_j^{(sr)} + \frac{1}{2} \left(X_j^{(r)} - X_j^{(s)} \right) F_i^{(sr)} \right] \tag{5.23}$$

This value can be further expressed as Equation (5.24) by substituting Equation (5.17) and Equation (5.18) into Equation (5.23).

$$\langle \sigma \rangle_{ij} = \frac{(R+h_0)^2}{2V} \sum_{N_a} \sum_n \left[\begin{array}{l} 2\left(S_n - S_\tau\right)\left(\langle \varepsilon \rangle_{kl} I_k^{(sr)} I_l^{(sr)}\right) I_i^{(sr)} I_j^{(sr)} \\ + S_\tau \left(\langle \varepsilon \rangle_{jk} I_k^{(sr)} I_i^{(sr)} + \langle \varepsilon \rangle_{ik} I_k^{(sr)} I_j^{(sr)} \right) \end{array} \right] \tag{5.24}$$

Assuming that the geometry of the pack is statistically isotropic and the distribution probability of the contact points over the surface of a sphere is uniform, the summation in Equation (5.24) can be represented in terms of averages:

$$\langle \sigma \rangle_{ij} = \frac{(R+h_0)^2 n N_a}{2V} \left[2\langle (S_n - S_\tau) \langle \varepsilon \rangle_{kl} I_k I_l I_i I_j \rangle + \langle S_\tau \langle \varepsilon \rangle_{jk} I_k I_i \rangle + \langle S_\tau \langle \varepsilon \rangle_{ik} I_k I_j \rangle \right] \tag{5.25}$$

where the brackets <·> denote the average over all uniformly distributed unit vector **I**.

In Equation (5.25), the total volume of the system V can be given as

$$V = \frac{V_a}{\phi_a} \tag{5.26}$$

where V_a and ϕ_a denote the volume and the volume fraction of the aggregate particles in the RVE, respectively. When all the particles are spheres with uniform sizes, the value of V_a is given as

$$V_a = \frac{4}{3} \pi R^3 N_a \tag{5.27}$$

Combining Equations (5.26)-(5.27), the value of N_a/V can be expressed as

$$\frac{N_a}{V} = \frac{3}{4} \frac{\phi_a}{\pi R^3} \tag{5.28}$$

Therefore, Equation (5.25) can be further written as

$$\langle \sigma \rangle_{ij} = \frac{3n\phi_{\rm a}(R+h_0)^2}{8\pi R^3}\left[2\left\langle (S_n - S_\tau)\langle \varepsilon \rangle_{kl}\, I_k I_l I_i I_j \right\rangle + \left\langle S_\tau \langle \varepsilon \rangle_{jk}\, I_k I_i \right\rangle + \left\langle S_\tau \langle \varepsilon \rangle_{ik}\, I_k I_j \right\rangle \right] \quad (5.29)$$

According to the definition of the stiffness tensor:

$$\langle \sigma \rangle_{ij} = C_{ijkl} : \langle \varepsilon \rangle_{kl} \tag{5.30}$$

the general expression for the effective stiffness tensor of a granular material can be written as:

$$(C_{\rm eff})_{ijkl} = \frac{3n\phi_{\rm a}(R+h_0)^2}{16\pi R^3}\left[\begin{array}{c} 4\left\langle (S_n - S_\tau) I_i I_j I_k I_l \right\rangle + \left\langle S_\tau I_k I_i \right\rangle \delta_{jl} + \\ \left\langle S_\tau I_k I_j \right\rangle \delta_{il} + \left\langle S_\tau I_l I_i \right\rangle \delta_{jk} + \left\langle S_\tau I_l I_j \right\rangle \delta_{ik} \end{array} \right] \tag{5.31}$$

In Equation (5.31), the stiffness tensor of a granular material on the macroscale is related to the properties of a two-particle system on the microscale. Therefore, once the properties of a two-particle system are known, the effective moduli of the granular material can be obtained.

5.2.3 Effective moduli of a bonded granular material

Since it is generally considered a bonded granular material as an isotropic material, the expression for the effective stiffness tensor $\mathbf{C}_{\rm eff}$ in Equation (5.31) can be rewritten as:

$$(C_{\rm eff})_{ijkl} = \frac{3n\phi_{\rm a}(R+h_0)^2}{16\pi R^3}\left[\begin{array}{c} 4(S_n - S_\tau)\left\langle I_i I_j I_k I_l \right\rangle + \\ S_\tau \left(\left\langle I_k I_i \right\rangle \delta_{jl} + \left\langle I_k I_j \right\rangle \delta_{il} + \left\langle I_l I_i \right\rangle \delta_{jk} + \left\langle I_l I_j \right\rangle \delta_{ik} \right) \end{array} \right] \tag{5.32}$$

where S_n and S_τ are taken out from the average brackets over different directions.

According to the relationships in Equation (5.33) and the definition of the stiffness tensor for an isotropic material in Equation (5.34), the bulk modulus K and the shear modulus G of a bonded granular material can be calculated using Equation (5.35).

$$\left\langle I_i I_j \right\rangle = \frac{1}{3}\delta_{ij}, \left\langle I_i I_j I_k I_l \right\rangle = \frac{1}{15}\left(\delta_{ij}\delta_{kl} + \delta_{ik}\delta_{jl} + \delta_{ik}\delta_{jk} \right) \tag{5.33}$$

$$(C_{\rm eff})_{ijkl} = \left(K_{\rm eff} - \frac{2}{3}G_{\rm eff} \right)\delta_{ij}\delta_{kl} + G_{\rm eff}\left(\delta_{ik}\delta_{jl} + \delta_{il}\delta_{jk} \right) \tag{5.34}$$

$$K_{\rm eff} = \frac{n\phi_{\rm a}(R+h_0)^2}{12\pi R^3}S_n, G_{\rm eff} = \frac{n\phi_{\rm a}(R+h_0)^2}{20\pi R^3}\left(S_n + \frac{3}{2}S_\tau \right) \tag{5.35}$$

5.3 A proposed framework to predict the stiffness of PA mixes

The proposed framework for predicting the stiffness of PA mixes contained three main steps, see Figure 5.6. A microstructure for PA mixes was assumed to consist of randomly packing spherical particles, mortar, and air voids. The total volume of mortar was categorized into two functional groups. Some mortar that locates between adjacent particles plays a major role in binding particles together, and thus they were defined as the "binding mortar". Whereas the remaining parts only play a role in coating individual particles, and thus they were defined as the "coating mortar".
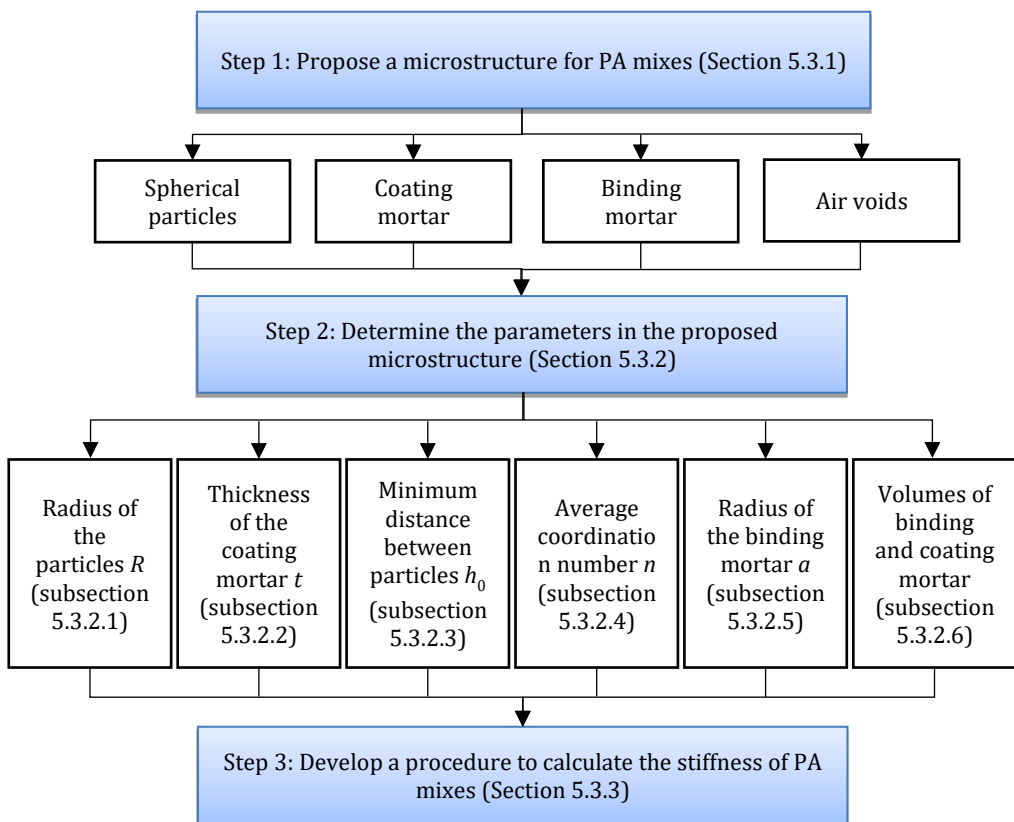
Figure 5.6 Flowchart of the proposed framework

To predict the stiffness of PA mixes, the mechanical, volumetric, and geometric properties of each phase are required. Generally, the mechanical and the volumetric properties can be directly measured from laboratory tests. Additionally, five geometric parameters need to be determined: 1) the radius of the spherical particles, 2) the thickness of the coating mortar, 3) the minimum thickness of the binding mortar, 4) the average coordination number, and 5) the radius of the binding mortar. These geometric

properties may also be measured using sophisticated technologies such as digital image processing. However, this method is difficult to be implemented since the values of all these geometric parameters vary with different locations. Thus, in this study, a different method that can be used to determine the geometric parameters of the proposed microstructure in a much easier but reasonable way was proposed.

In the proposed microstructure, the properties of both the binding mortar and the coating mortar affect the stiffness of a PA mix. However, Dvorkin's model can only predict the stiffness of a skeleton framework consisting of particles, air voids and the binding mortar. Therefore, in the last step, a procedure was developed to take into account the effect of the coating mortar.

5.3.1 Proposed microstructure model for PA mixes

A microstructure model for PA mixes, as illustrated in Figure 5.7, was proposed according to the literature (Chang and Meegoda, 1997). Individual particles (modelled as identical spheres with a uniform radius of R) are initially covered by mortar with a uniform thickness of t. When the mortar-covered aggregate particles pack together, the minimum distance between adjacent particles, represented as $2h_0$, has an initial value of $2t$, see Figure 5.7a. It was assumed that during the compaction process, the value of h_0 decreases, and depending on the amount of the compaction work, the value of h_0 ranges from t (without any compaction effort) to 0 (two particles contact each other), see Figure 5.7b.

a. **Before compaction**   b. **After compaction**
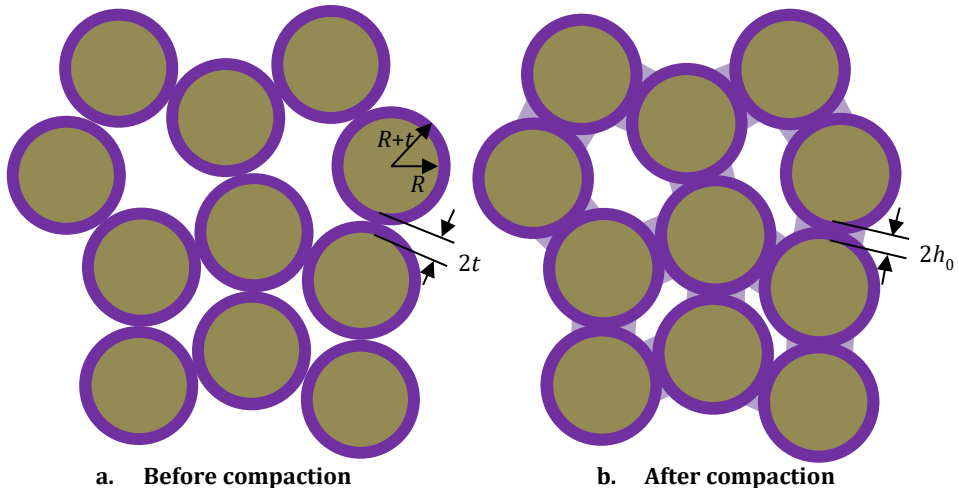
Figure 5.7 Proposed microstructure model for PA mixes

The volume of the binding mortar between two adjacent particles is illustrated in Figure 5.8a. The binding mortar, with a radius of a, was assumed to be composed of two

parts, see Figure 5.8b. When two particles are compacted closer, their coating mortar overlaps each other to form one part of the binding mortar with a radius of a_1. Due to the overlap of the coating mortar, some mortar is squeezed out and forms the other part of the binding mortar with a radius of a_2.

a. A pair of adjacent particles | b. Two components of the binding mortar
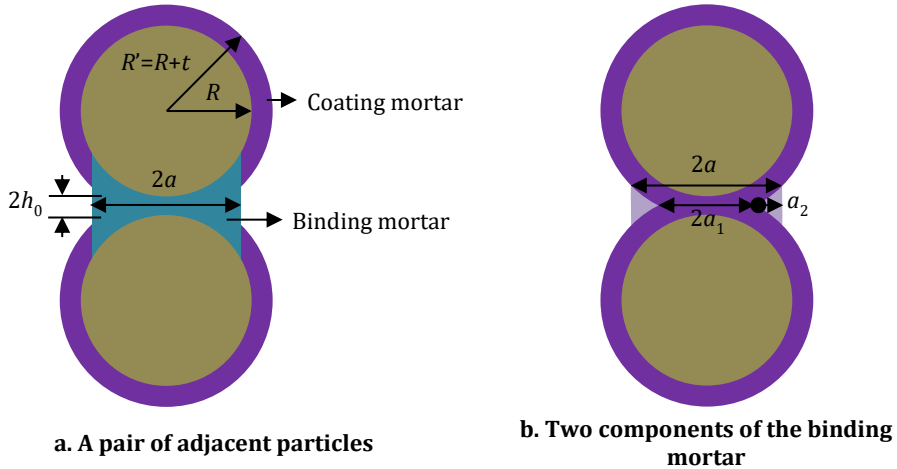
Figure 5.8 Illustration of binding mortar

5.3.2 Method to determine geometric parameters

In the proposed microstructure in Figure 5.7b, five geometric parameters, i.e. R, t, h_0, n and a, are required to predict the effective modulus of the mix. In this section, the proposed methods to determine these parameters are presented. Once the geometric parameters are known, the volume fractions of the binding mortar ϕ_{b_b} and the coating mortar ϕ_{b_c} can be further determined. The proposed method to determine ϕ_{b_b} and ϕ_{b_c} is introduced in this section as well.

5.3.2.1 *Calculation of R*

In Dvorkin's model, aggregate particles are modelled as identical spheres. However, in an asphalt mix, the size of the aggregate particles is generally not uniform but graded. Therefore, in order to specify the value of R, it is necessary to obtain a representative size of the aggregate particles in the mix. For this purpose, a commonly used mathematical method of averaging different sizes of graded aggregate particles was utilized (Li et al., 1999), see Equation (5.36):

$$R = \sum_{i=1}^{N-1} \phi_i \cdot \frac{d_i + d_{i+1}}{2} \tag{5.36}$$

with

$$\phi_i = \frac{(P_{i+1} - P_i)/\rho_i}{\sum\limits_{j=1}^{N-1}(P_{j+1} - P_j)/\rho_i} \tag{5.37}$$

where P_{i+1} and P_i are the percentages passing the sieve $i+1$ and sieve i by the total weight of aggregates, respectively; ρ_i is the density of aggregates retained on sieve i; ϕ_i is the volume fraction of aggregate particles retained on sieve i; N is the total grades of aggregates by sieving, i.e., 0.063mm, 2mm, 5.6mm, etc.; and d_{i+1} and d_i are the diameters of sieve $i+1$ and sieve i, respectively.

5.3.2.2 *Calculation of t*

The value of t can be determined according to the binder content β in the mix, which is defined as

$$\beta = \frac{V_{\mathrm{mor}}}{V_{\mathrm{mor}} + V_{\mathrm{a}}} = \frac{\phi_{\mathrm{mor}}}{\phi_{\mathrm{a}} + \phi_{\mathrm{mor}}} \tag{5.38}$$

where V_{mor} and ϕ_{mor} denote the total volume and the volume fraction of the mortar, respectively.

Assuming that individual particles are surrounded by mortar with identical thicknesses, the value of V_{mor} can be calculated using Equation (5.39).

$$V_{\mathrm{mor}} = N_{\mathrm{a}} \cdot \frac{4}{3}\pi R^3 \left[(1+\tau)^3 - 1 \right] \tag{5.39}$$

where $\tau = t/R$. By substituting Equations (5.27) and (5.39) into Equation (5.38), the value of β can be written as

$$\beta = 1 - \frac{1}{(1+\tau)^3} \tag{5.40}$$

Since the value of β is known from the values of ϕ_{mor} and ϕ_{a}, the value of t can be computed from Equation (5.40).

5.3.2.3 *Calculation of h_0*

As mentioned earlier, the value of h_0 is related to the compaction effort. Since the compaction effort can be reflected by the air voids content, the value of h_0 can be determined according to the air voids content of the mix.

Figure 5.9 shows the relationship between the air voids content of the mix $\phi_{\mathrm{v\_c}}$ and the number of compaction cycles N during the compaction process. The value of $\phi_{\mathrm{v\_c}}$ is calculated according to the height of the specimens H, Equations (5.41)-(5.43).
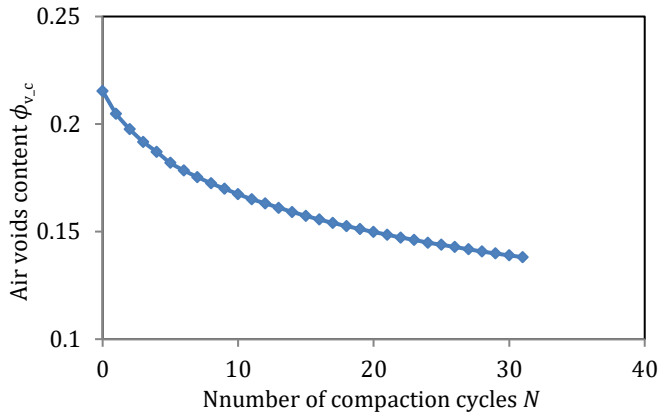
Figure 5.9 Relationship between air voids content and number of compaction cycles

$$\phi_{v\_c} = \frac{V_{\text{total}} - V_{\text{mass}}}{V_{\text{total}}} \tag{5.41}$$

$$V_{\text{total}} = \frac{1}{4}\pi \times 150^2 \times H \tag{5.42}$$

$$V_{\text{mass}} = \frac{W_{\text{mass}}}{\rho_{\text{max}}} \tag{5.43}$$

where V_{total} denotes the total volume of the specimen; V_{mass} and W_{mass} denote the volume and the weight of the real mass of the specimen; and ρ_{max} is the maximum density of the mix, which can be obtained from the density of each constituent.
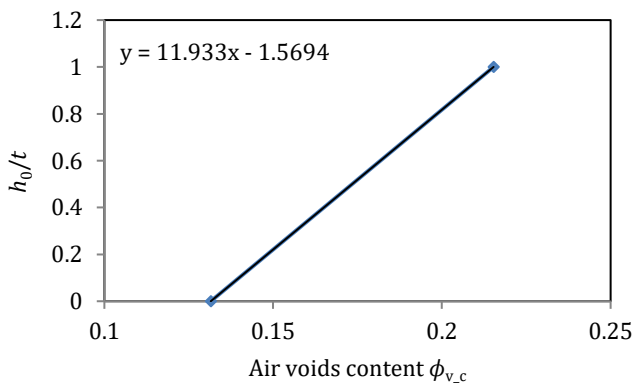
Figure 5.10 Relationship between h_0/t and air voids content

Before any compaction effort is applied (when N=0), the value of h_0 is expected to be equal to t, and the corresponding value of ϕ_{v_c} is approximately 0.22. With the

increase of the compaction effort, the value of h_0 decreases, and thus the value of ϕ_{v_c} decreases as well. After conducting a certain amount of compaction effort, h_0 is expected to be gradually close to 0, and meanwhile, ϕ_{v_c} gradually stabilizes at a value of 0.13.

Using the values of h_0 and ϕ_{v_c} in the above two extreme cases, the relationship between h_0/t and ϕ_{v_c} was assumed to be expressed as a simple linear function, see Figure 5.10. From this relationship, once the air voids content of the PA mix specimen is known, the value of h_0/t can be obtained.

5.3.2.4 *Calculation of n*

For a PA mix system in Figure 5.7b where spherical particles are covered by mortar, it is difficult to directly determine its average coordination number n. However, for a "dry" packing system consisting of only identical spheres, researchers (Chang et al., 1999) have proposed that the coordination number n_d can be estimated on the basis of the air voids content of the system ϕ_d, see Figure 5.11. The relationship between n_d and ϕ_d can be developed by plotting their values in different regular packings, i.e. a simple cubic packing (n_d=6, ϕ_d=0.4764), a tetragonal sphenoidal packing (n_d=8, ϕ_d=0.3954), a pyramidal packing (n_d=10, ϕ_d=0.3019) and a tetrahedral packing (n_d=12, ϕ_d=0.2595). As shown in Figure 5.11, the value of n_d shows an almost linear increase with the decrease of ϕ_d. Therefore, a regressed linear equation, see Equation (5.44), can be given to describe the relationship between n_d and ϕ_d.
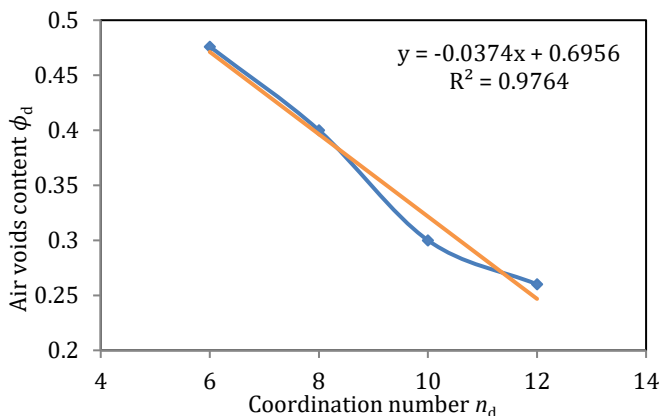
Figure 5.11 Relationship between the coordination number and the air voids content in a packing system of identical spheres

$$\phi_d = -0.0374n_d + 0.6956 \qquad (5.44)$$

On the basis of the relationship in Figure 5.11, researchers (Chang et al., 1999) further developed a method to determine the average coordination number of a packing system where binders for connecting adjacent particles (the binding mortar) were included. In this study, a similar method was used to determine the value of n.

In order to determine the value of n, a reference packing system is introduced, see Figure 5.12. In the reference system, individual particles have the same configurations as those in the PA mix in Figure 5.7b. This indicates that the coordination number in the reference system remains the same as n. However, particles in the reference system are covered by mortar with a thickness of h_0 instead of a thickness of t. Due to the change of the mortar's thickness, the air voids content in the reference system changes to a value of ϕ_0.

Since the minimum distance between adjacent particles in the PA mix system is $2h_0$, particles covered with mortar with a thickness of h_0 in the reference system are supposed to just touch each other. Therefore, the arrangement of the mortar-coated particles in the reference system can be considered the same as a dry packing system consisting of spheres with a uniform radius of $(R+h_0)$. Accordingly, the relationship between n and ϕ_0 can be described using the relationship in Equation (5.44).
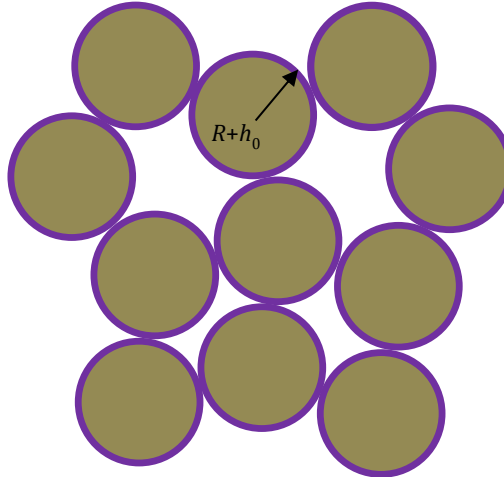
Figure 5.12 A reference packing system

Total volumes of the particles and the mortar V_a' in the reference system can be calculated using Equation (5.45), and thus the total volume of the reference system can be given as $V_a'/(1-\phi_0)$. It is further assumed that more mortar materials are located around the particles in Figure 5.12 to form the PA mix system in Figure 5.7b. Since the total volume of the system cannot change, the relationship in Equation (5.46) must satisfy.

$$V_a' = N_a \cdot \frac{4}{3}\pi\left(R+h_0\right)^3 \tag{5.45}$$

$$\frac{V_{mor}+V_a}{1-\phi_v}=\frac{V_a^{'}}{1-\phi_0} \tag{5.46}$$

where ϕ_v is the air voids content of the PA mix.

By substituting Equations (5.27), (5.39), and (5.45) into Equation (5.46), the value of ϕ_v can be expressed as

$$\phi_v=1-\frac{\left(1-\phi_0\right)\cdot\left(1+\tau\right)^3}{\left(1+\gamma\right)^3} \tag{5.47}$$

where $\gamma=h_0/R$. By combining Equations (5.44) and (5.47), the value of n can be determined for a given value of ϕ_v.

5.3.2.5 *Calculation of a*

It was mentioned in Figure 5.8 that the binding mortar is composed of two parts. One part (with a radius of a_1) is formed because two mortar-coated particles overlap each other, and the other part (with a radius of a_2) comes from the mortar that is squeezed out, see Figure 5.13a. On the basis of this assumption, a relationship that the volume of the cylinder V_1 (bounded by the red line in Figure 5.13b) is identical to that of the spherical cap V_2 (bounded by the green line) can be obtained:

$$H_1\times\pi a^2=\frac{\pi}{3}\times H_2^2\times\left[3\left(R+t\right)-H_2\right] \tag{5.48}$$

where H_1 and H_2 are the heights of the cylinder and the spherical cap, respectively, and their values can be computed using Equations (5.49) and (5.50), respectively.

$$H_1=\left(R+h_0\right)-\sqrt{\left(R+t\right)^2-a^2} \tag{5.49}$$

$$H_2=\left(R+t\right)-\sqrt{\left(R+t\right)^2-a^2} \tag{5.50}$$

By substituting Equations (5.49) and (5.50) into Equation (5.48), the following relationship can be obtained:

$$\begin{aligned}&\left[\sqrt{\left(1+\tau\right)^2-\alpha^2}-\left(1+\gamma\right)\right]\alpha^2\\&=\frac{1}{3}\left[\left(1+\tau\right)-\sqrt{\left(1+\tau\right)^2-\alpha^2}\right]^2\left[2\left(1+\tau\right)+\sqrt{\left(1+\tau\right)^2-\alpha^2}\right]\end{aligned} \tag{5.51}$$

where $\gamma=h_0/R$, and $\alpha=a/R$. With the calculated values of t and h_0 from the previous steps, the value of a can be determined from Equation (5.51).
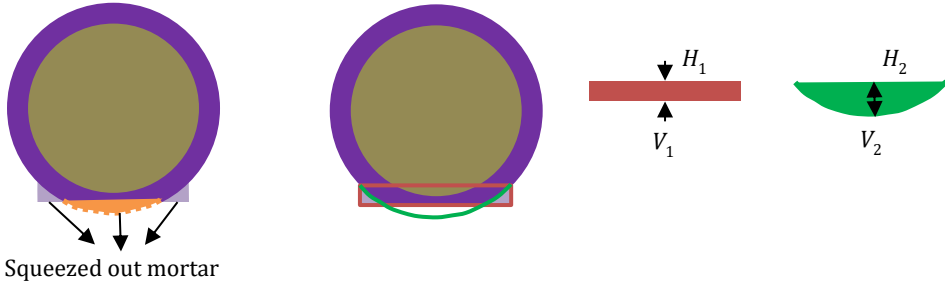
a. squeezed out mortar   **b. Relationship between V_1 and V_2**

Figure 5.13 Illustration for the calculation of a

5.3.2.6 *Calculation of ϕ_{b_b} and ϕ_{b_c}*

As illustrated in Figure 5.14, the volume of half of the binding mortar between two adjacent particles v_{m_b} can be calculated by subtracting the volume of a spherical cap from the volume of a cylinder, see Equation (5.52). The total volume of the binding mortar in a PA mix V_{m_b} is equal to the value of v_{m_b} multiplied by the average coordination number n and the total number of the particles N_a, see Equation (5.53). Once the value of V_{m_b} is known, the value of ϕ_{m_b} and ϕ_{m_c} can be easily obtained on the basis of the total volume and the volume fraction of the mortar, see Equations (5.54) and (5.55).
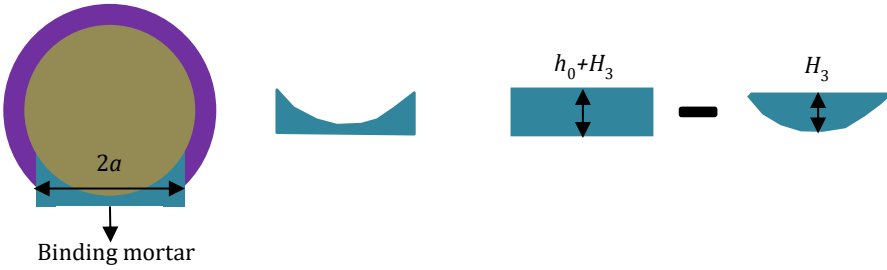
Figure 5.14 Illustration of the volume of the binding mortar

$$v_{m\_b} = \pi \times a^2 \times \left(h_0 + H_3 \right) - \frac{\pi}{3} \times H_3^{\,2} \times \left(3R - H_3 \right) \tag{5.52}$$

$$V_{m\_b} = N_a \cdot n \cdot v_{m\_b} \tag{5.53}$$

with

$$H_3 = R - \sqrt{R^2 - a^2}$$

$$\phi_{\mathrm{m\_b}} = \frac{V_{\mathrm{m\_b}}}{V_{\mathrm{mor}}} \cdot \phi_{\mathrm{mor}} \tag{5.54}$$

$$\phi_{\mathrm{m\_c}} = 1 - \phi_{\mathrm{m\_b}} \tag{5.55}$$

where V_{mor} can be obtained from Equation (5.39).

5.3.3 Method to calculate the stiffness of PA mixes

According to the literature (Dvorkin et al., 1999), contributions to the stiffness of a mix made by the binding mortar and the coating mortar are different. The binding mortar plays a major role in providing the stiffness of the mix because they enable the discrete particles to work together as a skeleton framework. By contrast, the coating mortar contributes to the stiffness of the mix by filling the air voids in the skeleton framework.

a. Skeleton framework equivalent as a two-phase composite

b. PA mix equivalent as a three-phase composite
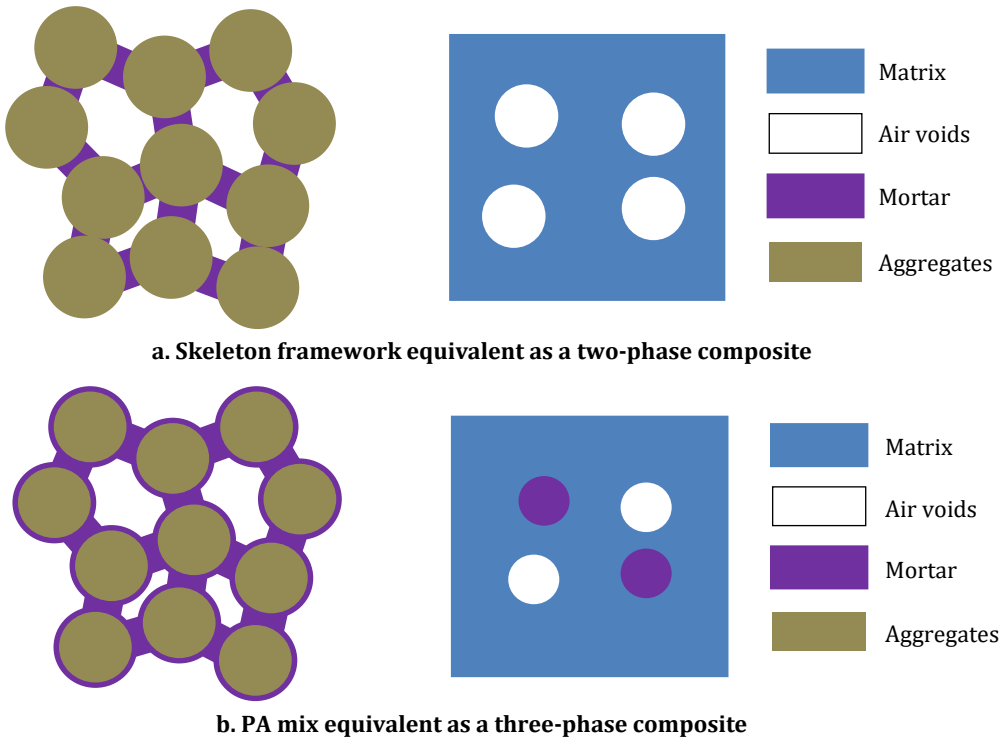
Figure 5.15 Procedures to calculate the stiffness of PA mixes

In light of the above realization, the following procedure was proposed to calculate the stiffness of PA mixes. At first, the stiffness of the skeleton framework consisting of aggregate particles and the binding mortar is predicted using Dvorkin's model, see Figure 5.15a. This skeleton framework is further assumed to be equivalent to a two-phase composite that consists of air voids embedded into a continuous matrix.

The stiffness of the two-phase composite is the same as the skeleton framework. The volume fraction of the air voids in the two-phase composite is equal to the sum of the volume fractions of the air voids and the coating mortar in the PA mix. Based on the stiffness of the composite and the volume fraction of each phase, the matrix's stiffness can be back-calculated.

At last, the covering mortar materials are added into the skeleton framework to form the PA mix. This is equivalent to the process that the same volume of mortar is embedded into the matrix of the two-phase composite. As a result, a three-phase composite consisting of the matrix, the coating mortar and air voids, is formed, see Figure 5.15b. The volume fractions of the coating mortar and the air voids in this three-phase composite are the same as those in the PA mix. Based on the stiffness and the volume fraction of each phase, the stiffness of the three-phase composite can be calculated. Therefore, the stiffness of the PA mix, which is equal to the stiffness of the three-phase composite, is obtained as well.

Since the matrix in the two-phase composite and the three-phase composite is continuous, the back-calculation of the matrix's stiffness and the calculation of the stiffness of the three-phase composite can be achieved using CBMM. In this study, the SC model was preferred over others due to the facts that: (a) it can provide more accurate predictions when the volume fraction of inclusions is lower than 50%, as demonstrated in Chapter 4 Section 4.3; and (b) it can be easily solved to back-calculate the stiffness of the matrix.

Implementing the above proposed framework for the materials of this study, the values of the geometric parameters in the PA mix microstructure model were quantified and the stiffnesses of PA mix-1 and PA mix-2 were estimated. In the following section, the obtained results are presented.

5.4 Results and discussions

5.4.1 Results of calculated geometric parameters

Using the proposed method in Section 5.3.2, the geometric parameters of the proposed microstructure of PA mixes were determined on the basis of the properties of each phase given in Chapter 2.

Since PA mix-1 and PA mix-2 contain the same aggregate gradations and the same asphalt binder contents, the values of R and t are identical for both mixes. The value of R was calculated as 4 mm using Equations (5.36) and (5.37). The value of β was calculated as 0.24 from the values of ϕ_b and ϕ_a using Equation (5.38). Once the value of β was known, the value of τ in Equation (5.40) was computed as 0.097, and thus the value of t was equal to 0.39 mm.

As can be seen in Figure 5.10, when the air voids contents are 18% and 13%, the values of h_0/t are approximately equal to 0.58 and 0, respectively. Therefore, the values of h_0 were estimated as 0.22 mm and 0 mm for PA mix-1 and PA mix-2, respectively. Using the values of ϕ_v, R, t and h_0, the values of ϕ_0 were calculated as 0.268 and 0.340 from Equation (5.47) for PA mix-1 and PA mix-2, respectively. The values of n were further calculated as 11.5 and 9.5 for PA mix-1 and PA mix-2, respectively. On the basis of the obtained values of R, t and h_0, the values of a were computed as 1.67 mm and 2.53 mm using Equation (5.51) for PA mix-1 and PA mix-2, respectively. Furthermore, using the values of ϕ_{mor}, R, t, h_0, n and a, the values of ϕ_{m_b} were computed from Equations (5.52)-(5.54) as 9.4% and 20.3% for PA mix-1 and PA mix-2, respectively. The values of ϕ_{m_c} were further obtained using Equation (5.55) as 10.6% and 0.7% for PA mix-1 and PA mix-2, respectively. The calculated results of all the parameters are summarized in Table 5.1.

Table 5.1 Values of volumetric and geometric parameters

Parameters	ϕ_{mor}	ϕ_a	ϕ_v	R	t	h_0	n	a	ϕ_{m_b}	ϕ_{m_c}
PA mix-1	20%	62%	18%	4 mm	0.39 mm	0.22 mm	11.5	1.67 mm	9.4%	10.6%
PA mix-2	21%	66%	13%	4 mm	0.39 mm	0 mm	9.5	2.53 mm	20.3%	0.7%

Comparing the values of the geometric parameters between PA mix-1 and PA mix-2, it can be found that different compaction effort affects individual phases in terms of not only their volumetric properties on the macroscale but also their geometric properties on the microscale. A larger amount of compaction effort decreases the average distance between adjacent particles (or the average thickness of the binding mortar). When two particles become closer, a higher proportion of the coating mortar overlaps each other to form the binding mortar. Therefore, with the decrease of the distance between adjacent particles, the radius, as well as the total volume of the binding mortar, increases. On the other hand, more compaction effort decreases the average coordination number. This can be explained by the fact that when the particles become closer, less space around one particle is provided for other particles to surround it.

5.4.2 Predicted results of PA mixes' modulus

Figure 5.16 shows the predicted results of $|E_{mix}^*|$ and δ_{mix} for both PA mix-1 and PA mix-2. It is noted that in the calculation of $|E_{mix}^*|$ and δ_{mix} for PA mix-2, instead of using 0, a value of h_0 that approaches 0 (i.e. 10^{-8} mm) was used. This is because when h_0 is equal to 0, the stresses of the mortar σ_n and σ_τ at the centre (see (5.4) and (5.5)) are equal to infinity, which is difficult to be dealt with during the integration of (5.6) and (5.7). On

top of that, using a value that is slightly different from 0 is not expected to significantly change the final results on the basis of the fact that the values of $|E_{mix}{}^*|$ and δ_{mix} converge when h_0 approaches 0.

In order to compare the performance of Dvorkin's model against CBMM, predicted results from CBMM are also presented in the same figures. The predictions from the Dilute model with the utilization of the DS approach were taken as examples because in Chapter 4 it was shown that these predictions were more accurate than others.

As can be seen in Figure 5.16, at higher frequencies, for a loosely compacted PA mix (i.e. PA mix-1), the predicted results of $|E_{mix}{}^*|$ and δ_{mix} do not show significant differences between CBMM and Dvorkin's models. Whereas, for a densely compacted PA mix (PA mix-2), Dvorkin's model provides better predictions. This can be related to the fact that Dvorkin's model is developed particularly for densely packing granular materials (Dvorkin et al., 1999). Apart from the volumetric properties of each phase, Dvorkin's model also takes into account the geometric characteristics of the individual particles and the mortar. Therefore, compared to CBMM, Dvorkin's model can account for the volume-filling stiffening effect more accurately.
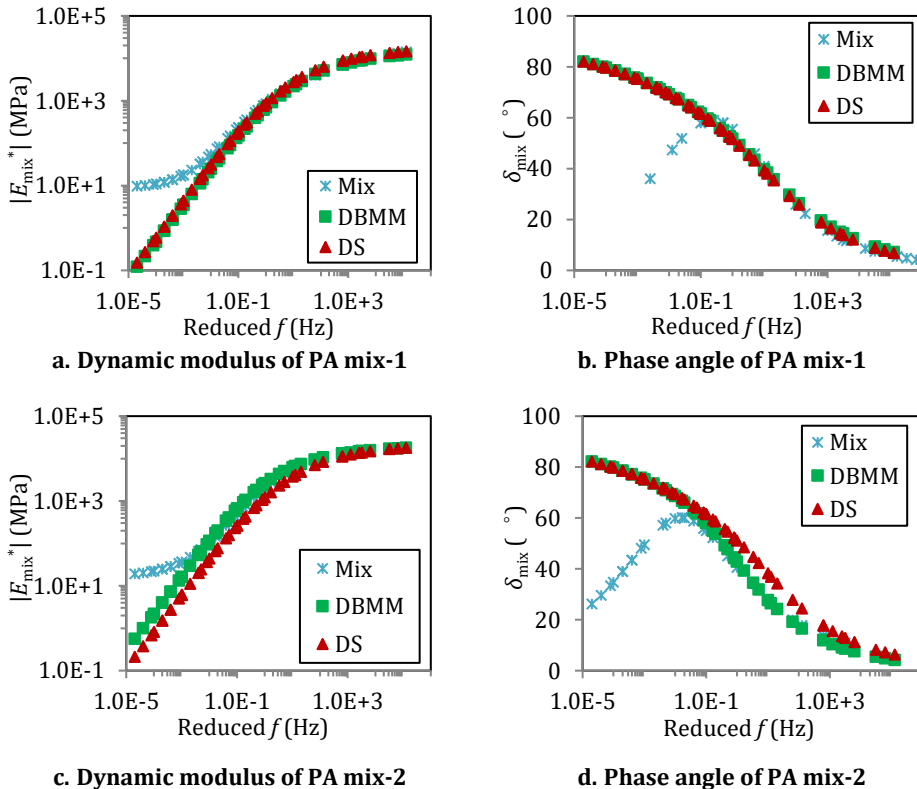

a. Dynamic modulus of PA mix-1

b. Phase angle of PA mix-1

c. Dynamic modulus of PA mix-2

d. Phase angle of PA mix-2

Figure 5.16 Predicted results of PA mixes' modulus using Dvorkin's model

Figure 5.16 also shows that Dvorkin's model has the same limitation as CBMM that at lower frequencies, predicted values of $|E_{mix}^*|$ are significantly lower than the experimental results. Moreover, the predicted results of δ_{mix} do not show a decreasing trend. One of the possible reasons could be that the values of some input parameters, i.e. h_0, n, a, and ν_{mor}, should change with frequencies/temperatures rather than being constants over the whole frequency range. With this realization, in order to further understand the limitation of Dvorkin's model, the sensitivity of the predicted modulus on these parameters was conducted. In the following section, the results of the sensitivity analysis are presented.

5.4.3 Sensitivity analysis of predicted results to input parameters

In the previous analysis, the geometric characteristics of the proposed PA mix's microstructure were considered to remain unchanged. However, this assumption may not be valid because the external loads, i.e. the gravity and the applied load, may change the values of geometric parameters (i.e. h_0, n and a). With the increase of temperatures and the decrease of frequencies, the mortar becomes softer and easier to deform. Consequently, the distance between adjacent particles, i.e. the value of h_0, is expected to decrease. Meanwhile, the change of h_0 also induces the change of n and a, which can be easily derived from Equations (5.44)-(5.47) and Equation (5.51).

The above discussion indicates that the use of constant values of h_0, n and a in the whole frequency range can be one reason for the poor performance of Dvorkin's model in Figure 5.16. Additionally, a constant value of ν_{mor} was assumed in the predictions. As mentioned earlier, the value of ν_{mor} is frequency- and temperature-dependent. Therefore, it is also possible that the inaccuracy of the predictions results from the assumption of a constant value of ν_{mor}. With these realizations, in this section, the values of h_0 and ν_{mor} are varied to check if the performance of the model can be improved. It is noted that sensitivity analysis was conducted by taking PA mix-1 as an example.

5.4.3.1 *Sensitivity of predicted E_{mix}^* on h_0*

As discussed above, the value of h_0 is expected to decrease with the decrease of frequencies, therefore, three lower values of h_0 (h_0<0.22 mm or h_0/t<0.58) were used to predict E_{mix}^* in the sensitivity analysis. Table 5.2 shows the calculated results of n, a, ϕ_{m_b} and ϕ_{m_c} for different values of h_0 using Equations (5.44)-(5.47) and Equation (5.51), respectively. It can be seen that with the decrease of h_0, the values of n and ϕ_{m_c} decrease while the values of a and ϕ_{m_b} increase. The reasons for the changes of n, a, ϕ_{m_b} and ϕ_{m_c} with the value of h_0 have been explained in the previous section (see Section 5.4.1).

Figure 5.17 presents the predicted $|E_{mix}^*|$-f and δ_{mix}-f curves using different values of h_0, n and a. It can be observed that with the decrease of h_0, PA mixes become stiffer,

which is reflected by an increase of predicted $|E_{mix}{}^*|$ and a decrease of predicted δ_{mix}. This can be explained by the fact that with the decrease of the distance between two particles, the total volume of the binding mortar, which makes the main contribution to the load-bearing capacity of the mix, increases. Meanwhile, when two particles become closer, their interactions become stronger. As can be derived from Equations (5.4) and (5.5), the stresses at the mortar-particle interface increase with the decrease of h_0. When the interactions between adjacent particles become stronger, their stiffening effect on the mix becomes more significant.

Further investigations of the plots in Figure 5.17 show that the shapes of the predicted $|E_{mix}{}^*|$-f and δ_{mix}-f curves do not significantly change with different values of h_0. At very low frequencies, even when h_0 is close to 0, the predicted values of $|E_{mix}{}^*|$ are still much lower than the experimental results. Moreover, the predicted values of δ_{mix} do not show a significant decrease. These observations indicate that the predictions are not likely to be accurate even if the values of the geometric parameters change. Therefore, it can be concluded that the possible inaccurate assumption about the geometric parameters is not the main reason to explain the poor performance of the model at high temperatures/low frequencies.

Table 5.2 Values of input parameters with the change of h_0

Parameters	h_0/t	n	a (mm)	ϕ_{m_b}	ϕ_{m_c}
	0.58	11.5	1.67	9.4%	10.6%
Values	0.25	9.1	2.2	13.5%	6.5%
	0.125	8.8	2.35	14.9%	5.1%
	0	8.5	2.53	17.3%	2.7%

a. $|E_{mix}{}^*|$-f curve for PA mix-1   b. $|\delta_{mix}|$-f curve for PA mix-1
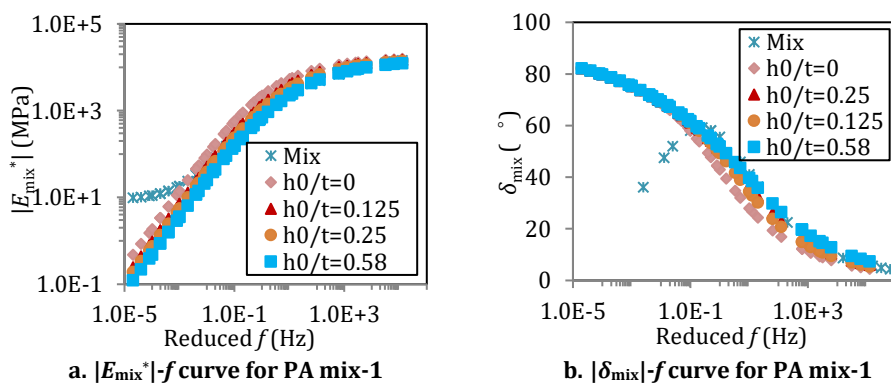
Figure 5.17 Sensitivity of predicted modulus on mortar's thickness

5.4.3.2 *Sensitivity of predicted E_{mix}^* on v_{mor}*

The predicted results of E_{mix}^* using different values of v_{mor} are shown in Figure 5.18. With the increase of v_{mor}, the predicted values of $|E_{mix}^*|$ increase, whereas the predicted values of δ_{mix} decrease. When the value of v_{mor} approaches 0.5, the predicted values of $|E_{mix}^*|$ become much higher than the experimental values, whereas the values of δ_{mix} are far below. It can be postulated that if higher values of v_{mor} are used at lower frequencies, the predicted values of $|E_{mix}^*|$ and δ_{mix} may match with the experimental results. Therefore, in order to understand the effect of v_{mor} on the predicted results of E_{mix}^*, and to figure out if increasing the value of v_{mor} is a logical way to improve the accuracy of the predictions, the effect of v_{mor} on the behaviour of the mortar was investigated.

| a. $|E_{mix}^*|$-f curve for PA mix-1 | b. $|\delta_{mix}|$-f curve for PA mix-1 |
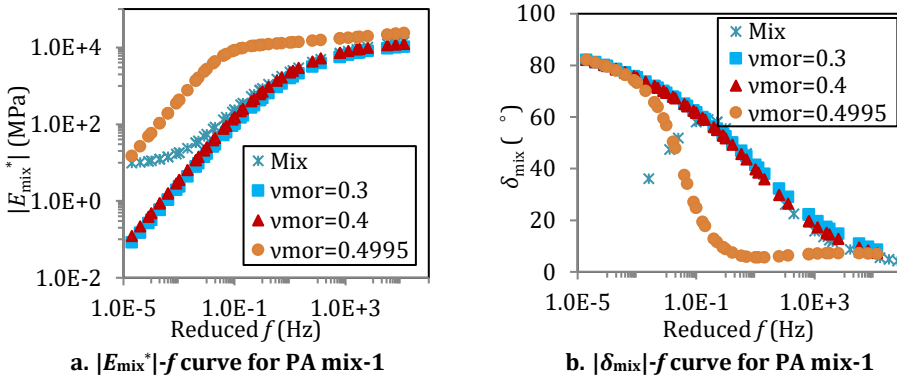
Figure 5.18 Sensitivity of predicted modulus on mortar's Poisson's ratio

In Dvorkin's model, the properties of the mortar are described using Equations (5.4) and (5.5). The stiffness of the mortar in the normal direction S_{n_m} ($2G_{mor}(1-v_{mor})/(1-2v_{mor})$) is a function of both G_{mor} and v_{mor}. Figure 5.19 shows the calculated results of $S_{n\_m}/2G_{mor}$ (or $(1-v_{mor})/(1-2v_{mor})$) when the value of v_{mor} ranges from 0 to 0.5. It can be observed that when v_{mor} is smaller than 0.45, the value of $S_{n\_m}/2G_{mor}$ is not higher than 6. This indicates that when v_{mor} is smaller than 0.45, the value of S_{n_m} is at most 12 times of G_{mor}. Since G_{mor} is much lower than the stiffness of aggregates, the value of S_{n_m} should be much lower than the stiffness of aggregates as well. In this case, the softer mortar, which is much easier to deform, governs the stiffness of the two-particle system (F_n/δ_n). Therefore, in Figure 5.18, it was observed that when v_{mor} is equal to 0.3 and 0.4, the predicted results of $|E_{mix}^*|$ and δ_{mix} follow the same shapes as $|G_{mor}^*|$ and δ_{mor}, respectively.

On the contrary, when v_{mor} is higher than 0.45, the value of S_{n_m} increases dramatically. When v_{mor} approaches 0.5, S_{n_m} becomes infinite, which indicates that the mortar behaves as a rigid body. In this case, when F_n is applied, only particles deform, and thus the predicted modulus of the mix relies on the properties of the aggregate particles. Since the aggregate particles are stiffer and behave as elastic materials, the

predicted properties of the mix (see Figure 5.18) tend to be stiff (high value of $|E_{mix}^*|$) and elastic (low values of δ_{mix}) as well.
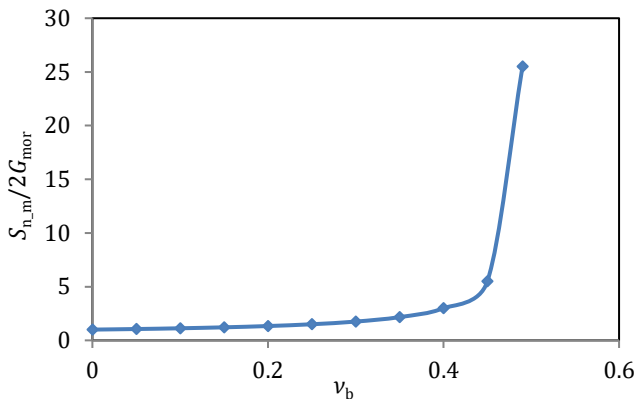
Figure 5.19 Sensitivity of mortar's normal stiffness on Poisson's ratio

From the above discussions, it can be concluded that the effect of ν_{mor} on predicted $|E_{mix}^*|$ and δ_{mix} is related to the assumption that with the increase of ν_{mor}, the mortar behaves like a rigid body. In this case, when two aggregate particles approach each other, the mortar does not have any deformation, while only aggregates deform. However, in a real PA mix, when ν_{mor} approaches 0.5 at high temperatures/low frequencies, it is expected that the mortar behaves more like a viscous material which is quite easy to be deformed, while the deformation of the substantially stiff aggregates is much lower. It is obvious that in these two cases, the properties of the mortar are totally different. Therefore, although the predictions with higher values of ν_{mor} may match the experimental results numerically, the physical mechanism behind these predictions does not seem to be realistic.

5.4.4 Limitation of Dvorkin's model and possible explanations

Predicted results in Figure 5.16 show that Dvorkin's model performs better in predicting the modulus of PA mixes at higher frequencies than CBMM, especially for mixes with densely packing aggregate particles; however, it still fails to provide accurate predictions at lower frequencies. Following sensitivity analyses further reveal that it is impossible (or unreasonable) to improve the accuracy of the predictions at lower frequencies by varying the values of input parameters.

The limitation of Dvorkin's model can be related to the assumption that in a bonded granular material, a load is always transferred through the mortar between adjacent particles. This assumption is clearly reflected by Equations (5.2) and (5.3), where the total deformation of a two-bonded particle system is the sum of the deformation of the particles and the deformation of the mortar. This assumption is

suitable at low temperatures/high frequencies because, under these conditions, the mortar between two particles is stiff enough to transfer a high level of load from one particle to the other. Even if a particle-to-particle direct contact area forms at the same time, since the total particle-mortar contact area is expected to dominate over the particle-to-particle contact area, the overall stiffness of the mix is governed by the behaviour of the mortar.

On the contrary, at high temperatures/low frequencies, the mortar is too soft to effectively transfer loads among adjacent particles. Compared to the soft mortar, particle-to-particle direct contacts are supposed to play a leading role in providing the load transfer capacity for the mix. In this case, the assumption in Dvorkin's model is not applicable anymore, and thus the predictions start to differ from the experimental results.

5.5 Conclusions

This chapter presented a methodology to use Dvorkin's model to predict the stiffness of PA mixes. The predicted results were compared to those from CBMM and the experimental values. In order to improve the accuracy of the predictions at lower frequencies, the sensitivities of the predicted results on geometric input parameters and the Poisson's ratio of the mortar were analysed. In the end, the limitation of Dvorkin's model was highlighted. Based on the obtained results, the following conclusions can be drawn:

- In the proposed microstructure model, a PA mix was simulated as an assembly of identical spherical particles that are covered and bonded by mortar materials with uniform thicknesses.

- Geometric parameters were determined in a way that: the radius of the spherical particles was determined from the aggregate gradation; the thickness of the coating mortar was determined from the mortar content; the minimum distance between two adjacent particles and the coordination number were determined from air voids content, and the radius of the binding mortar was finally determined on the basis of the values of other parameters.

- Based on the proposed microstructure model, the stiffness of PA mixes was calculated in three steps. At first, the stiffness of the skeleton framework consisting of aggregate particles and the binding mortar was predicted using Dvorkin's model. Then the matrix's stiffness of an equivalent two-phase composite, whose stiffness was identical to that of the skeleton framework, was back-calculated using CBMM. At last, by adding the coating mortar to the matrix, the stiffness of PA mixes was calculated using CBMM again.

- At higher frequencies, better predictions were obtained using Dvorkin's model, especially for a densely compacted PA mix. However, Dvorkin's model showed the same limitation as CBMM that at lower frequencies, the predicted dynamic moduli were significantly lower than the experimental results, and moreover, the predicted phase angle did not show a decreasing trend.

- The performance of Dvorkin's model cannot be significantly improved by varying the values of the geometric parameters. By varying the Poisson's ratio of the mortar, the predictions may match the experimental results numerically. However, the physical mechanism behind these predictions that the mortar behaves like a rigid body does not seem to be realistic.

- The limitation of Dvorkin's model is related to the assumption that in a bonded granular material, a load is always transferred through the mortar between adjacent particles. This assumption is valid at higher frequencies, while at lower frequencies, the load is supposed to be mainly transferred through the particle-to-particle direct contacts.

5.6 References

CHANG, C. S. & GAO, J. 1997. Rheological modeling of randomly packed granules with visco-elastic binders of Maxwell type. *Computers and Geotechnics,* 21**,** 41-63.

CHANG, C. S. & LIAO, C. L. 1994. Estimates of Elastic Modulus for Media of Randomly Packed Granules. *Applied Mechanics Reviews,* 47**,** S197-S206.

CHANG, C. S., SHI, Q. S. & ZHU, H. 1999. Microstructural Modeling for Elastic Moduli of Bonded Granules. *Journal of Engineering Mechanics,* 125**,** 648-653.

CHANG, K.-N. & MEEGODA, J. 1997. Micromechanical Simulation of Hot Mix Asphalt. *Journal of Engineering Mechanics-asce - J ENG MECH-ASCE,* 123.

CHEUNG, C. Y., COCKS, A. C. F. & CEBON, D. 1999. Isolated contact model of an idealized asphalt mix. *International Journal of Mechanical Sciences,* 41**,** 767-792.

DVORKIN, J., BERRYMAN, J. & NUR, A. 1999. Elastic moduli of cemented sphere packs. *Mechanics of Materials,* 31**,** 461-469.

DVORKIN, J., NUR, A. & YIN, H. 1994. Effective properties of cemented granular materials. *Mechanics of Materials,* 18**,** 351-366.

LI, G., LI, Y., METCALF, J. B. & PANG, S.-S. 1999. Elastic Modulus Prediction of Asphalt Concrete. *Journal of Materials in Civil Engineering,* 11**,** 236-241.

MARCADON, V., HERVE, E. & ZAOUI, A. 2007. Micromechanical modeling of packing and size effects in particulate composites. *International Journal of Solids and Structures,* 44**,** 8213-8228.

SHASHIDHAR, N. & SHENOY, A. 2002. On using micromechanical models to describe dynamic mechanical behavior of asphalt mastics. *Mechanics of Materials,* 34**,** 657-669.

SHU, X. & HUANG, B. 2008. Dynamic Modulus Prediction of HMA Mixtures Based on the Viscoelastic Micromechanical Model. *Journal of Materials in Civil Engineering,* 20**,** 530-538.

UNDERWOOD, B. S. 2011. *Multiscale constitutive modeling of asphalt concrete.*

UNDERWOOD, B. S. & KIM, Y. R. 2014. A four phase micro-mechanical model for asphalt mastic modulus. *Mechanics of Materials,* 75**,** 13-33.

ZHU, H., CHANG, C. S. & RISH, J. W. 1996. Normal and tangential compliance for conforming binder contact II: Visco-elastic binder. *International Journal of Solids and Structures,* 33**,** 4351-4363.

ZHU, H. & NODES, J. E. 2000. Contact based analysis of asphalt pavement with the effect of aggregate angularity. *Mechanics of Materials,* 32**,** 193-202.

6

A hybrid micromechanical model for asphalt concrete response simulation

6.1 Introduction

Previous chapters have shown that further improvement in the accuracy of asphalt concrete response predictions at the lower frequencies range requires considering the stiffening effect of the particle-to-particle direct contacts. In fact, the role of the particle-to-particle contacts in the response of asphalt materials has been widely realized by researchers (Buttlar et al., 1999, Underwood and Kim, 2013, Shu and Huang, 2008). However, the challenge is to quantitatively evaluate its stiffening effect on the mechanical properties of asphalt materials.

Until now, in the pavement field, very few approaches have been developed to account for the stiffening effect of the particle-to-particle direct contacts. The percolation theory, as introduced in the previous chapter, is one of these approaches. However, it does not further improve the accuracy of the predictions when the concentration of particles is higher than 40%. The main reason for the failure of the percolation theory is that it simply treats the connected particles as an entire phase while it never directly considers the contacts among different particles (Underwood and Kim, 2014).

Underwood & Kim (2013) developed a microstructural association model where the stiffening effect of the particle-to-particle contact is quantified using a structuralization index (SI). The value of SI can be calculated from the measured packing properties of the aggregates in a mix. It was further pointed out that the SR (stiffening ratio)-SI relationship developed at a lower scale can be used to obtain the stiffening ratio of materials at higher scales. Therefore, the prediction of the modulus of an asphalt mixture can be achieved by using the SR-SI relationship that was developed in the mastic scale. The advantage of doing this is that performing laboratory tests on the mastic scale is much less time-consuming than that on the mixture scale.

In comparison with the percolation theory, the use of SI in the microstructural association model is a more reasonable approach for capturing the particle-to-particle direct contact effect in a composite. Underwood & Kim (2013) showed that the SR-SI relationship could be well established in the mastic scale and using this relationship the modulus of asphalt mixtures in a wide temperature range (from 20°C to 54°C) could be well predicted. However, the establishment of all the equations in the model requires a large number of laboratory tests. In addition, in the model, there are many parameters required to be back-calculated. Overall, the implementation of the microstructural association model is tedious and complicated.

Apart from the percolation theory and the microstructural association model, calibration factors were also used to account for the stiffening effect of the particle-to-particle direct contacts (Sun et al., 2017, Cai et al., 2020). Since calibration methods do

not give any fundamental insight into the particle direct contacts, a more logical and reasonable method needs to be developed.

Although the characteristics of the particle direct contacts have not been thoroughly studied in the field of pavement engineering, a large amount of relevant research work has been conducted in other engineering fields like granular solids. In the field of granular solids, the phenomenon that two solids form a finite contact area when they are compressed together is usually referred to as "Hertzian contact". The work of Hertz (1882) provides the relationship between the radius of the contact area, the applied normal force, the radii of the solids in contact and the elastic properties of the materials (HERTZ, 1882, Fischer-Cripps, 1999). Further research studies extended Hertz's work from normal contact to a more general case of oblique contact where not only a normal contact force but also tangential contact forces exist at the contact surface (Mindlin, 1949, Walton, 1978).

Based upon the contact law between two contacting particles, researchers (Digby, 1981, Walton, 1987, Chang and Liao, 1994) have further developed DBMM to estimate the effective moduli of un-bonded granular materials, see Figure 6.1. In these models, an un-bonded granular material is described as a pack of aggregate particles with uniform sizes. Based upon such geometric configuration, equations for calculating the effective moduli of un-bonded granular materials have been derived by different researchers (Digby, 1981, Walton, 1987, Chang and Liao, 1994). In this study, equations derived by Walton (Walton, 1987) were used and thus DBMM for un-bonded granular materials is referred to as Walton's model in the following sections.
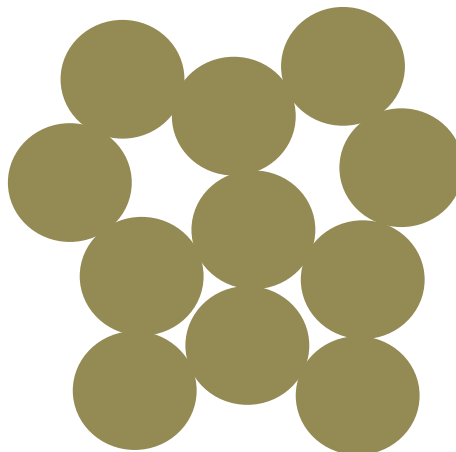

Figure 6.1 Illustration of DBMM for un-bonded granular materials

Walton's model has been widely used in the field of granular solids (Chang et al., 1989); however, it has never been used to account for the stiffening effect of the particle-to-particle direct contacts in asphalt materials. Therefore, the aim of this

chapter is to develop a way of using Walton's model for determining the stiffening effect of the particle-to-particle direct contacts in a PA mix. Furthermore, in order to achieve the main objective of this study, a hybrid micromechanical model that combines the volume-filling stiffening effect and the stiffening effect of the particle-to-particle direct contacts is developed. In the end, the performance of the developed model in predicting the total stiffness of PA mixes is assessed.

6.2 Introduction of Walton's model

The way that Walton's model uses to predict the stiffness of an un-bonded granular material is similar to that used by Dvorkin's model. The homogenization technique introduced in Section 5.2.2 is also applicable to un-bonded granular materials, while the contact laws are different. Therefore, in this section, the introduction of Walton's model mainly focuses on the contact law between two contacting particles. Furthermore, using the same homogenization technique, the effective moduli of an un-bonded granular material can be derived.

6.2.1 Contact law of a two-contacting particles system

In Walton's model, two identical spheres are compressed together in such a manner that the centre of the upper sphere undergoes a displacement of δ_n in the normal direction and δ_τ in the tangential direction; and the lower sphere undergoes an equal but opposite displacement, see Figure 6.2. Under the given compression, a circular contact area between two spheres is formed and the radius of the area a is given by:

$$a^2 = R\delta_n \tag{6.1}$$

where R is the radius of the spheres.

In the case of infinitely rough spheres (no relative slip between two spheres), the stresses acting on the contact area, σ_z (normal stress) and σ_τ (tangential stress), are given as:

$$\sigma_z = \frac{2}{\pi^2 RB}\left(a^2 - r^2\right)^{1/2} \tag{6.2}$$

$$\sigma_\tau = \frac{4\delta_\tau}{\pi^2 R(2B+C)\delta_n}\left(a^2 - r^2\right)^{1/2} \tag{6.3}$$

where

$$B = \frac{1}{4\pi}\left(\frac{1}{G_a} + \frac{1}{\lambda_a + G_a}\right) = \frac{1 - v_a^2}{\pi E_a}, \ C = \frac{1}{4\pi}\left(\frac{1}{G_a} - \frac{1}{\lambda_a + G_a}\right) = \frac{v_a\left(1 + v_a\right)}{\pi E_a} \tag{6.4}$$

where λ_a and G_a denote the Lame moduli of the spheres; E_a and ν_a are Young's modulus and Poisson's ratio of the spheres, respectively; and $r=(x^2+y^2)^{1/2}$. By integrating σ_z and σ_τ across the contact area, the forces acting on the contact surface can be obtained as:

$$F_n = \frac{4R^{1/2}\delta_n^{3/2}}{3\pi B} \tag{6.5}$$

$$F_\tau = \frac{8\delta_\tau \left(R\delta_n\right)^{1/2}}{3\pi\left(2B+C\right)} \tag{6.6}$$
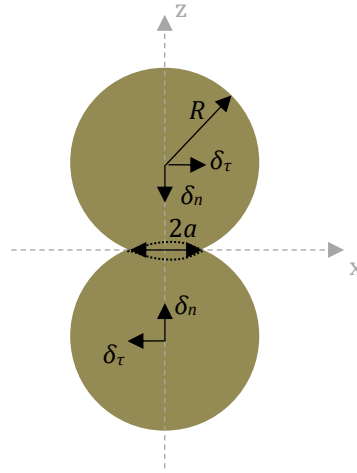
Figure 6.2 A two-contacting particles system

According to the definition of the stiffness of a two-particle system in Equation (5.1) (see Chapter 5), the values of S_n and S_τ for a two-contacting particles system can be derived from Equations (6.5) and (6.6) as:

$$S_n = \frac{4R^{1/2}\delta_n^{1/2}}{3\pi B} \tag{6.7}$$

$$S_\tau = \frac{8\left(R\delta_n\right)^{1/2}}{3\pi\left(2B+C\right)} \tag{6.8}$$

6.2.2 Effective moduli of an un-bonded granular material

Substituting the expression of δ_n in the global coordinate system in Equation (5.14) into Equations (6.7) and (6.8), the values of S_n and S_τ can be related to the average strain of the granular material as

$$S_n = \frac{4R}{3\pi B}\left(-\langle\varepsilon\rangle_{kl} I_k^{(sr)} I_l^{(sr)}\right)^{1/2} \tag{6.9}$$

$$S_\tau = \frac{8R}{3\pi(2B+C)}\left(-\langle\varepsilon\rangle_{kl} I_k^{(sr)} I_l^{(sr)}\right)^{1/2} \tag{6.10}$$

Substituting (6.9) and (6.10) into the general expression for the average stress of a granular material in Equation (5.29), the average stress <σ> for an un-bonded granular material can be given as (Walton, 1987):

$$\langle\sigma\rangle_{ij} = \frac{\phi_a n_d}{\pi^2 B(2B+C)}\left[\begin{array}{l} B\left\langle\left(-\langle\varepsilon\rangle_{pq} I_p I_q\right)^{1/2}\langle\varepsilon\rangle_{jk} I_k I_i\right\rangle + B\left\langle\left(-\langle\varepsilon\rangle_{pq} I_p I_q\right)^{1/2}\langle\varepsilon\rangle_{ik} I_k I_j\right\rangle \\ + C\left\langle\left(-\langle\varepsilon\rangle_{pq} I_p I_q\right)^{1/2}\langle\varepsilon\rangle_{kl} I_i I_j I_k I_l\right\rangle \end{array}\right] \tag{6.11}$$

where n_d is the average number of the particles that are in direct contact with one particle; ϕ_a is the volume fraction of the particles.

When a hydrostatic strain $\langle\varepsilon\rangle_{ij}=\varepsilon\delta_{ij}$ is applied on the un-bonded granular material, the corresponding confining pressure can be computed using Equation (6.12) as:

$$p = \frac{\phi_a n_d (-\varepsilon)^{3/2}}{3\pi^2 B} \tag{6.12}$$

Furthermore, Young's modulus of the system, denoted as E^{eff}, can be related to the confining pressure using Equation (6.13).

$$E^{eff} = \frac{5B+C}{2(5B+2C)}\left(\frac{3\phi_a^2 n_d^2 p}{\pi^4 B^2}\right)^{1/3} \tag{6.13}$$

6.3 Structuralization of aggregate particles in a PA mix

As mentioned earlier, aggregate particles are structuralized, and direct particle-to-particle contacts form in an asphalt mixture. Researchers (Underwood and Kim, 2013) have widely realized the important role played by the structuralization of aggregate particles in the mechanical properties of the mix. However, up to now, a reasonable explanation about how the aggregate particles in a mix are structuralized has not been provided, and because of that, an effective methodology for quantifying their contributions has not been developed. Therefore, in this study, before the development of such a methodology, the structuralization of aggregate particles in a PA mix was investigated.

In order to easily figure out how the particle-to-particle direct contacts form, a simplified microstructure of a PA mix, which consists of aggregate particles packing

together and mortar bridges randomly distributing around adjacent particles, was used, see Figure 6.3a. In this microstructure, particle A was taken as an example and the interactions between particle A and its surrounding particles (i.e. particles B, C, and D) were analysed.

Figure 6.3b shows the loading condition performed in this study (as described in Chapter 2) where a compressive strain is applied to a PA mix specimen in the vertical direction. In such a case, it is expected that the particle-to-particle direct contacts form between particle A with particle B and particle D. As a result, two compressive forces F_{AB}^C and F_{AD}^C are subjected to particle A. However, with these two compressive forces, particle A cannot be in balance and it tends to move in the lateral direction. In this case, in order to keep the whole structure of the mix stable, a tensile force is needed to suck particle A back. When there is no confinement applied to the mix in the lateral direction, the only way to provide a tensile force is the sucking effect of the mortar bridge between particle A with particle C. In other words, as a result of the outward motion of particle A due to the forces F_{AB}^C and F_{AD}^C, for equilibrium, a tensile force F_{AC}^T needs to be generated by the sucking effect of the mortar bridge which restrains the uncontrolled lateral displacement of the aggregate, enhancing thus the contacts between particle A with particle B and D. Implicitly, the mortar bridge acts as an additional lateral confinement mechanism.

| a. An aggregates pack | b. Compressive load | c. Tensile load |
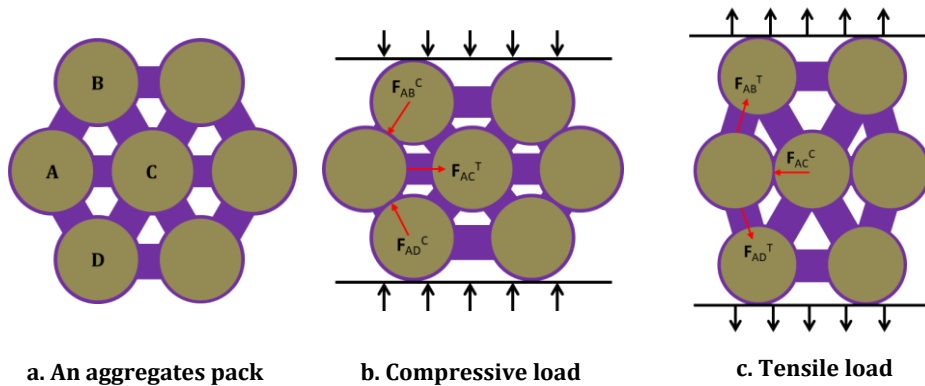
Figure 6.3 Illustration of the aggregates structuralization in PA mixes

The important role played by the mortar bridges in the generation of particle direct contacts can be seen under the tensile loading condition as well. As can be seen in Figure 6.3c, the sucking effect of the mortar bridges between particle A with particles B and D (i.e. tensile forces F_{AB}^T and F_{AD}^T) enables the tensile response of the material and, in a manner equivalent to Poisson's effect, enhances the particle contact between particle A with particle C (i.e. compressive force F_{AC}^C) in the lateral direction.

From the above discussions, it can be concluded that what prevents an unconfined PA mix from collapsing into a pile of rocks is the sucking action of the mortar bridges between aggregate particles, which encourages particle-to-particle interactions and, as such, enhances the stiffness of the system of aggregate particles. In light of these realizations, a methodology that can quantify the contribution from the structuralization of aggregate particles to the total stiffness of a mix was further developed.

6.4 Contribution of particles structuralization to PA mix's stiffness

Based on the discussions in the above section, it is known that both in tension and compression, the generation of the contact forces between adjacent particles is supported by the sucking effect of the mortar bridges. This effect of the mortar bridges on the structuralization of aggregate particles in a PA mix is quite similar to the effect of the confinement on the structuralization of granular materials since both of them serve as a precondition for the formation of particle-to-particle direct contacts. Therefore, when Walton's model is used to describe the structuralization of aggregate particles in a PA mix, the value of p in Equation (6.13) can be considered as the sucking effect of the mortar bridges. From Figure 6.3, it is known that the sucking effect of mortar bridges is related to the stresses in the mortar phase. With this realization, the following equation was proposed to calculate the value of p:

$$p = \frac{\langle\sigma\rangle_{11} + \langle\sigma\rangle_{22} + \langle\sigma\rangle_{33}}{3} \tag{6.14}$$

where $\langle\sigma\rangle_{ii}$ ($i=1, 2, 3$) is the stress in the mortar bridges in three different directions.

In Chapter 5, it was explained that mortar bridges exist among aggregate particles, and the three-dimensional confinement provided to the mortar by the presence of the surrounding particles makes the mortar's response stiffer than that in a typical DSR test and, as such, improves its capability to resist deformation. Therefore, the estimation of the load-bearing capability of the mortar bridges should take into account the stiffening effect on the mortar due to the presence of the particles. With this realization, it was further proposed that the value of $\langle\sigma\rangle_{ii}$ in Equation (6.14) was calculated using Dvorkin's model which describes the load-bearing capability of a mortar-particle system, see Equation (5.29).

Since a uniaxial strain $\langle\varepsilon\rangle_3$ was applied to the mix in the laboratory tests, the value of $\langle\varepsilon\rangle_{ij}$ in Equation (5.29) was written as

$$\langle\varepsilon\rangle_{ij} = \langle\varepsilon\rangle_3 \delta_{i3}\delta_{j3} \tag{6.15}$$

Substituting Equation (6.15) into Equation (5.29), the value of $\langle\sigma\rangle_{ii}$ was calculated as

$$\langle\sigma\rangle_{11} = \frac{3n_s\phi_a\left(R+h_0\right)^2\langle\varepsilon\rangle_3}{4\pi R^3}\left[\left(S_n - S_\tau\right)\langle I_1^2 I_3^2\rangle\right] \tag{6.16}$$

$$\langle\sigma\rangle_{22} = \frac{3n_s\phi_a\left(R+h_0\right)^2\langle\varepsilon\rangle_3}{4\pi R^3}\left[\left(S_n - S_\tau\right)\langle I_2^2 I_3^2\rangle\right] \tag{6.17}$$

$$\langle\sigma\rangle_{33} = \frac{3n_s\phi_a\left(R+h_0\right)^2\langle\varepsilon\rangle_3}{4\pi R^3}\left[\left(S_n - S_\tau\right)\langle I_3^4\rangle + S_\tau\langle I_3^2\rangle\right] \tag{6.18}$$

where the values of S_n and S_τ can still be determined using the method as introduced in Section 5.2.

Once the value of p is known, the stiffness due to the particle-to-particle contacts can be further calculated using Equation (6.13). It is worth highlighting here that:

- n_s refers to the number of mortar bridges that surround one particle and provide sucking effects for this particle.

- since the mortar bridges that surround one particle (the number of which is n as described in Chapter 5) are either stretched to provide the sucking effect (the number of which is n_s) or compressed along with the formation of the particle-to-particle direct contacts (the number of which is n_d), the sum of n_s and n_d is identical to the value of n.

- theoretically, the values of n_s and n_d can be determined according to the stress states of the mortar bridges. However, since the stresses of the mortar bridges are material responses on the microscale, it is difficult to determine the values of these stresses and thus the values of n_s and n_d in an analytical way. Therefore, in this research, a simple method in which the values of n_s and n_d were determined in the case when the stiffness of the mix was the maximum was proposed. The underlying assumption was that a mix always adjusted itself to be the strongest in order to sustain an external load. Following the proposed method, the values of n_s and n_d were calculated as 6 and 5.5 for PA mix-1, respectively, while for PA mix-2, the values of n_s and n_d were 3 and 6.5, respectively.

In this section, a methodology for determining the stiffening effect of the particle-to-particle contacts in a PA mix was introduced. Furthermore, a hybrid micromechanical model, which combines the volume-filling stiffening effect and the stiffening effect of the particle-to-particle contacts, was developed to predict the total stiffness of the mix. In the following section, this hybrid micromechanical model will be introduced.

6.5 A hybrid micromechanical model to predict the stiffness of PA mixes

As explained earlier, the stiffness to resist the overall deformation of a mix comes from the volume-filling stiffening effect together with the stiffening effect of the particle-to-particle direct contacts. Following this thought, a parallel arrangement of these two mechanisms was proposed in order to calculate the total stiffness of the mix E_{mix}^*, see Figure 6.4.
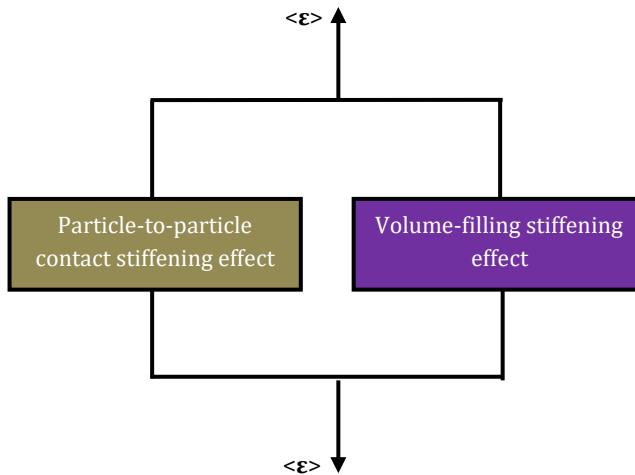
Figure 6.4 The proposed hybrid micromechanical model

In order to further physically understand how the proposed hybrid micromechanical model works, a simple constitutive model, known as the standard solid model, was used to simulate the mechanical response of each stiffening mechanism and the behaviour of their combined effects, see Figure 6.5. According to the previous chapters, it was known that the volume-filling stiffening effect provided a liquid-like behaviour of a mix. Therefore, in Figure 6.5 a Maxwell model was used to describe the mechanical response of the volume-filling stiffening effect. On the other hand, since the mechanical response of a mix due to the particle-to-particle direct contacts is elastic, a spring was used for the simulation.
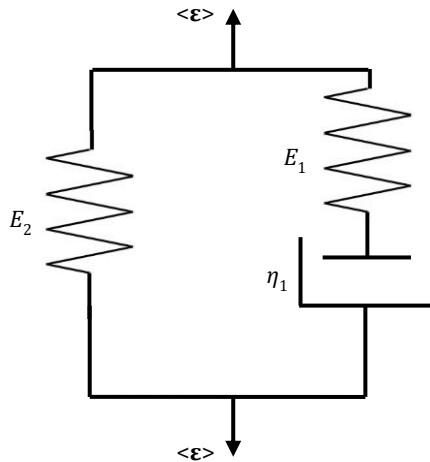
Figure 6.5 Standard solid model

Figure 6.6 illustrates the mechanical response (dynamic modulus and phase angle) of a Maxwell model. Various curves were plotted by setting the modulus of the spring and the viscosity of the dashpot as different values. The similarity of these curves' shapes indicates that a mix always shows a liquid-like behaviour if only the volume-filling stiffening effect is considered.
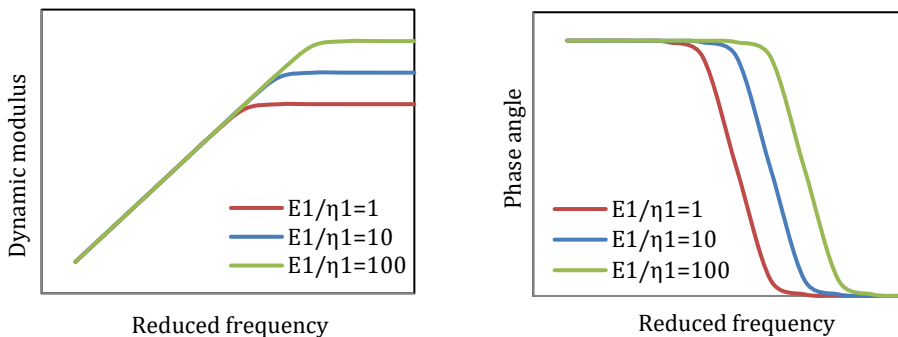
Figure 6.6 Mechanical responses of a Maxwell model

By contrast, with the addition of a spring in parallel, the total model shows a PA mix-like behaviour that the dynamic modulus reaches an asymptotic value at very low frequencies and a peak value appears in the phase angle curve, see Figure 6.7. This observation verifies the necessity of considering the particle-to-particle direct contacts in order to accurately predict the mechanical properties of PA mixes. In addition, it also proves the validity of arranging the volume-filling stiffening effect and the stiffening effect of the particle-to-particle direct contacts in parallel in the proposed hybrid micromechanical model.
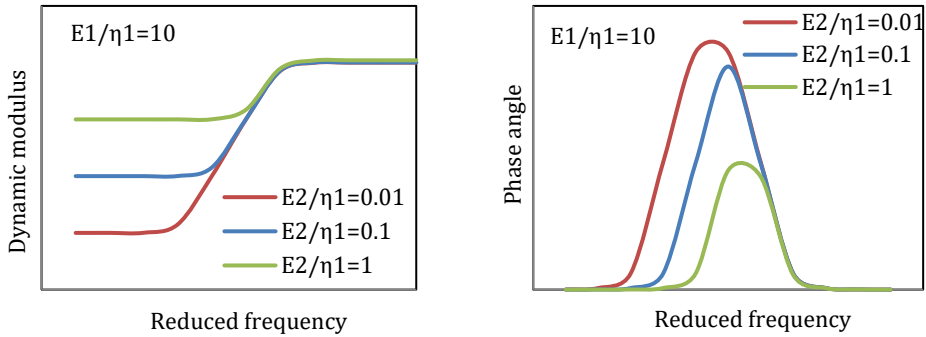
Figure 6.7 Mechanical responses of the standard solid model

In a parallel arrangement, the overall stiffness of a composite is the sum of the stiffnesses of individual components. Thus, the value of E_{mix}^* can be calculated by summing up the stiffness due to the volume-filling stiffening effect, represented as E_{mix}^m, and the stiffness resulting from the particle-to-particle contacts, denoted as E_{mix}^c, see Equation (6.19). Since the values of E_{mix}^m and E_{mix}^c are frequency/temperature-dependent, they are both represented as complex numbers in the frequency domain. Therefore, the calculated result of E_{mix}^* is also a complex number, which indicates that both the dynamic modulus $|E_{mix}^*|$ (the magnitude of E_{mix}^*) and the phase angle δ_{mix} of the mix can be obtained using Equation (6.19).

$$E_{mix}^*(f) = E_{mix}^m(f) + E_{mix}^c(f) \tag{6.19}$$

It is noted here that according to the previous chapters (Chapter 4 and Chapter 5), the value of E_{mix}^m can be estimated using either CBMM (i.e. the MT model, the SC model, the GSC model, etc.) or DBMM (i.e. Dvorkin's model). The comparison among different micromechanical models showed that Dvorkin's model predicts the volume-filling stiffening effect more accurately. Therefore, Dvorkin's model was used in this study to estimate the value of E_{mix}^m.

6.6 Results and discussion

6.6.1 Predicted results of $|E_{mix}^*|$

Using the proposed hybrid micromechanical model, the predicted results of $|E_{mix}^*|$ were obtained, see Figure 6.8. In order to compare the contribution from the volume-filling stiffening effect with that from the particle-to-particle contacts, the values of $|E_{mix}^m|$ and $|E_{mix}^c|$ are also plotted in the same figures.

Comparing the predicted results of $|E_{mix}^m|$ and $|E_{mix}^c|$, it can be seen that both the volume-filling stiffening effect and the stiffening effect of the particle-to-particle contacts make contributions to the stiffness of the mix in the whole frequency range.

However, the dominant mechanism changes at different frequencies. At higher frequencies, the values of $|E_{mix}{}^m|$ are much higher than $|E_{mix}{}^c|$, and the values of $|E_{mix}{}^m|$ match quite well with the experimental results. These observations indicate that at higher frequencies, the volume-filling stiffening effect dominates the behavior of the mix.

With the decrease of frequencies, the value of $|E_{mix}{}^m|$ decreases sharply, while the decrease of $|E_{mix}{}^c|$ is much less significant than that of $|E_{mix}{}^m|$. From a certain frequency, the value of $|E_{mix}{}^c|$ starts to be higher than $|E_{mix}{}^m|$. When the frequency is very low, the value of $|E_{mix}{}^c|$ is significantly dominant over the value of $|E_{mix}{}^m|$, and in this case, the measured value of $|E_{mix}{}^*|$ closely follows the change of $|E_{mix}{}^c|$. These observations clearly show that at very lower frequencies, the stiffening effect of the particle-to-particle contact plays a leading role in the overall behaviour of the mix.
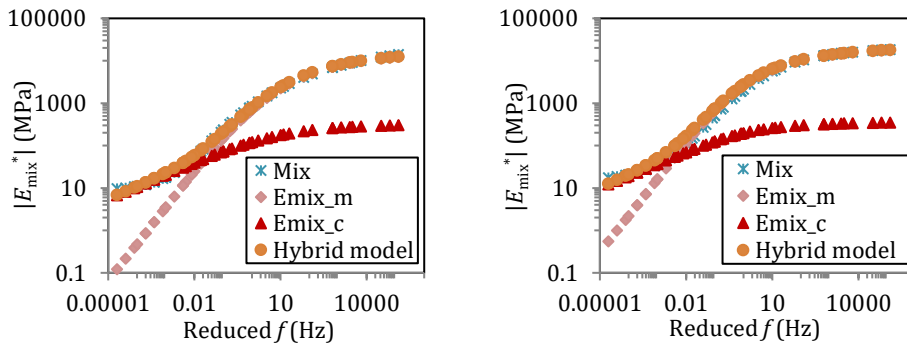
a. Dynamic Young's modulus of PA mix-1   b. Dynamic Young's modulus of PA mix-2

Figure 6.8 Predicted results of dynamic Young's modulus using the proposed methodology

The change of the dominant mechanism at different frequencies can be explained by considering the properties of the mortar materials. At higher frequencies, the stiffness of the mortar is quite high. Beyond that, the mortar-particle contact area is much bigger than the direct contact area between two particles. Therefore, compared to the particles' direct contacts, the mortar can provide a much stronger resistance to prevent the overall deformation of the mix. By contrast, at lower frequencies, the mortar is too soft, and thus the resistance provided by mortar can be almost neglected. In this case, the resistance provided by the particles' direct contacts becomes relatively significant.

By summing the values of $|E_{mix}{}^m|$ and $|E_{mix}{}^c|$ up, the predicted results of $|E_{mix}{}^*|$ were obtained. It can be seen that the proposed model performs quite well in the whole frequency range. The predicted values of $|E_{mix}{}^*|$, showing asymptotic behaviours at both very high frequencies and very low frequencies, match well with the experimental

results. The agreement between the predictions and the experimental results justifies the proposed methodology for predicting the modulus of PA mixes.

6.6.2 Predicted results of δ_{mix}

The predicted results of δ_{mix} are shown in Figure 6.9. Additionally, in order to clearly show the change of the predicted phase angle after the consideration of the particle-to-particle contacts, the phase angle with only the consideration of the volume-filling stiffing effect δ_{mix}^{m} (predicted from Dvorkin's model) is also plotted in the figures.

a. Phase angle of PA mix-1   **b. Phase angle of PA mix-2**
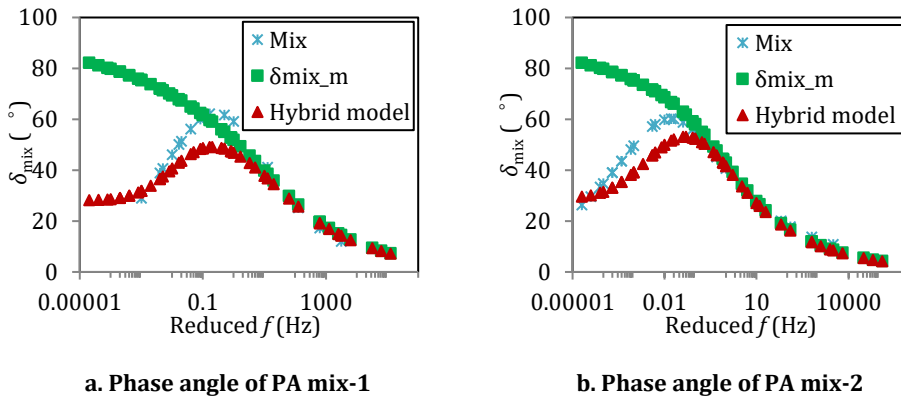
Figure 6.9 Predicted results of phase angle using the proposed methodology

It can be seen that at high frequencies, both the proposed hybrid model and Dvorkin's model provide accurate predictions. This observation further verifies the domination of the volume-filling stiffening effect at higher frequencies. With the decrease of frequencies, the predicted values of δ_{mix}^{m} keep increasing, whereas, because of the consideration of particles' direct contacts, the predicted values of δ_{mix} using the proposed model show a decrease after a peak point.

Overall, in the whole frequency range, it can be claimed that the proposed model provides acceptable predicted results of δ_{mix}. The good agreement between the predicted δ_{mix} and the experimental results further demonstrates the robustness of the proposed micromechanical model.

6.6.3 Effect of compaction effort on the behaviour of PA mixes

In this study, two types of PA mixes which were performed different compaction efforts were investigated. According to the test results, a more compacted mix (i.e. PA mix-2) is stiffer than a mix with less compaction effort. From the macroscopic perspective, the effect of the compaction effort on the behaviour of PA mixes can be attributed to the changes of the volume fractions of individual phases. However, on the basis of previous

analyses, it can be known that from the microscopic perspective, the influence of the compaction effort is much more than just changing the volume fraction of each phase. Therefore, in this part, from the microscopic perspective, a more detailed explanation about the influence of the compaction effort is given.

a. Volume-filling stiffening effect

b. Stiffening effect of particle-to-particle contact
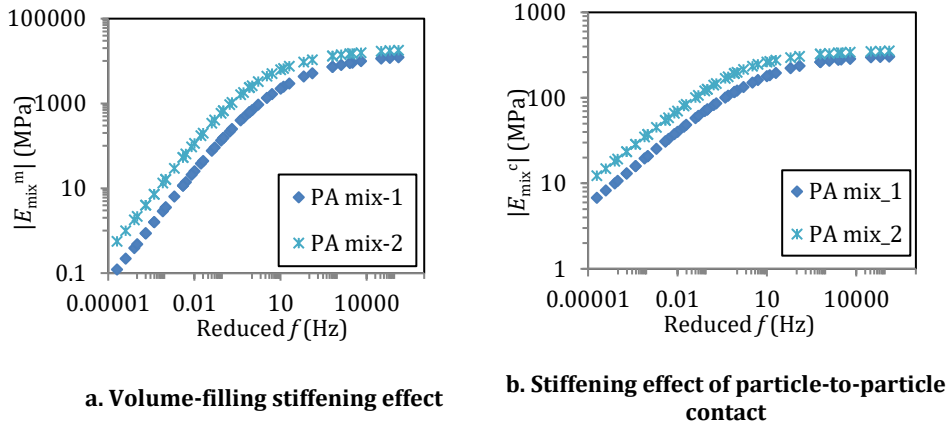
Figure 6.10 Effect of compaction effort on the behaviour of PA mixes

Figure 6.10 shows the comparison of the volume-filling stiffening effect and the stiffening effect of the particle-to-particle contacts between PA mix-1 and PA mix-2. It can be seen that compaction effort can impact the stiffening effects of both mechanisms. From Chapter 5, it was known that the compaction effort affects the volume-filling stiffening effect by changing the microstructural configuration of the mix, i.e. the average distance between connecting particles, the coordination number, and the radius of the bonding mortar.

The influence of the compaction effort on the stiffening effect of the particle-to-particle contacts can be explained from two aspects. Since the compaction effort improves the volume-filling stiffening effect, the confinement for the aggregates pack is enhanced. On top of that, more compaction effort produces a more densely packing stone-on-stone framework, which can be reflected by the increase of the number of particles that are in direct contacts.

6.7 Summary

This chapter interpreted the physical mechanism behind the structuralization of the aggregate particles in PA mixes. On the basis of that, a method to determine the stiffness due to the particles' direct contacts was proposed. Furthermore, a hybrid micromechanical model which combines the volume-filling stiffening effect and the stiffening effect of the particle-to-particle contacts was developed to predict the overall stiffness of a PA mix. In the end, the performance of the proposed model was evaluated

on the basis of experimental results. Based on all the discussions and the obtained results, the following conclusions can be made:

- The sucking action of the mortar bridges between the aggregate particles prevents an unconfined PA mix from collapsing into a pile of rocks, which encourages particle-to-particle interactions and, as such, enhances the stiffness of the system of aggregate particles.

- When Walton's model is used to describe the stiffening effect due to the particle-to-particle contacts in a PA mix, the value of the confinement in the model can be related to the stresses in the mortar phase.

- The stresses in the mortar phase can be estimated using Dvorkin's model since this model takes into account the stiffening effect on the mortar due to the presence of the particles.

- A parallel arrangement of the volume-filling stiffening effect and the stiffening effect of the particle-to-particle contacts can accurately predict both the dynamic modulus and the phase angle of PA mixes in the whole frequency range.

- In the whole frequency range, both the volume-filling stiffening effect and the stiffening effect of the particle-to-particle contacts make contributions to the stiffness of the mix. At higher frequencies, the volume-filling stiffening effect governs the behaviour of the mix, while at lower frequencies, the stiffening effect of the particle-to-particle contacts plays a leading role.

- Compaction effort impacts both the volume-filling stiffening effect and the stiffening effect of the particle-to-particle contacts. Compaction effort affects the volume-filling stiffening effect by changing the microstructural configuration of the mix; while the influence of the compaction effort on the stiffening effect of the particle-to-particle contacts is attributed to the enhancement of the confinement and the generation of more direct particle-to-particle contacts.

6.8 References

BUTTLAR, W., BOZKURT, D., AL-KHATEEB, G. & WALDHOFF, A. 1999. Understanding Asphalt Mastic Behavior Through Micromechanics. *Transportation Research Record: Journal of the Transportation Research Board,* 1681**,** 157-169.
CAI, X., ZHANG, J., ZHANG, H., YAO, Z., CHEN, X. & YANG, J. 2020. Identification of microstructural characteristics in semi-flexible pavement material using micromechanics and nano-techniques. *Construction and Building Materials,* 246**,** 118426.

CHANG, C. S. & LIAO, C. L. 1994. Estimates of Elastic Modulus for Media of Randomly Packed Granules. *Applied Mechanics Reviews,* 47**,** S197-S206.

CHANG, C. S., SUNDARAM, S. S. & MISRA, A. 1989. Initial moduli of particulated mass with frictional contacts. *International Journal for Numerical and Analytical Methods in Geomechanics,* 13**,** 629-644.

DIGBY, P. J. 1981. The Effective Elastic Moduli of Porous Granular Rocks. *Journal of Applied Mechanics,* 48**,** 803-808.

FISCHER-CRIPPS, A. C. 1999. The Hertzian contact surface. *Journal of Materials Science,* 34**,** 129-137.

HERTZ, H. 1882. Verhandlungen des Vereins zur Be Forderung des Gewerbe Fleisses. 61.

MINDLIN, R. D. 1949. Compliance of Elastic Bodies in Contact. *ASME Trans. J. Appl. Mech.,* 16**,** 259-268.

SHU, X. & HUANG, B. 2008. Micromechanics-based dynamic modulus prediction of polymeric asphalt concrete mixtures. *Composites Part B: Engineering,* 39**,** 704-713.

SUN, Y., CHEN, J., PAN, B., SHU, X. & HUANG, B. 2017. Three-Dimensional Micromechanical Complex-Modulus Prediction of Asphalt Concrete Considering the Aggregate Interlocking Effect. *Journal of Materials in Civil Engineering,* 29**,** 04017153.

UNDERWOOD, B. S. & KIM, Y. R. 2013. Microstructural Association Model for Upscaling Prediction of Asphalt Concrete Dynamic Modulus. *Journal of Materials in Civil Engineering,* 25**,** 1153-1161.

UNDERWOOD, B. S. & KIM, Y. R. 2014. A four phase micro-mechanical model for asphalt mastic modulus. *Mechanics of Materials,* 75**,** 13-33.

WALTON, K. 1978. The oblique compression of two elastic spheres. *Journal of the Mechanics and Physics of Solids,* 26**,** 139-150.

WALTON, K. 1987. The effective elastic moduli of a random packing of spheres. *Journal of the Mechanics and Physics of Solids,* 35**,** 213-226.

7

Conclusions and recommendations

Up to now, there are still no readily available and accessible tools to assist pavement practitioners in mitigating ravelling distress of PA mix pavements or making accurate ravelling distress predictions. For this reason, this study proposed a homogenization-based approach which is expected to be able to effectively analyse the propensity of a given PA mix for ravelling without the need for expensive computational facilities. In order to finally implement the proposed approach, this thesis attempted to firstly achieve the approach's first step of accurately estimating the stiffness of a PA mix based on the properties of the mix's individual constituents.

The whole research work was carried out in two steps. The first step mainly focused on the evaluation of commonly used micromechanical models, i.e. SEMM, CBMM and DBMM, for their performances in accurately predicting the mechanical properties of PA mixes. In this step, both the advantages and the limitations of different types of micromechanical models were investigated; and moreover, the fundamental mechanisms that affect the behaviour of PA mixes were analysed. Furthermore, a methodology for accurately predicting the mechanical properties of PA mixes was developed. Based on all the analyses and discussions, the main findings and the recommendations for further research will be summarized in this chapter.

7.1 Conclusions

7.1.1 Evaluation of commonly used micromechanical models

7.1.1.1 *Evaluation of SEMM*

As the first step of this research work, SEMM were evaluated for their capability of accurately predicting the stiffness of PA mixes. As compared to CBMM and DBMM, SEMM are much easier to be implemented. Thus, starting with the evaluation of SEMM is beneficial to easily capture the basic concepts behind the development of different micromechanical models.

Christensen's model, one of the most commonly used SEMM, was investigated. In Christensen's model, one of the critical parameters in the calculation of a mix's stiffness is the so-called contact factor. This factor describes the important role played by the interactions among aggregate particles in the behaviour of the mix. However, the interpretation of the contact factor does not comply with the physical situation where fewer aggregate particles are expected to be in intimate contact at high frequencies/low temperatures. Therefore, a modified expression for Christensen's model, with the introduction of an aggregate organization factor, was proposed. By means of the aggregate organization factor, the frequency/temperature-dependent contribution from the aggregate phase to the total stiffness of a mix can be accounted for. Furthermore, a sigmoidal curve function was proposed to describe the characteristics of the aggregate organization factor in the whole frequency range.

The modified version of Christensen's model is easy to implement and it was verified that this model is capable of accurately predicting the stiffness of PA mixes. However, the limitation of Christensen's model is that laboratory tests are required for calibrating the parameters in the model, and moreover, recalibration is always required when the model is used for a different type of mix.

The limitation of SEMM is related to their assumptions of simply arranging individual phases in parallel or in series. In that case, the stress/strain field in the macroscale and that in the microscale can only have a relationship of either a uniform stress or a uniform strain. However, considering the complicated microstructure of a mix, it is not expected that those relationships are accurate. Therefore, in order to avoid the need for calibrations, further attention was paid to CBMM which can provide more rigorous stress/strain relationships.

7.1.1.2 *Evaluation of CBMM*

CBMM were developed on the basis of Eshelby's solution for the inhomogeneity problem where an ellipsoid inclusion is embedded into an infinite matrix. In comparison to SEMM, CBMM can provide more rigorous relationships of the stress/strain fields between macroscale and microscale; thus, calibration parameters are typically not required in these models. Therefore, in the attempt to find out a methodology that can accurately predict the mechanical properties of PA mixes without the need for calibrations, CBMM were studied.

A comprehensive investigation into the performance of commonly used CBMM in predicting the stiffness of PA materials was conducted. It was found that CBMM performed better in predicting the modulus of a composite with a low concentration of inclusions (i.e. mastic) than their performances for a highly concentrated composite (i.e. mixes). This can be associated with the fact that CBMM were primarily developed to account for the stiffening effect caused by the embedded inclusions in a mix with minimal particle interactions.

The results showed that the performance of CBMM at higher frequencies is much better than that at lower frequencies. At higher frequencies, the predicted dynamic modulus and phase angle followed the same shapes as those measured from laboratory tests. Different CBMM provided different predictions of the stiffness's magnitudes. The predictions using the GSC model when the aggregate phase was added before the addition of the air voids phase were in the best agreement with the experimental values. On the other hand, at lower frequencies, none of the evaluated micromechanical models could adequately predict the mechanical properties of PA mixes. The shapes of the predicted dynamic modulus and phase angle were not consistent with experimental results, and moreover, in general, all the models significantly underestimated the values of dynamic modulus and overestimate the values of phase angle.

In order to find out possible approaches to improve the accuracy of the predictions. Further attention was given to the sensitivities of the predictions' accuracy to (1) the scale of the matrix phase, (2) the utilization of the differential scheme, and (3) the value of the matrix's Poisson's ratio. The results showed that (1) upscaling from a higher scale matrix phase (i.e. mortar) provided more accurate predictions than upscaling from a lower scale matrix phase (i.e. asphalt binder and mastic); (2) After the introduction of the differential scheme, the accuracy of the predictions improved at higher frequencies, whereas at lower frequencies, it did not; (3) the accuracy of the predictions did not show a considerable increase by adjusting the Poisson's ratio of the matrix phase.

Overall, CBMM failed to accurately predict the mechanical properties of a composite with a high concentration of inclusions, especially at lower frequencies (high temperatures). A discussion about the reasons behind the failure of CBMM was further given. It was pointed out that CBMM have the limitations that (1) these models cannot explicitly account for the inter-particle interactions (the volume-filling stiffening effect), and (2) they cannot capture the stiffening effect due to the particle-to-particle direct contacts.

The limitations of CBMM are related to the fact that in such models, the set of all the individual particles is simply represented as one inclusion phase. In this case, it is impossible to consider any characteristics of individual particles, not to mention their interactions and direct contacts. Therefore, in order to improve the accuracy of the predictions, efforts were further made to study DBMM which are capable of taking into account the characteristics of individual particles.

7.1.1.3 *Implementation and evaluation of DBMM*

In Dvorkin's model (one of DBMM), a PA mix is described as an assembly of packing individual particles that are bonded by mortar materials. This model includes several geometric parameters to describe the characteristics of individual particles, i.e. the radius of the particles, the average number of contacts per particle, and the distance between adjacent particles. Studying Dvorkin's model aimed to investigate if the accuracy of the predictions at lower frequencies can be improved with the consideration of these particles' characteristics.

A framework was proposed in order to achieve the implementation of Dvorkin's model for predicting the stiffness of PA mixes. This framework included the following procedures:

(1) a microstructure model where a PA mix was simulated as an assembly of identical spherical particles covered and bound together by mortar materials was developed.

(2) the geometric parameters in the microstructure model were determined from the volumetric properties of the mix. The radius of the spherical particles was determined from the aggregate gradation; the thickness of the coating mortar was determined from the mortar content; the minimum distance between two adjacent particles and the coordination number were determined from air voids content; and the radius of the binding mortar was finally determined on the basis of the values of other parameters.

(3) the stiffness of PA mixes was calculated in three steps. At first, the stiffness of the skeleton framework consisting of aggregate particles and the binding mortar was predicted using Dvorkin's model. Then the matrix's stiffness of an equivalent two-phase composite, whose stiffness was identical to that of the skeleton framework, was back-calculated using CBMM. At last, by adding the coating mortar to the matrix, the stiffness of PA mixes was calculated using CBMM again.

The evaluation results showed that Dvorkin's model provided accurate predictions at high frequencies. However, this model showed similar limitations as CBMM: at low frequencies the predicted dynamic moduli were significantly lower than the experimental results, and moreover, the predicted phase angle did not show a decreasing trend. Further investigation into the sensitivity of the predictions' accuracy to the geometric parameters and the Poisson's ratio of the mortar showed that the performance of Dvorkin's model cannot be significantly improved by varying the values of these parameters.

Overall, it can be concluded that in comparison to SEMM and CBMM, Dvorkin's model has the advantage of considering the characteristics of individual particles, and thus, Dvorkin's model can account for the volume-filling stiffening effect in a more explicit way. Nevertheless, Dvorkin's model has a similar limitation as CBMM that it cannot capture the stiffening effect due to the particle-to-particle direct contacts for studied PA mixes.

Based on all the above findings, it can be finally concluded that accurately predicting the stiffness of a PA mix, the first step towards analysing the ravelling distress, cannot be achieved by using the commonly used micromechanical models without any calibrations. Therefore, to achieve the objective of this thesis, a new micromechanical model was further developed.

7.1.2 Development of a hybrid micromechanical model

The first part of this thesis showed that commonly used micromechanical models are not capable of accurately predicting the stiffness of PA mixes at lower frequencies mainly because these models cannot capture the stiffening effect of the particle-to-particle direct contacts. Therefore, before the development of a new micromechanical

model, a methodology was first developed to quantify the contribution of the particle-to-particle direct contacts to the total stiffness of a PA mix.

An explanation about the structuralization of the aggregate particles in a PA mix was at first proposed. It was pointed out that the sucking action of the mortar bridges between the aggregate particles prevents an unconfined PA mix from collapsing into a pile of rocks, which encourages particle-to-particle interactions and, as such, enhances the stiffness of the system of aggregate particles.

Based on the understanding of the particles' structuralization, Walton's model was used to estimate the stiffening effect of the particle-to-particle direct contacts. The confinement for the formation of the particles' direct contacts was considered as the stresses in the mortar phase. These stresses were calculated using Dvorkin's model where the stiffening effect on the mortar's stresses due to the presence of the surrounding particles was considered.

A hybrid micromechanical model which combined the volume-filling stiffening effect and the stiffening effect of the particle-to-particle direct contacts was further developed. It was assumed that the volume-filling stiffening effect and the stiffening effect of the particle-to-particle direct contacts are in a parallel arrangement. Therefore, the total stiffness of the mix was computed by summing up the stiffnesses coming from these two mechanisms. In the end, the capability of the model in accurately predicting the stiffness (both dynamic modulus and phase angle) of PA mixes was verified.

In summary, this study successfully developed a micromechanics-based model which is able to predict the stiffness of a PA mix based on the stiffnesses on the microscale. This thesis helps deepen our understanding of the behaviour of PA mixes and the characteristics of different types of micromechanical models. More importantly, as the first step of the proposed homogenization-based approach, this study enables us to further the implementation of the proposed approach in analysing the propensity of a given PA mix for ravelling.

7.2 Recommendations for future research

On the basis of the obtained results in this thesis, recommendations are made for future research in order to further explore the utilization of micromechanical models in the field of pavement engineering.

In the current study, two types of PA mixes used for verification were prepared with the same asphalt binder contents and the same aggregate gradations. In future research, more laboratory tests performed on PA mixes with different gradations and different asphalt binder contents can be used to further verify the proposed model.

In this research, the developed hybrid micromechanical model was implemented to estimate the stiffness of PA mixes. The utilization of this model can be further extended to DA mixes.

This thesis focused on the development of a micromechanical model for accurately predicting the stiffness of PA mixes. However, as mentioned at the beginning, the final objective of this research is to analyse the ravelling distress of PA pavements, and the prediction of a mix's stiffness is only the first step for this purpose. Therefore, in future research, the developed model will be used to conduct other steps, i.e. estimating the stress and strain fields of individual phases, and to finally achieve the analysis of the ravelling distress of PA mixes.

Appendix A

Numerical solutions to mortar's displacements in Dvorkin's model

In this study, a numerical method was used to calculate the displacements of the mortar, $V(x)$ (see Equation (5.9)) and $U(x)$ (see Equation (5.10)). In the following paragraphs, the steps for solving $V(x)$ in Equation (5.9) are presented, and the same method can be used to solve $U(x)$ in Equation (5.10). It is noted that the method used in this study was developed on the basis of the basic approaches for solving the Volterra integral equations of the second kind (Golberg, 1990).

The calculation of $V(x)$ can be made in three steps:

- *Step1: choose the points where the value of V(x) is calculated.* In the range from 0 to a, $N+1$ discrete points of x with an identical distance between neighbouring points, x_0, x_1,...,x_N, are chosen. By substituting these points into Equation (5.9), $N+1$ equations are obtained, see Equation (A.1). The following steps aim to solve these $N+1$ equations to obtain the values of $V(x)$ at different points of x.

$$\delta_n + V(x_i) = \Lambda_n \int_0^\pi d\varphi \int_0^{x_i \cos\varphi + \sqrt{a^2 - x_i^2 \sin^2\varphi}} \frac{V(\sqrt{x_i^2 + s^2 - 2x_i s \cos\varphi})}{h_0 + \frac{x_i^2 + s^2 - 2x_i s \cos\varphi}{2R}} ds, \; i = 0, \, 1, \, ..., \, N \quad \text{(A.1)}$$

- *Step 2: discretize the variables.* The variable φ is identically discretized into $N+1$ discrete points in the range from 0 to π, φ_0, φ_1,..., φ_N. The discretization of s is dependent on the value of x_i. In order to solve the $N+1$ unknowns of $V(x_i)$ in Equation (A.1), it is required that no other unknowns are introduced. This means that for a certain value of x_i, the discretized values of s, s_0, s_1,..., s_{ni}, should satisfy Equation (A.2). Thus, the values of s_j can be calculated by using Equation (A.3). Equation (A.3) is a quadratic equation, and the roots are given as Equation (A.4). It is noted here that since the upper boundary of s is a function of x_i, the number of the discretized points of s (represented by n_i in Equations (A.3)-(A.4)) is dependent on the value of x_i.

$$V(\sqrt{x_i^2 + s_j^2 - 2x_i s_j \cos\varphi_k}) = V(x_j), \; i = 0, \, 1, \, ..., \, N \quad \text{(A.2)}$$

$$x_i^2 + s_j^2 - 2x_i s_j \cos\varphi_k = x_j^2, \; j = 0, \, 1, \, ..., \, n_i \quad \text{(A.3)}$$

$$s_j = x_i \cos\varphi_k \pm \sqrt{x_j^2 - x_i^2 \sin^2\varphi_k}, \; j = 0, \, 1, \, ..., \, n_i \quad \text{(A.4)}$$

- *Step 3: solve the integral equation.* By substituting all the discretized points of φ and s into Equation (A.1), the discretized form is written as Equation (A.5). The values of $V(x_i)$ can be obtained by solving these $N+1$ equations. In Equation

(A.5), $\omega_k{}^\varphi$ and $w_j{}^s$ are the weights of the discrete points of φ_k and s_j, respectively. If the trapezoidal rule is used for approximating the integral values, the values of $\omega_k{}^\varphi$ and $w_j{}^s$ are equal to 1 for the middle points while they are equal to 0.5 for the points at the boundaries. h^φ is the distance between two neighbouring points for φ, which is equal to π/N. $h_{ij}{}^s$ is the distance between two neighbouring points for s, which can be automatically known once the values of s_j are obtained.

$$\delta_n + V(x_i) = \Lambda_n \sum_{k=0}^{N} h^\varphi \omega_k^\varphi \sum_{j=0}^{n_i} h_{ij}^s \omega_j^s \frac{V(x_j)}{h_0 + \dfrac{x_j^2}{2R}}, \; i = 0, \, 1, \, ..., \, N \tag{A.5}$$

Reference

GOLBERG, M. A. 1990. *Numerical Solution of Integral Equations*.

Summary

With the attempt to reduce traffic noise, porous asphalt (PA) mixture is widely used as a wearing course on the highways in the Netherlands. However, due to the open structure, PA mix pavement easily suffers from the loss of individual aggregates from its surface, which is named as ravelling. After the initial ravelling, the damage can rapidly develop into potholes which can significantly reduce the driving safety of the pavement.

In order to develop an accessible tool to assist pavement practitioners in mitigating ravelling distress or making accurate ravelling distress predictions, this thesis proposed one possible solution based on the homogenization technique. At first, the properties of individual components are measured in the laboratory and the stiffness of a PA mix is predicted using micromechanical models. Then, the strains in the PA mix layer are calculated by means of any available pavement analysis tool (i.e. 3D-MOVE) on the basis of the predicted mix's stiffness. Lastly, the local stresses/strains in the individual phases are calculated. Based on the fatigue characteristics of each phase under these stresses/strains conditions, the propensity of a given PA mix for ravelling can be evaluated.

Following the proposed solution, this thesis focused on the first step of accurately predicting the stiffness of a PA mix using micromechanical models. Two types of PA mixes, with different air voids contents, were used for the evaluation of different models. Both the dynamic modulus and the phase angle of the mixes were measured under the uniaxial loading condition at different frequencies and temperatures. Based on these experimental data, three types of commonly used micromechanical models, including the Semi-empirical micromechanical models (SEMM), Continuum based micromechanical models (CBMM), and Discrete particles-based micromechanical models (DBMM), were assessed on their ability of accurately predicting the stiffness of a PA mix.

The results showed that when an aggregate organization factor was used, SEMM provided accurate predictions. However, the values of this factor needed to be calibrated from laboratory tests. On the other hand, CBMM and DBMM do not include any calibration factor, and they can provide accurate predictions at high frequencies/low temperatures. However, the predictions at low frequencies/high temperatures did not match with the experimental results, and generally, the predictions were much lower. Therefore, it can be concluded that without any calibration, commonly used micromechanical models are incapable of accurately predicting the stiffness of a PA mix in a wide frequency/temperature range.

The assessment of different types of micromechanical models also revealed that the limitation of these models is related to the fact that they can only account for the

volume-filling stiffening effect due to the addition of aggregates into mortar, but they do not take into account the stiffening effect due to the particle-to-particle direct contacts. Based on this realization, a new micromechanical model was further developed in this thesis. The structuralization of the aggregate particles in a PA mix was explained based on the concept of the sucking action of the mortar bridges between the aggregate particles. Furthermore, Walton's model was used to estimate the stiffening effect of the particle-to-particle direct contacts. A hybrid micromechanical model which combined the volume-filling stiffening effect and the stiffening effect of the particle-to-particle direct contacts was further developed. In the end, the capability of the developed model in accurately predicting the stiffness (both dynamic modulus and phase angle) of PA mixes was verified.

In summary, this study successfully developed a micromechanics-based model which is able to predict the stiffness of a PA mix based on the stiffnesses on the microscale. This thesis helps deepen our understanding of the behaviour of PA mixes and the characteristics of different types of micromechanical models. More importantly, as the first step of the proposed homogenization-based approach, this study enables us to further the development of an accessible tool to assist pavement practitioners in ravelling analysis.

Curriculum vitae

Hong Zhang 张红

27 July 1990	Born in Laiwu, Shandong Province, China
Aug. 2008 – Jul. 2012	B.S. in Road and Bridge Engineering
	Honours School
	Harbin Institute of Technology, China
Aug. 2012 – Jul. 2014	M.S. in Highway and Railway Engineering
	School of Transportation Science and Engineering
	Harbin Institute of Technology, China
Jul. 2014 – Jul. 2015	Road Designer
	Shanghai Urban Construction and Municipal Engineering Co., Ltd., China
Sep. 2015 – Jun. 2022	Ph.D. candidate
	Section of Pavement Engineering
	Faculty of Civil Engineering and Geosciences
	Delft University of Technology, The Netherlands
Oct. 2019 – Dec. 2019	Visiting Ph.D. student
Feb. 2020 – May 2020	Department of Civil Infrastructure and Environmental Engineering
	Khalifa University, UAE

List of publications

Journal Publications

- **H. Zhang**, K. Anupam, T. Skarpas, C. Kasbergen, S. Erkens. Contact Mechanics-based Solution to Predict Modulus of Asphalt Materials with High Porosities. Materials & Design, 2021.

- **H. Zhang**, K. Anupam, T. Skarpas, C. Kasbergen, S. Erkens. Understanding the Stiffness of Porous Asphalt Mixture through Micromechanics. Transportation Research Record, 2021.

- **H. Zhang**, K. Anupam, T. Scarpas, C. Kasbergen, S. Erkens. Simple Homogenization-based Approach to Predict Ravelling in Porous Asphalt. Transportation Research Record. 2020.

- **H. Zhang**, K. Anupam, T. Scarpas, C. Kasbergen, S. Erkens, L. Al Khateeb. Continuum-based Micromechanical Models for Asphalt Materials: Current Practices & Beyond. Construction and Building Materials, 2020.

- **H. Zhang**, K. Anupam, T. Scarpas, C. Kasbergen, S. Erkens. Effect of Stone-on-Stone Contact on Porous Asphalt Mixes: Micromechanical Analysis. International Journal of Pavement Engineering. 2019.

- **H. Zhang**, K. Anupam, T. Scarpas, C. Kasbergen. Comparison of Different Micromechanical Models for Predicting the Effective Properties of Open Graded Mixes, Transportation Research Record, 2018.

- **H. Zhang**, K. Anupam, T. Scarpas, C. Kasbergen. Issues in the Prediction of the Mechanical Properties of Open Graded Mixes, Transportation Research Record, 2018.

Conference papers

- **H. Zhang**, K. Anupam, T. Scarpas, C. Kasbergen, S. Erkens, H. Wang & P. Apostolidis. Micromechanical Modelling of Porous Asphalt Mixes at High Temperatures. Advances in Materials and Pavement Performance Prediction (AM3P), 2020.

- **H. Zhang**, K. Anupam, T. Scarpas, C. Kasbergen, H. Wang, S. Erkens. Influence of Loading Characteristics on Micromechanical Models. Transportation Research Board (TRB), 2019.

- **H. Zhang**, K. Anupam, T. Scarpas, C. Kasbergen, S. Erkens. Implementation of Dvorkin's Model on Predicting Effective Modulus of Open Graded Mixes. Transportation Research Board (TRB), 2019.